

Extending the ALMA Census of Circumstellar Disks in the Upper Scorpius OB Association

JOHN M. CARPENTER,¹ TARAN L. ESPLIN,² KEVIN L. LUHMAN,^{3,4} ERIC E. MAMAJEK,^{5,6} AND SEAN M. ANDREWS⁷

¹*Joint ALMA Observatory, Avenida Alonso de Córdova 3107, Vitacura, Santiago, Chile*

²*Steward Observatory, University of Arizona, 933 North Cherry Avenue, Tucson, AZ 85721, USA**

³*Department of Astronomy and Astrophysics, The Pennsylvania State University, University Park, PA 16802, USA*

⁴*Center for Exoplanets and Habitable Worlds, The Pennsylvania State University, University Park, PA 16802, USA*

⁵*Jet Propulsion Laboratory, California Institute of Technology, 4800 Oak Grove Drive, Pasadena, CA 91109, USA*

⁶*Department of Physics and Astronomy, University of Rochester, P.O. Box 270171, 500 Wilson Boulevard, Rochester, NY 14627-0171, USA*

⁷*Center for Astrophysics | Harvard & Smithsonian, 60 Garden Street, Cambridge, MA 02138, USA*

ABSTRACT

We present ALMA Band 7 continuum (340 GHz) and CO J=3–2 observations for an extended sample of disks in the Upper Scorpius OB Association (Upper Sco, age ~ 10 Myr). The targets were selected from previous studies that identified new members of Upper Sco using photometry and astrometry from the *Gaia* mission, and the presence of a disk has been inferred from mid-infrared excess emission. The new ALMA observations are combined with previous ALMA data to define a sample of 202 Upper Sco members with disks that have spectral types between G0 and M5.5. Among these sources, 120 (59%) have been detected in the continuum with a signal-to-noise ratio ≥ 3 , and 83 (41%) have been detected in CO J=3–2. Both the continuum and CO J=3–2 fluxes show a strong correlation with the spectral type of the central star and the type of disk inferred from the shape of the infrared spectral energy distribution, where disks around earlier type stars and full disks are more luminous than disks around later type stars and evolved and debris disks. The median dust continuum luminosity is lower for disks in Upper Sco than in younger regions, as found in previous studies, where the differences are more pronounced in later spectral types (M4–M5) than in earlier spectral types.

1. INTRODUCTION

Demographic studies are a widely used method to investigate the evolution of protoplanetary disks. By observing the properties of disks surrounding stars of various ages and masses, any age-related variations are assumed to indicate secular evolution. In theory, changes in disk size and mass over time can help constrain the mechanisms driving disk dispersal (see review by Manara et al. 2023).

Numerous demographic studies have been performed over a range of wavelengths to trace various aspects of disk evolution. Near-infrared (1–4 μm) photometric surveys, which probe warm dust in close proximity to the star, have shown $\gtrsim 80\%$ of solar-mass stars contain an inner disk at an age of ~ 1 Myr, and that by an age of ~ 5 Myr, only $\sim 20\%$ of the inner disks remain (Haisch et al. 2001; Hernández et al. 2005; Mamajek 2009). The *Spitzer Space Telescope* and the all-sky *Wide-field Infrared Survey Explorer (WISE)* have extended these studies to mid-infrared wavelengths (3.5–24 μm), which are particularly sensitive to the presence of dust emission at a few to several astronomical units around solar-type stars. Ribas et al. (2015, see also Ribas et al. 2014) compiled observations from numerous studies with *Spitzer* and *WISE*. Averaged across all stellar masses, they found an exponential dissipation timescale of ~ 3 Myr at 3.4–12 μm and ~ 5 Myr at 22–24 μm , with shorter dissipation timescales for stars more massive than $2 M_{\odot}$. The longer dissipation timescales at long wavelengths are consistent with inside-out clearing of disks (see, however, Maeshima et al. 2021).

Corresponding author: John M. Carpenter
 john.carpenter@alma.cl

* Strittmatter Fellow

Measurements of the gas dissipation times are more limited but suggest similar timescales. The average mass accretion rate decreases with stellar age (Muzerolle et al. 2000; Sicilia-Aguilar et al. 2010; Hartmann et al. 2016), although individual disks with high accretion rates can persist to ages of \sim 10 Myr (Ingleby et al. 2014; Manara et al. 2020). Fedele et al. (2010) showed that the fraction of K0–M5 stars with measurable gas accretion rates has an exponential dissipation timescale of \sim 2.3 Myr, which is comparable if not slightly shorter than the dust dissipation time. Briceño et al. (2019) inferred a similar timescale of 2.1 ± 0.5 Myr based on the accretion fraction of K and M-type stars for various stellar population in Orion.

Millimeter and submillimeter wavelength continuum and spectral line observations provide complementary information on the disk demographics. The longer wavelength observations have lower optical depths than infrared data, providing a better measure of the dust content of millimeter-sized grains. In addition, the higher angular resolution from interferometric observations provide better constraints on the spatial extent of disks. In principle, such studies can discern the dominant mechanisms that control the evolution of disks (e.g., see Rosotti et al. 2019; Zagaria et al. 2022; Manara et al. 2023).

ALMA has greatly expanded the scope of millimeter and submillimeter studies of disks due to vastly improved sensitivity and angular resolution (for a recent review, see Manara et al. 2023). Barenfeld et al. (2016, see also Carpenter et al. 2014) showed that the disks in the Upper Sco OB Association (Upper Sco, \sim 10 Myr) have lower dust masses than the younger Taurus region. This trend with age has been confirmed with observations of other regions, including Lupus (Ansdel et al. 2016), Chamaeleon I (Pascucci et al. 2016), Ophiuchus (Williams et al. 2019), σ Orionis (Ansdel et al. 2017), IC 348 (Ruiz-Rodríguez et al. 2018), the Orion Nebula Cluster (Eisner et al. 2018), the Orion A molecular cloud (Grant et al. 2021; van Terwisga et al. 2022), and the eastern portion of NGC 2024 (van Terwisga et al. 2020). λ Orionis, which has a comparable age to Upper Sco, also tends to have fainter disks than younger regions (Ansdel et al. 2020), supporting the scenario that the differences in the dust masses may be a result of evolution. However, variations in the radiation field across different regions might also influence disk luminosities. Trapman et al. (2020) estimated that the ambient radiation field in Upper Sco ranges from 10 to 300 G_0 , which is significantly stronger than that in the Taurus molecular cloud (Flagey et al. 2009) and Lupus (Cleeves et al. 2016), though weaker than the levels found in the Orion Nebula Cluster (up to $10^7 G_0$; Aru et al. 2024) and σ Orionis (up to $\sim 10^5 G_0$; Maucó et al. 2023). Trapman et al. (2020) showed that the intermediate radiation fields observed in Upper Sco can result in reduced dust masses.

A key region in demographic studies has been Upper Sco. It is one of three subgroups of the Scorpius-Centaurus OB Association (Sco-Cen), which also includes Upper Centaurus-Lupus (UCL) and Lower Centaurus-Crux (LCC). Upper Sco is the youngest of three subgroups. The age of the association is typically considered to be between 5 and 11 Myr. The ages of the K- and M-type stars in Upper Sco inferred from pre-main-sequence evolution tracks averages to \sim 5 Myr (Preibisch et al. 2002; Slesnick et al. 2008). However, Pecaut et al. (2012) inferred an age of \sim 11 Myr for the association based on the luminosities of the F-type stars, the kinematic age expansion of Upper Sco, and isochronal ages for the B-, A-, and G-type stars and the M supergiant Antares. Feiden (2016) suggests that the apparent discrepancy in the ages between the early and late-type stars is a result of magnetic inhibition of convection of late-type stars, and showed models that include magnetic fields (Feiden & Chaboyer 2012, 2013) yield older ages (9–10 Myr) for the late type stars that are more inline with early type stars. More recent studies incorporating *Gaia* astrometry suggest that there are distinct clusters within the association that have ages between 4 and 19 Myr (Kerr et al. 2021; Ratzenböck et al. 2023a,b). Regardless of the precise ages and complex star formation history, Upper Sco is generally considered older than regions such as Taurus and Ophiuchus on the basis of the relative luminosity of stars of similar spectral types (Pecaut et al. 2012; Luhman & Esplin 2020). And given the mean distance of \sim 145 pc (de Zeeuw et al. 1999; Wright & Mamajek 2018; Kerr et al. 2021; Ratzenböck et al. 2023a), Upper Sco contains the largest nearby population of disks at its age (Esplin et al. 2018; Luhman 2022a).

Carpenter et al. 2014, Barenfeld et al. (2016), and Barenfeld et al. (2017) provided an initial census of the gas and dust properties for a sample of 106 stars in Upper Sco between spectral types of G0 and M5. Since those surveys, the census of the Upper Sco membership has expanded and refined with additional ground-based photometric and spectroscopic surveys and with high-precision astrometry from the *Gaia* mission (Perryman et al. 2001; de Bruijne 2012; Gaia Collaboration et al. 2016). Given the significance of Upper Sco in demographic studies, we have expanded the submillimeter census of the disk properties in Upper Sco using ALMA. This study present the observation data and re-evaluates the demographic trends. Moreover, the enlarged sample enables us to analyze subsets of the data with spectral type.

The paper is organized as follows. Section 2 describes how the sample of stars was selected. Section 3 provides an overview of the new observations. Sections 4 and 5 present the continuum and spectral line measurements, respectively, along with an analysis of the Upper Sco demographics. The results and a comparison with other regions are discussed in Section 6.

2. SAMPLE

The sample for this survey was drawn from the census of young stars and brown dwarfs presented in Luhman et al. (2018), who identified 1631 likely members of the Upper Sco association based on parallaxes, proper motions, color-magnitude diagrams, and optical and infrared spectra. Esplin et al. (2018) identified stars with circumstellar disks by mid-infrared excess emission detected with the *WISE* and *Spitzer*. From the Esplin et al. (2018) compilation, 284 disk-bearing stars were selected that have spectral types between G0 and M5. (In a later analysis, one of the M5 stars was reclassified as M5.5.) The sources were observed with ALMA as described in Section 3.

Since the analysis by Luhman et al. (2018) and Esplin et al. (2018), the second and third data releases of *Gaia* have become available (DR2 and DR3, Gaia Collaboration et al. 2018, 2021, 2023), which provide high-precision proper motions and parallaxes down to much fainter magnitudes than the first data release ($G \sim 20$). Luhman & Esplin (2020) and Luhman (2022b) used the data from DR2 and DR3 to refine the census of Upper Sco and other populations in Sco-Cen. Because of overlap among the Sco-Cen populations in their spatial positions and kinematics, some stars have kinematics that are consistent with multiple groups.

The 284 ALMA targets are listed in Table 1, which includes each source’s designation from *Gaia* DR3, adopted spectral type (Luhman & Esplin 2020; Luhman 2022b; Manara et al. 2020), disk classification (Esplin et al. 2018; Luhman 2022a), parallactic distance from *Gaia* DR3 (Bailer-Jones et al. 2021), and the Sco-Cen populations with which the *Gaia* kinematics are consistent (Luhman 2022b). The spectral types are taken primarily from the compilation in Luhman (2022b). Manara et al. (2020) presented spectral types from X-shooter spectra for 36 stars.¹ For five stars where the spectral type in Manara et al. (2020) differed from Luhman (2022b) by more than one subclass, we adopted the classification from Manara et al. (2020). If *Gaia* data are not available or the star is not a kinematic member of a known Sco-Cen subgroup, no population is listed in Table 1. Among the 284 targets, 116 have kinematics that are consistent with Upper Sco alone, 92 are consistent with Upper Sco and one or more other Sco-Cen groups, 76 are not members of Upper Sco or lack the kinematic data from *Gaia* DR3 for membership classifications. For this study, we adopt the 208 stars from the first two categories as members of Upper Sco. As described in Section 4.1, for 13 out of the 284 sources, no continuum emission was detected around the target star but a continuum source was detected nearby that could be responsible for the observed infrared excess. These 13 sources, which include six Upper Sco members, are not considered when analyzing the continuum and CO flux distributions. The 202 sources that constitute the final Upper Sco sample are marked in Table 1.

As described in Esplin et al. (2018) and Luhman (2022a), the disks have been classified based on the shape of the spectral energy distribution and location in infrared color-color diagrams. The final Upper Sco sample includes 121 sources where the disk has been classified as “full” (where the disks are optically thick at infrared wavelengths and lack significant clearing of dust in the inner disk), 15 as “transitional” (where the disks have inner holes of radius $\gtrsim 1$ au), 28 as “evolved” (the disk is becoming optically thin but no significant clearing of the inner disk has occurred), and 38 as “debris”, “evolved transitional” or class III, where the disk is optically thin and have inner holes of radius $\gtrsim 1$ au. Figure 1 shows the distribution of the spectral types by the disk class. Most stars (72%) have spectral types of M3 or later, and among the later type stars, 64% have full disks.

3. OBSERVATIONS

ALMA observations of the continuum and Carbon Monoxide (CO) were obtained in Cycles 0, 2, and 6 using the 12-m array. The Cycles 0 and 2 data for 106 sources were presented in Barenfeld et al. (2016, see also Carpenter et al. 2014). An additional 178 sources were observed in Cycle 6 following the observational setup in the earlier cycles.

Table 2 presents the observation log for the Cycle 6 observations. An observation log for the earlier observations is available in Barenfeld et al. (2016). As with the previous surveys, all observations in Cycle 6 were obtained in Band 7 (Mahieu et al. 2012). Spectral windows were centered at 334.2, 336.1, 346.2, and 348.1 GHz with a bandwidth of 1.875 GHz for each window. The window centered at 346.2 GHz, which includes the CO J=3–2 transition at a

¹ Of the 36 stars, 35 are in our sample. Manara et al. (2020) resolved 2MASS J15354856-2958551 into a binary for the first time and the secondary is not explicitly part of the sample.

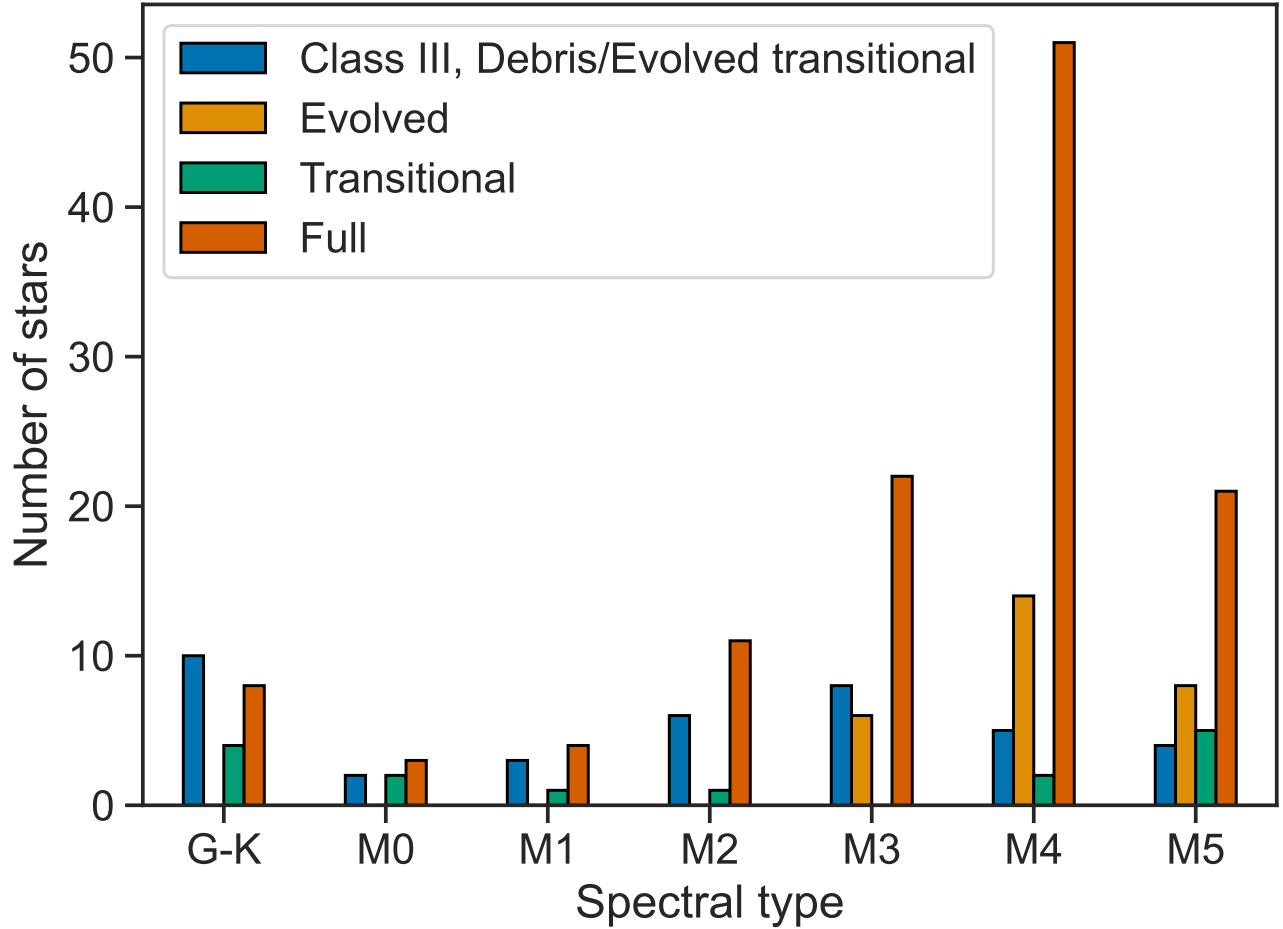


Figure 1. Distribution of spectral types for the 202 sources in the Upper Sco sample. One source (2MASS J16193570-1950426) with a uncertain spectral type has been excluded. For the M-type stars, the plotted subclass is truncated at the integer value (e.g. M2.5 is plotted as M2).

rest frequency of 345.7959899 GHz, has a channel width of 0.488 MHz (0.429 km s⁻¹ for CO J=3–2) with a spectral resolution of 0.977 MHz (0.858 km s⁻¹). The other three windows have a channel width and a spectral resolution of 0.977 MHz and 1.129 MHz, respectively.

The observations were obtained with the 12-m array using between 43 and 50 antennas. The maximum baselines ranged between 740 m to 2617 m to provide an angular resolution between 0''.1 and 0''.3. The full-width-at-half-maximum (FWHM) primary beam size of the observations is 18''.5. The typical on-source integration time was 2.5 minutes to provide a continuum sensitivity (1σ) of ~ 0.15 mJy.

The data were calibrated by ALMA staff using the ALMA data reduction pipeline. Data reduction steps include atmospheric calibration using the 183 GHz water vapor radiometers, bandpass calibration, flux calibration, and gain calibration. The calibrators for each observation date are listed in Table 2. We performed phase-only self-calibration for the bright sources using Common Astronomy Software Applications (CASA) 5.6.1 package (CASA Team et al. 2022). We assume a 1σ flux calibration uncertainty of 10%.

Continuum images were constructed in CASA by combining all channels except for channels with CO J=3–2 velocities (LSRK) between -10 and 15 km s⁻¹. A CO J=3–2 image cube was generated between velocities of -200 and 200 km s⁻¹. Images were deconvolved using the CASA task tclean. A circular clean mask was centered on the expected stellar position with a radius of $1''$ for the continuum images and $2''$ for the CO J=3–2 cubes. A larger radius was used for CO J=3–2 since the CO emission is often extended over a larger radial extent. Visual inspection of the

continuum images identified 40 additional continuum sources that are not associated with the Upper Sco target. A clean mask was also placed around these sources for both the continuum and CO J=3–2 deconvolution. All images were made with robust=2 Briggs weighting to maximize sensitivity.

Figure 2 presents the continuum and CO J=3–2 data for all 284 sources observed by ALMA. The figure for each source includes the continuum image, the integrated CO J=3–2 intensity image, the real part of the continuum visibility versus the uv distance, and the CO J=3–2 spectrum. The continuum and CO results are presented in Section 4 and Section 5, respectively.

Fig. Set 2. ALMA images of the complete sample

4. ANALYSIS OF ALMA BAND 7 CONTINUUM DATA

Figure 3 shows the Band 7 continuum images for the 120 Upper Sco sources that have been detected with a signal-to-noise ratio of ≥ 3 (see Section 4.1). For completeness, Figure 4 presents similar images for the 39 non-members of Upper Sco that were detected with ALMA. Most of the sources are point-like or slightly resolved at the resolution of these observations. Notable exceptions include the dust ring resolved in 2MASS J16042165-2130284 (Mathews et al. 2012; Zhang et al. 2014) and 2MASS J16120668-3010270 (Sierra et al. 2024). The remainder of this section analyzes the continuum measurements of the Upper Sco sources, including the procedure to measure the fluxes (Section 4.1) and analysis of the continuum measurements (Section 4.2).

4.1. Flux measurements

Fluxes were measured by either fitting the visibility data with a parametric model or performing aperture photometry in the images. First, a preliminary list of sources was generated by visually inspecting the images. If a source contained obvious asymmetries, the flux density was measured in the images using aperture photometry measured with the `imstat` function in CASA. The aperture radius was chosen by visual inspection of the images and analyzing the curve-of-growth using different aperture sizes. The uncertainties in the aperture fluxes were computed from the RMS in the image and the number of independent beams in the aperture. For sources with no obvious substructure, a two dimensional gaussian was fitted to the visibility data. The free parameters in the model are total flux density, the right ascension and declination positional offset from the phase center of the image, the FWHM of the major axis, the ratio of the minor to major axis (which reflects the inclination of the disk), and the position angle. In a few cases, the FWHM of the fitted gaussian to faint sources converged to an unrealistic large value based on inspection of the images. For these sources, a delta function was fitted with three free parameters: the source flux density and the positional offset. If there was no obvious detection in the images at the stellar position, a point-source model was fitted to the data fixed at the expected stellar position. If a continuum source was detected but it was not coincident with the stellar position, we fitted simultaneously to the visibility data a Gaussian to the continuum source and a delta function at the stellar position, where the latter was used to establish an upper limit to the continuum flux of the Upper Sco source.

The visibility fitting was performed using the affine-invariant Markov chain Monte Carlo (MCMC) ensemble sampler implemented in the Python package Emcee v3.0.2 (Foreman-Mackey et al. 2013). The fits used 50 walkers and the fits were run until the change in the autocorrelation length of the chains varied by less than 1%. Once convergence was reached, an additional 50,000 steps were run and the distribution of chains for the final 50,000 steps was used to estimate the parameters. Corner plots for the gaussian fits are presented in Appendix A.

The stars with disks were identified by infrared photometric surveys with an angular resolution of $\sim 2\text{--}12''$. Instead of originating from a disk surrounding the target star, the apparent infrared excess could potentially originate from a disk that surrounds a binary companion or from a background source, especially a galaxy. The sub-arcsecond emission with ALMA can be used to determine whether the ALMA detections coincide with the stellar position. Appendix B compares the observed ALMA positions with the expected stellar positions. Thirteen sources were identified as being contaminated by a nearby source that could potentially be responsible for the observed excess infrared radiation. Although these sources are listed in the flux tables for completeness, they are not used in analyzing the properties of Upper Sco.

Table 3 lists the measured fluxes for the 284 stars in the full sample. The table includes the source name, the Band 7 continuum flux measurement, the positional offset from the expected stellar position, and if applicable, the FWHM of the major axis, the inclination angle, and the positional angle of the Gaussian. Table 4 lists the Band 7 continuum fluxes for additional sources detected in the field that are offset from the stellar position.

4.2. Demographics

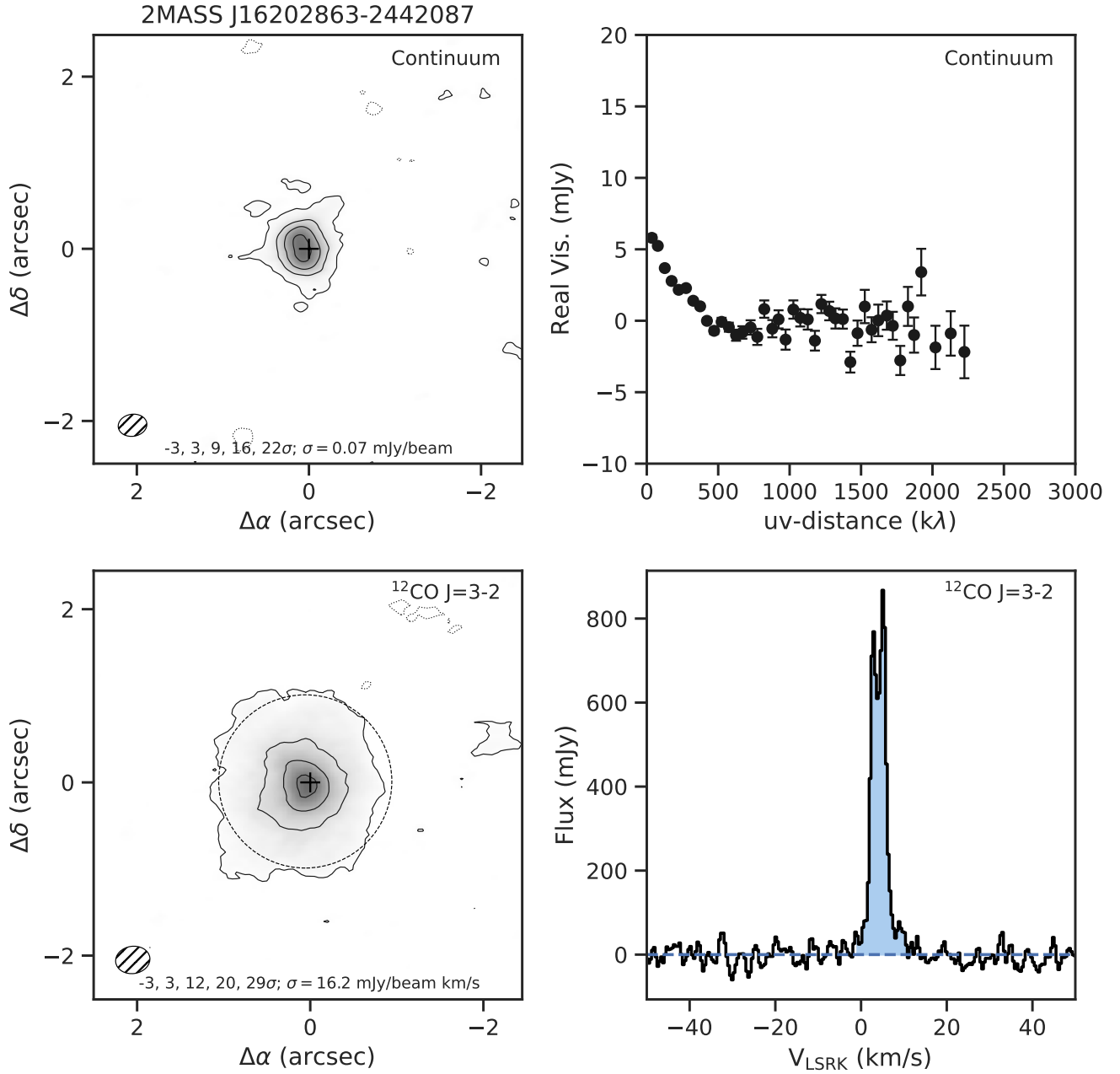


Figure 2. ALMA images of 2MASS J16202863-2442087. Upper left: 870 μm continuum image. Lower left: Integrated CO $J=3-2$ intensity. Upper right: Real part of the visibility versus baseline length, which has been phase shifted to the centroid of continuum emission (if detected) or the stellar position for continuum non-detections. Lower right: Integrated CO $J=3-2$ intensity within the circular aperture shown in the lower left panel. If the CO $J=3-2$ integrated intensity is detected with a SNR ≥ 3 , the velocity extent used to compute the integrated intensity is shaded in blue if two or more channels have a SNR $\geq 3\sigma$, and shaded in yellow otherwise. In the panels on the left, the plus symbol indicates the expected stellar position, the hatched ellipse is the full-width-at-half-maximum of the clean beam, and the dashed circle shows the aperture used to compute the CO $J=3-2$ spectrum or the continuum flux if aperture photometry was used. Diamond symbols indicate the location of any additional continuum sources detected in the image. While no primary beam correction has been applied to the images, a primary beam correction has been applied to the spectra. The complete figure set (284 images) is available in the online journal.

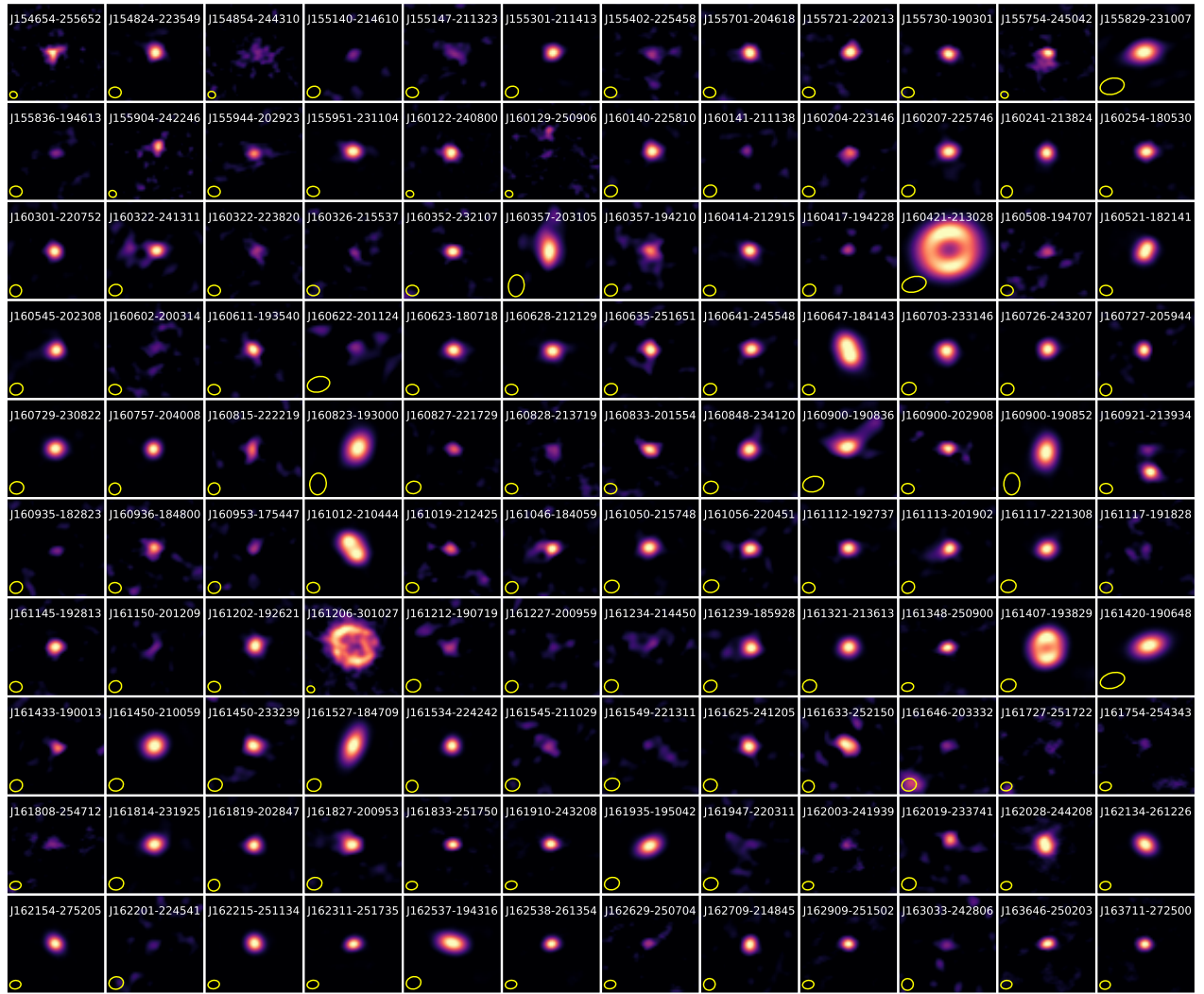


Figure 3. Band 7 continuum images for 120 sources that are confirmed Upper Sco members and have been detected in the continuum with a signal to noise ratio ≥ 3 . The angular size of each image is $3'' \times 3''$ centered on the expected stellar position. The FWHM synthesized beam is shown in the lower left corner of each panel. The sources are ordered in increasing right ascension from left to right, starting in the upper left corner.

The enlarged sample of Upper Sco members allow us to re-examine the flux distributions with demographics, especially with spectral type of the host star and the disk type inferred from infrared observations.

4.2.1. Spectral type

Figure 5 shows the Kaplan-Meier estimator (as implemented in `Lifelines`; [Davidson-Pilon et al. 2019](#)) of the Band 7 continuum fluxes for the Upper Sco sample. As demonstrated in Section 4.2.2, the submillimeter fluxes correlate with the disk type. Therefore, we select only “full” disks since it provides the largest subsample. The results show a clear dependence of the submillimeter continuum flux distributions on spectral type. Full disks that surround stars with spectral types K0–M1.75 are clearly brighter than M2–M3.75 stars, which in turn are brighter than the disks around M4–M5 stars. The log-rank two-sample linear rank test as implemented in the R ([R Core Team 2017](#)) package `EnvStats` ([Millard 2013](#)) confirms these results. The probability that the disks around K0–M1.75 stars have the same luminosity distribution as M2–M3.75 and M4–M5 stars is 3×10^{-4} and 3×10^{-13} respectively. When comparing

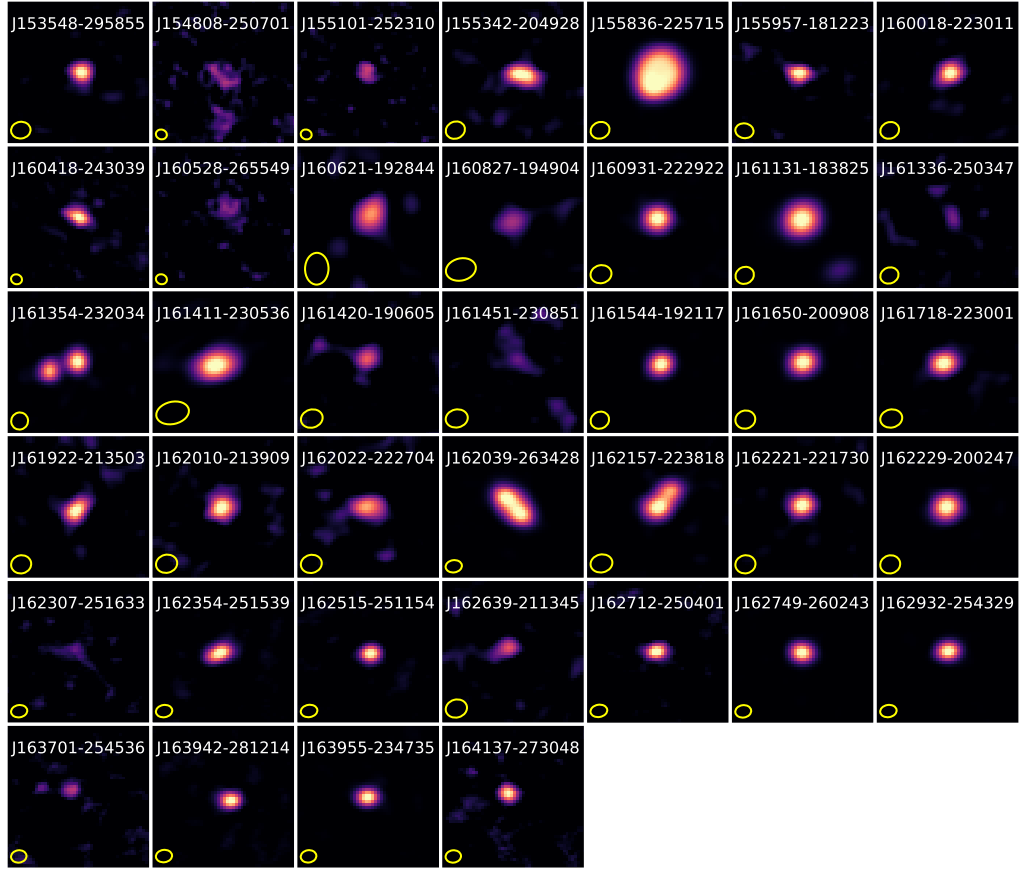


Figure 4. Same as Figure 3, except for the 39 sources in the sample that are not Upper Sco members and have been detected in the continuum with a signal to noise ratio ≥ 3 .

M2–M3.75 and M4–M5 stars, the probability that the two distributions are drawn from the same parent population is 0.02.

4.2.2. Disk type

Esplin et al. (2018) classified the disks in Upper Sco based on the infrared colors from 2MASS and *WISE*, and in a few cases, the disk classification was updated by Luhman & Esplin (2020) and Luhman (2022a). We investigate in this section the dependence of the submillimeter luminosities on the disk type inferred from the mid-infrared colors.

The detection rate has a clear dependence on disk type. The full and transitional disks have relatively high detection rates of 80% (97/121) and 93% (14/15) respectively. In contrast, evolved disks have a detection rate of 32% (9/28), and none of the 38 debris-type disks (i.e., debris/evolved transitional or Class III) have been detected.

These results do not depend on whether the star is an unambiguous kinematic member of Upper Sco or is a possible member (see Section 2 and Table 1). The Band 7 continuum detection rate for full disks for unambiguous Upper Sco members versus possible members is 79% and 81% respectively. Similarly, transitional (100% vs. 86%), evolved (31% vs. 33%), and debris-type disks (0% vs. 0%) all have similar detection rates. This suggests that most of the possible Upper Sco members are true members of the association or that the detection rates do not evolve significantly between Upper Sco and the Lower Centaurus Crux and Upper Centaurus Lupus associations.

Figure 6 shows the Kaplan-Meier distributions of the submillimeter continuum fluxes by disk types for various spectral-type ranges. The left plot shows the spectral type ranges between K0 and M1.75. Evolved and debris-type disks are not shown since none were detected by ALMA in this spectral type range. While transitional disks are

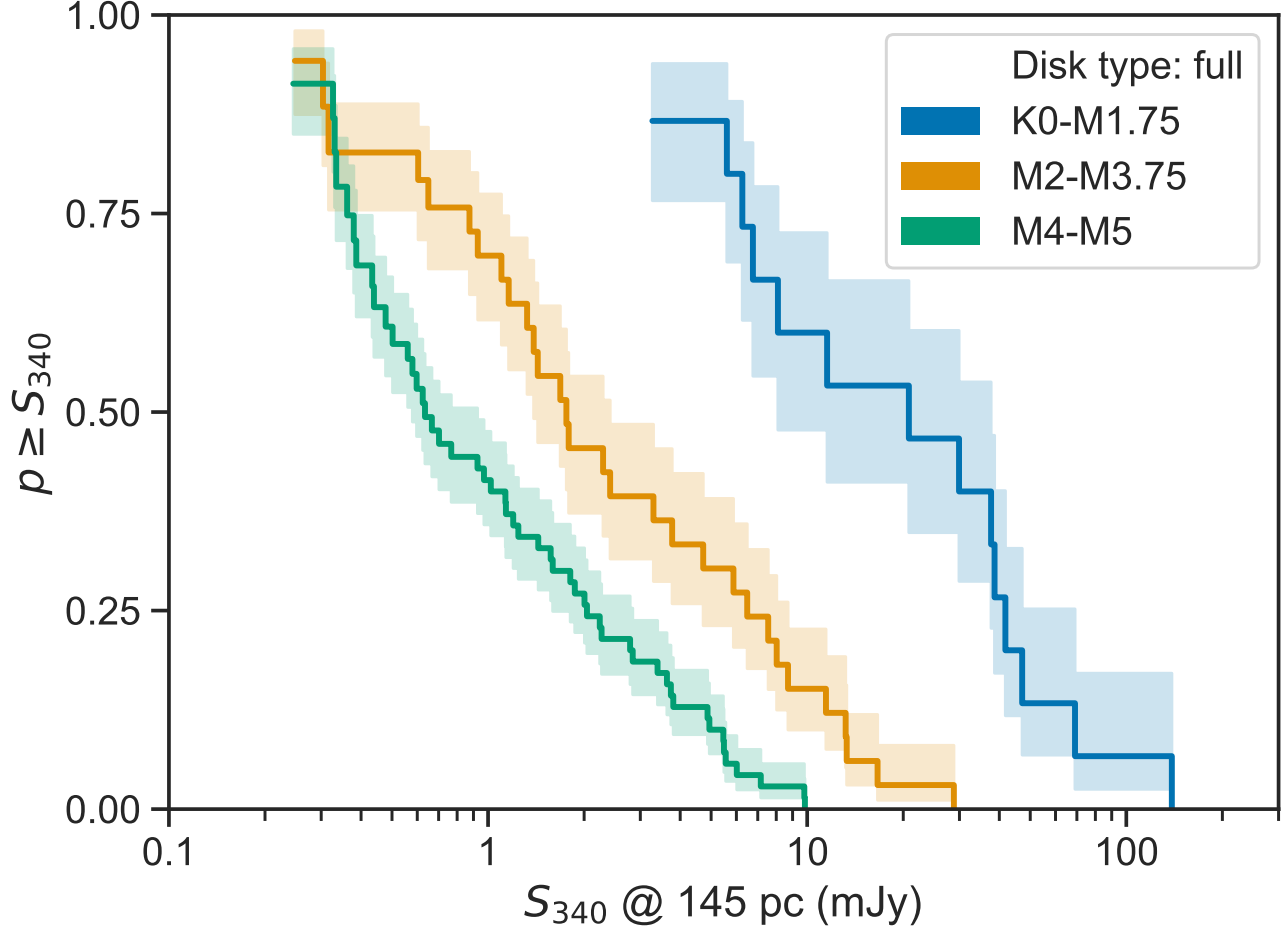


Figure 5. The Kaplan-Meier estimator of the Band 7 continuum fluxes for the full disks in Upper Sco, grouped in three spectral type ranges. Fluxes are for the observed frequency of 340 GHz at a distance of 145 pc. The results show that disks around earlier spectral types have more luminous disks than stars with later spectral types.

more luminous than full disks amongst K0–M1.75 stars, the probability that the two distributions are drawn from the same parent population is $p = 0.13$ and therefore the differences are not significant. Even though the evolved and debris-type systems were not detected, we infer from the upper limits that these disks are significantly less luminous than the full and transitional disks with $p = 2 \times 10^{-5}$ and 0.007, respectively.

The right panel in Figure 6 compares the submillimeter continuum luminosity distributions for stars with spectral types between M4 and M5. In this spectral type range, full disks are comparable in brightness to transitional disks ($p = 0.56$). Evolved disks and debris-type disks are significantly fainter than full disks with $p = 5 \times 10^{-4}$ and 4×10^{-4} , respectively. Results are not shown for spectral types between M2 and M3.75 since there is only one transitional disk and 5 evolved disks, and none were detected.

In summary, we find that full and transitional disks have no discernible differences in the submillimeter continuum flux distributions for spectral types between K0 and M5. However, full disks are more luminous in the Band 7 continuum than both evolved disks and debris-type systems.

5. ANALYSIS OF ALMA CO J=3–2 DATA

Images of the integrated CO J=3–2 intensity and the CO spectra are presented in Figure 2 for all sources. In this section, we describe the procedure to measure CO fluxes (Section 5.1) and analyze the results with disk demographics (Section 5.2).

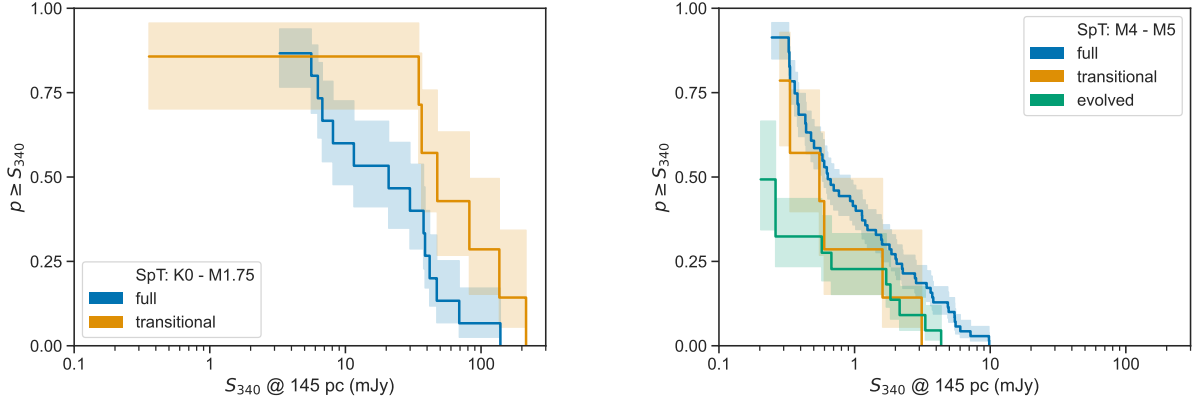


Figure 6. The Kaplan-Meier estimator of the Band 7 continuum fluxes for disks in Upper Sco classified for various disk types. The left panel shows the results for stars with spectral type between K0 and M1.75, and the right panel for stars between M4 and M5. No evolved disks are shown in the left panel since none of these systems in this spectral type range were detected with ALMA. All fluxes are for the observed frequency of 340 GHz at a distance of 145 pc.

5.1. Flux measurements

The spectral setup encompassed the CO J=3–2 spectral line as a tracer of the gas content of the disks. Measuring robust limits on the CO emission is more challenging than measuring the dust continuum since the stellar velocity is not typically known to high accuracy and the line width can range from a couple to tens of km s^{-1} depending on the inclination angle of the disk with respect to the line of sight, the radial extent of the CO emission, and the mass of the star.

The CO fluxes were measured using aperture photometry, but allowing the aperture radius and velocity range to be tuned to each source. The CO images were deconvolved using clean with a threshold limit of 2σ , where σ is the noise level in the spectral cube. A spectrum was computed solely from the clean components within a $0.25''$ radius centered on the position of the continuum source or the stellar position if the continuum is not detected. If fewer than two channels in the spectrum had intensities less than 3σ between velocities of 0 and 10 km s^{-1} , then no additional fine tuning of the radius and velocity was performed. If two or more channels had intensities greater than 3σ , the procedure moved to optimize the velocity range and then the radius. The velocity range was defined as the largest continuous velocity range that contained clean components around the peak of the line. The radius was defined as the radius that contains 95% of the integrated flux of the cleaned components within a radius of $1''$, twice the FWHM size of the continuum source, or twice the aperture radius, whichever is greater. The aperture radius was manually adjusted for 40 sources based on examination of the results.

The integrated CO flux was computed by summing the channels within the radius and velocity range defined above. The uncertainty in the integrated flux was estimated by randomly placing 100 apertures of the same size and velocity extent within the image cube and computing the standard deviation of the measurements. Table 5 summarizes the CO flux measurements for the 284 sources that were targeted by ALMA. Table 6 presents the CO flux measurements for the additional 40 continuum sources that were detected in the field. The table includes the aperture radius, the velocity extent used to compute the flux, the integrated flux, and the 1σ uncertainty.

To estimate the number of false positive detections from random noise, the automated CO identification procedure was applied toward the stellar positions but for velocities between -50 and -40 km s^{-1} and between 40 and 50 km s^{-1} , where no CO detections are expected. The procedure to identify lines and measuring the CO velocity extent and aperture radius followed that as for actual CO identifications. The open histogram in Figure 7 shows the distribution of these control velocity ranges, where the positive and negative velocity ranges were weighted by half to form the histogram. The maximum signal to noise in the control sample is 2.6. The Upper Sco sample significantly exceeds the control sample for signal-to-noise ratios $\gtrsim 3$, suggesting that most of these measurements are real detections.

5.2. Demographics

As with the continuum data, we now examine the demographics of the CO J=3–2 flux measurements by spectral type and disk type. In addition, we compare the CO J=3–2 and continuum fluxes.

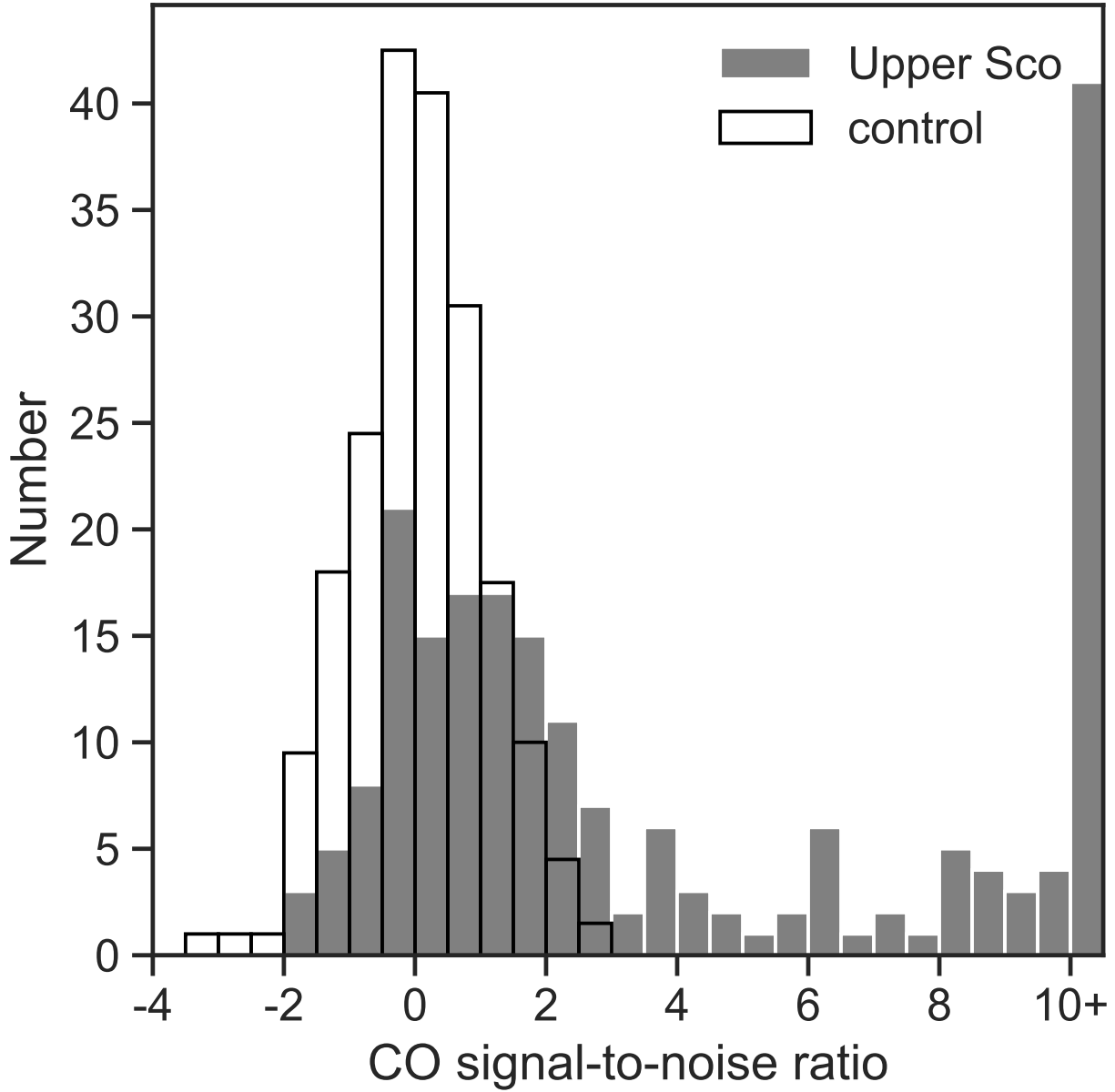


Figure 7. Histogram of the signal-to-noise ratio of the CO J=3–2 integrated intensity for the 199 Upper Sco members (gray histogram) and the control sample (open histogram).

5.2.1. Spectral type

Figure 8 shows the cumulative distribution of CO J=3–2 fluxes for the Upper Sco sample for the full disks. The results show a clear dependence of the submillimeter flux distributions with spectral type. Full disks surrounding stars with spectral types K0–M1.75 are clearly brighter than M2–M3.75 stars ($p = 2 \times 10^{-4}$), which in turn are brighter than the disks around M4–M5 stars ($p = 10^{-4}$). The median CO J=3–2 luminosity for disks around K0–M1.75 stars is $\sim 6\times$ higher than for M2–M3.75 stars and $\sim 23\times$ higher than for M4–M5 stars.

5.2.2. Disk type

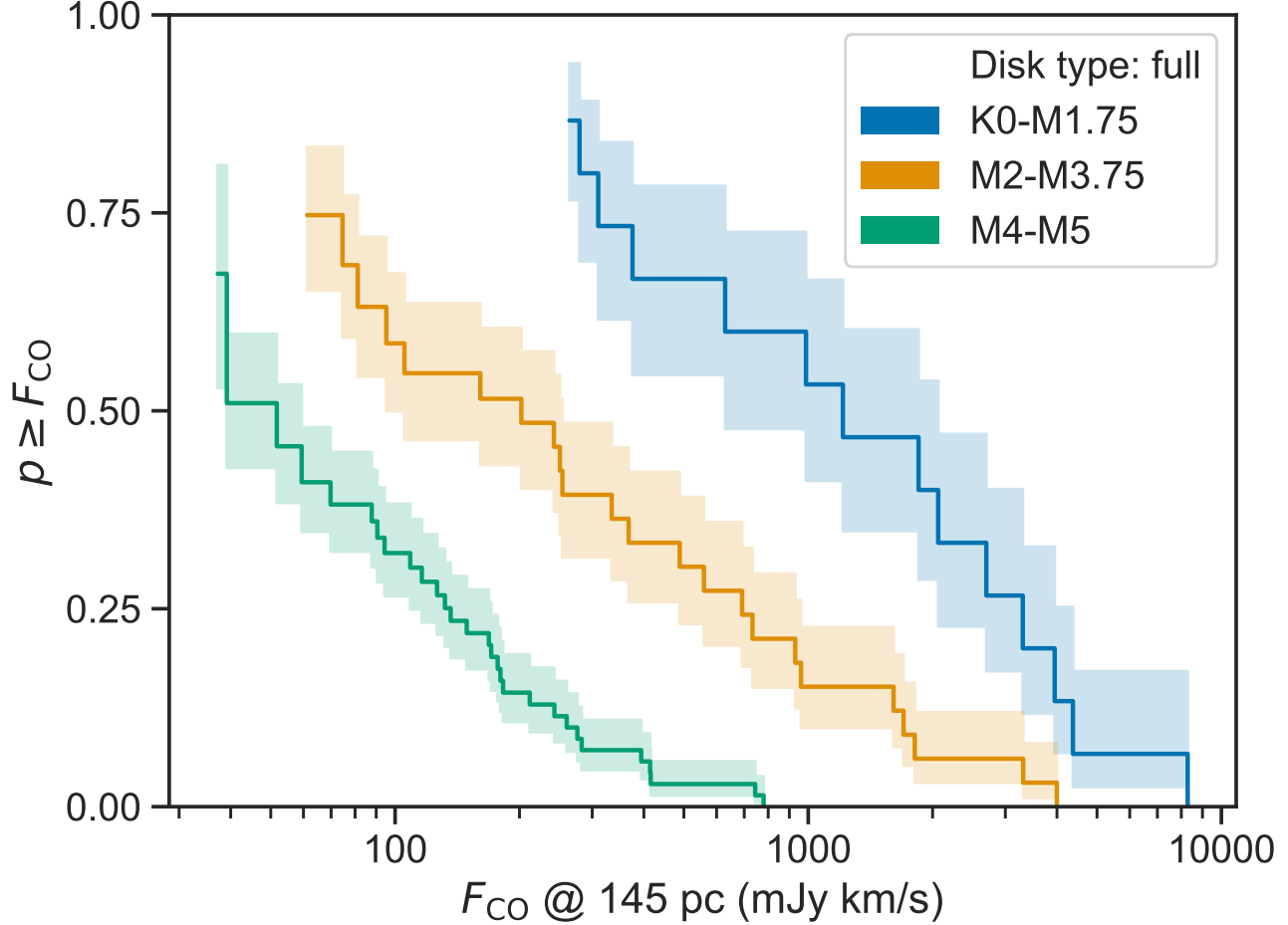


Figure 8. The Kaplan-Meier estimator of the CO J=3–2 fluxes for full disks in Upper Sco, grouped in three spectral type ranges. Fluxes have been scaled to a distance of 145 pc. The results show that earlier spectral types are more luminous in CO than disks around later spectral types.

As in the continuum (see Section 4.2.2), the overall CO J=3–2 detection rate varies with disk type. The detection rates for full and transitional disks are 57% (69/121) and 73% (11/15), respectively. By contrast, evolved disks have a detection rate of 7% (2/28), and only one of the 38 debris-type disks were detected. The one debris-disk type source detected is the Class III source 2MASS J16052076-1821367. As shown in the figure set for Figure 2, continuum emission was not detected toward the stellar position, but there is continuum emission and extended CO emission in the region. Therefore, the CO emission toward this source may be from the ambient cloud and not a disk.

5.2.3. Comparison with the continuum flux

Figure 9 shows the correlation between the CO J=3–2 integrated intensity and the Band 7 continuum flux for the Upper Sco members. In general, the brighter continuum disks are also brighter in CO J=3–2. This general trend is consistent with that previously found in Upper Sco (Barenfeld et al. 2017) and other regions (Long et al. 2022; Sanchis et al. 2021). If both the line and continuum emission are optically thick, such a correlation is expected since both tracers are basically tracing the surface area of the disk, although the spatial extent of the gas tends to be larger than the dust, likely due to radial drift of the dust (Sanchis et al. 2021; Long et al. 2022).

6. DISCUSSION

Given the empirical trends identified in the data, we examine the physical implications and compare the Upper Sco data with other regions.

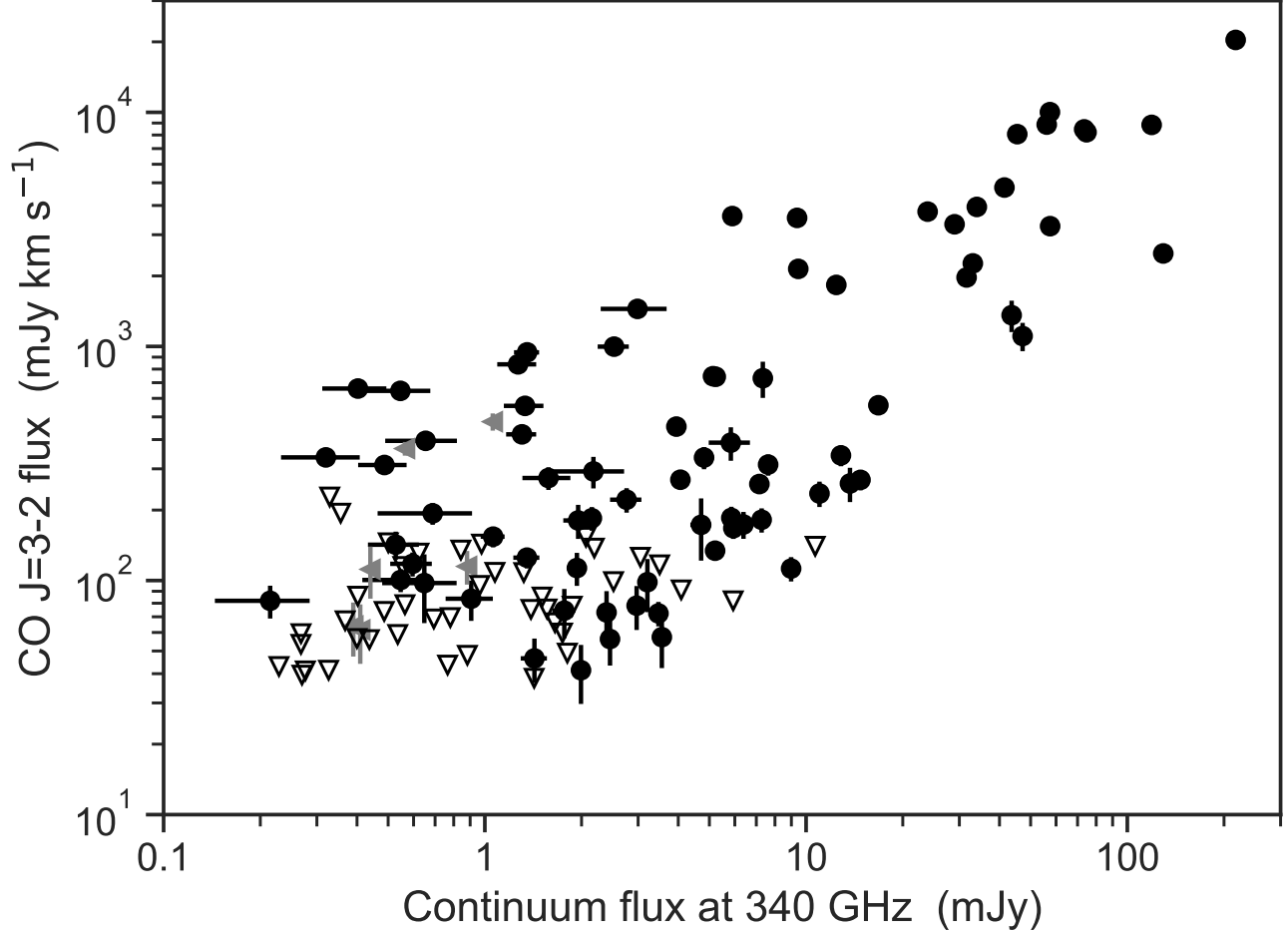


Figure 9. Correlation between the CO J=3–2 integrated intensity and the Band 7 continuum flux for the Upper Sco members. Filled circles indicate 77 sources that are detected in both CO J=3–2 and the continuum. Gray-filled triangles represent six sources detected in CO J=3–2 but not the continuum, and open triangles represent 43 sources detected in the continuum but not CO J=3–2. Non-detections are plotted as 3σ upper limits.

6.1. Variation of luminosity with spectral type

One factor contributing to the difference in submillimeter luminosities with spectral type is that stars with later spectral types have lower stellar luminosities, and thus the dust will tend to be cooler and less luminous. However, the differences in submillimeter luminosities are far larger than can be explained by differences in the stellar luminosities alone. In the Rayleigh-Jeans limit, the submillimeter luminosity will scale linearly with the dust temperature. For optically thin dust emission, a dust grain that emits as a blackbody at radius R_{dust} from the star will have a dust temperature that scales as $L_*^{0.25} R_{\text{dust}}^{-0.5}$. The median submillimeter luminosity around K0–M1.75 stars in Upper Sco is ~ 23 times higher than around M4–M5 stars. Since an early K-type star in Upper Sco is ~ 16 times more luminous than an M5 star (Barenfeld et al. 2016), the stellar luminosity differences can only account for a factor of two difference in the dust luminosities. Alternatively, assuming the Band 7 dust emission is optically thick, the dust continuum emission would be proportional to the disk radius squared. Disks around the later M-type stars would need to be $\sim 5\times$ smaller around later type stars to explain the low luminosities after accounting for the variation in the dust temperature with radius. Barenfeld et al. (2017) found that the size of the continuum disks in Upper Sco is a factor of ~ 3 smaller than found in Ophiuchus, Lupus, and Taurus (Tripathi et al. 2017; Tazzari et al. 2017). Hendl et al. (2020) conducted a more self-consistent analysis and found the median disk size in Upper Sco is a factor of 1.7 times smaller than in Lupus and 1.3 times smaller than in Chamaeleon I. The smaller disk sizes in Upper Sco can account for some but not all of

the differences in the dust continuum luminosities. This suggests that in addition to having a more compact size, the disks around low mass stars have reduced dust column densities and masses compared to disks around higher mass stars. This conclusion is analogous to the disk mass vs. stellar mass correlation that has been previously observed in several regions (Andrews et al. 2013; Pascucci et al. 2016; Ansdell et al. 2016, 2017; Tripathi et al. 2017; Andrews et al. 2018).

6.2. Comparison to other regions

Previous studies have shown that the continuum luminosity of disks in Upper Sco tend to be lower compared to most younger regions, including relative to Taurus (Barenfeld et al. 2016), Lupus (Ansdell et al. 2016), Chamaeleon I (Pascucci et al. 2016), Orion (Eisner et al. 2018), IC 348 (Ruiz-Rodríguez et al. 2018), σ Orionis (Ansdell et al. 2017), and NGC 2024 (van Terwisga et al. 2020). λ Orionis has disk luminosities comparable to Upper Sco, but it also has an older inferred age than nearby star-forming regions (Ansdell et al. 2020). Cazzoletti et al. (2019) found that disks around stars near the Corona Australis cloud have comparable masses as disks in Upper Sco even though the embedded population is much younger (<3 Myr Meyer & Wilking 2009; Sicilia-Aguilar et al. 2011). However, subsequent work has shown that many of those disks reside in an older population surrounding the cloud that is closer to the age of Upper Sco (Esplin & Luhman 2022).

The most common interpretation of the comparison between regions is that the disks in Upper Sco are fainter due to evolutionary effects. Upper Sco tends to be older than the comparison regions, and the fainter disk luminosities are presumed to indicate the depletion of millimeter-sized dust grains in disks with increasing age. However, other factors are known to influence disk evolution, including proximity to massive stars (Ansdell et al. 2017) and stellar multiplicity (Harris et al. 2012; Akeson et al. 2019). Trapman et al. (2020) showed that the sustained higher radiation fields in OB associations could also impact the masses of disks, which could contribute to the luminosity differences in addition to stellar age.

A more refined comparison of the disk luminosities is warranted given the extended ALMA sample. Because of the dependencies on spectral type (see Section 4.2.1 and disk type (see Section 4.2.2), it is important to select stars with similar properties. Accordingly, we compared Upper Sco with submillimeter surveys where spectral types are available and the disks have been classified with the same infrared classifications. These regions include Lupus (Luhman 2020), Ophiuchus (Esplin & Luhman 2020), Taurus (Esplin & Luhman 2019; Luhman 2023), and Chamaeleon I (Luhman et al. 2008; Luhman & Muench 2008; Luhman et al. 2010)

Taurus deserves special mention, since it has been extensively studied at all wavelengths, especially searching for binaries and measuring the submillimeter fluxes for the individual stellar components (Akeson et al. 2019). However, the mid-infrared by *Spitzer* and *WISE* often resolve the individual binary components and the disk classification is for the composite system (Esplin & Luhman 2019). For cases where the disk classification was for the composite system, we assigned the disk type to the primary and removed the secondary from the sample. In one case (CZ Tau), the primary was not detected in the millimeter continuum and the secondary component was, making it ambiguous if the disk classification (full) is appropriate for the primary, the secondary, or both. This star was also excluded from the sample following what was done for Upper Sco.

The observed submillimeter fluxes have been scaled to a common distance of 145 pc using the distances inferred from *Gaia* parallaxes. If the distance is not available from *Gaia* or the uncertainty on the distance is more than 10 pc, then the median distance of the members in the star forming region was used. The submillimeter fluxes were all scaled to a common frequency assuming the submillimeter spectral energy distribution has a slope of $\alpha = 2.2$ (Tazzari et al. 2020) for $S_\nu \propto \nu^\alpha$.

Figure 10 compares the submillimeter continuum flux distribution in Upper Sco to those in Lupus, Ophiuchus, Chamaeleon I, and Taurus, where the comparisons are shown for three different spectral type ranges. The most rigorous comparison would be done by stellar mass instead of spectral type to account for pre-main-sequence evolution between ages of ~ 1 to 10 Myr. However, the change in effective temperature (i.e., spectral type) with stellar age is expected to be small, since pre-main-sequence stars decrease in luminosity with age with small changes in temperature. For example, using the Baraffe et al. (2015) evolutionary models, the photospheric temperature of a 0.1, 0.2, and 0.5 M_\odot star (approximately spectral types of M4.5, M3.5, and M0.5, respectively) varies by ~ 110 K, 50 K, and 150 K between ages of 1 Myr and 10 Myr. This corresponds to a change in spectral type of approximately 1 subclass or less (Pecaut & Mamajek 2013). Therefore, within a spectral type range, the stellar masses should be approximately the same across regions. The comparison shows that for M4–M5 stars, Upper Sco clearly has fainter disk continuum luminosities than

Lupus ($p = 9 \times 10^{-9}$), Ophiuchus ($p = 0.007$), Chamaeleon I ($p = 7 \times 10^{-5}$), and Taurus ($p = 7 \times 10^{-6}$). The same trends are present for M2–M3.75 stars, but any differences are significant only for Taurus ($p = 3 \times 10^{-4}$) and Chamaeleon I ($p=2 \times 10^{-6}$), marginally for Lupus ($p = 0.02$), and not significant for Ophiuchus ($p = 0.87$). For the earliest spectral types shown (K0–M1.75), Upper Sco continues to have fainter disk luminosities, but the most significant difference is for Lupus with $p = 0.007$.

In summary, the disk continuum luminosities tend to be lower in Upper Sco than in other regions as found in previous analyses. The differences are more pronounced in the later (M4–M5) spectral types than in earlier type stars (K–M1.75). This trend with spectral type is analogous to the results in [Pascucci et al. \(2016\)](#), who found that the disk luminosity-stellar mass relation steepens with stellar age. They suggest this trend can be explained by models incorporating grain growth, fragmentation, and radial drift where, if disks are in the fragmentation regime, the timescale over which dust is depleted is faster in lower mass stars.

6.3. Clusters in Upper Sco

[Ratzenböck et al. \(2023a\)](#) identified nine clusters within Upper Sco that are co-spatial and co-moving based on the precise astrometry from *Gaia*. The ages of clusters inferred by placing the stars in the Hertzsprung-Russell (H-R) diagram range from approximately 4 Myr to 19 Myr ([Ratzenböck et al. 2023b](#)) when adopting the PARSEC models ([Marigo et al. 2017](#)) and the *Gaia G, G_{BP}, and G_{RP}* photometry.

Of the 202 stars analyzed in this paper as Upper Sco members as defined in [Luhman \(2022b\)](#), 200 appear in the analysis by [Ratzenböck et al. \(2023a\)](#), all of which are associated with one of the Upper Sco clusters. In contrast, of the 284 stars presented in this paper, 248 are associated with a cluster in [Ratzenböck et al. \(2023a\)](#), of which 40 are defined as an Upper Sco member in [Ratzenböck et al. \(2023a\)](#) but not in [Luhman \(2022b\)](#). It is beyond the scope of this paper to analyze the formal definition of Upper Sco, so here we consider the 200 stars that are defined as Upper Sco members by both [Ratzenböck et al. \(2023a\)](#) and [Luhman \(2022b\)](#).

To investigate if the continuum properties of the disks vary amongst the clusters defined in [Ratzenböck et al. \(2023a\)](#), we grouped clusters 1 and 2 (age 3.8–5.8 Myr), clusters 3 and 4 (age 7.6–9.8 Myr), and clusters 5 and 6 (age 10–12.7 Myr). Considering full disks only, this resulted in a sample of 30, 75, and 16 stars, respectively. None of the Upper Sco members defined here with disks are members of clusters 7, 8, and 9 in [Ratzenböck et al. \(2023a\)](#).

Figure 11 shows the cumulative distributions of Band 7 continuum fluxes grouped by spectral type in the panels and by cluster within a panel. For the spectral-type ranges considered here, no significant differences are observed in the flux distributions for the clusters. The most significant difference is for M4–M5 stars in clusters 5–6, which tend to have less luminous disks than clusters 1–2 ($p = 0.009$) and 3–4 ($p = 0.04$). Although this is consistent with less luminous disks at older ages, the probabilities are only marginally significant. In addition, there are no obvious differences in the flux distributions for the other spectral types. Any differences in the dust continuum luminosity distributions between the clusters are evidently less than those observed between regions (Figure 10). Therefore, if there is any disk evolution between the clusters, it is not readily apparent in the submillimeter continuum fluxes of the surviving disks.

7. SUMMARY

The Upper Sco OB association is one of the benchmark regions for measuring the evolution of protoplanetary disks. It represents the largest collection of ~ 10 Myr stars in the solar neighborhood and it is at comparable distances to the young (1 Myr) star forming regions. Since the initial ALMA studies of disks in Upper Sco ([Carpenter et al. 2014; Barenfeld et al. 2016, 2017](#)), the census of the disk population of the association has more than doubled through a combination of ground-based spectroscopy, *Gaia* astrometry, and mid-IR photometry from *WISE* ([Esplin et al. 2018; Luhman & Esplin 2020; Luhman 2022a](#)). In this study, we have presented ALMA data for newly identified disks in Upper Sco. The observations were obtained in the Band 7 (340 GHz) continuum and in CO J=3–2. Combined with previous observations, the full sample contains 284 stars. Of these stars, 208 are now considered Upper Sco members based on *Gaia* kinematics, and 202 form the sample studied here after removing possible contaminants (see Appendix B). Of the 202 Upper Sco members analyzed here, 120 have been detected in the Band 7 continuum and 83 in CO J=3–2 with a signal-to-noise ratio of ≥ 3 .

The expanded sample reinforces the conclusions of previous studies. For full disks, the submillimeter luminosities show a trend with stellar spectral type in that disks around later-type stars are fainter the submillimeter continuum than disks around earlier type stars for spectral types between K0 and M5. The magnitude of the difference cannot

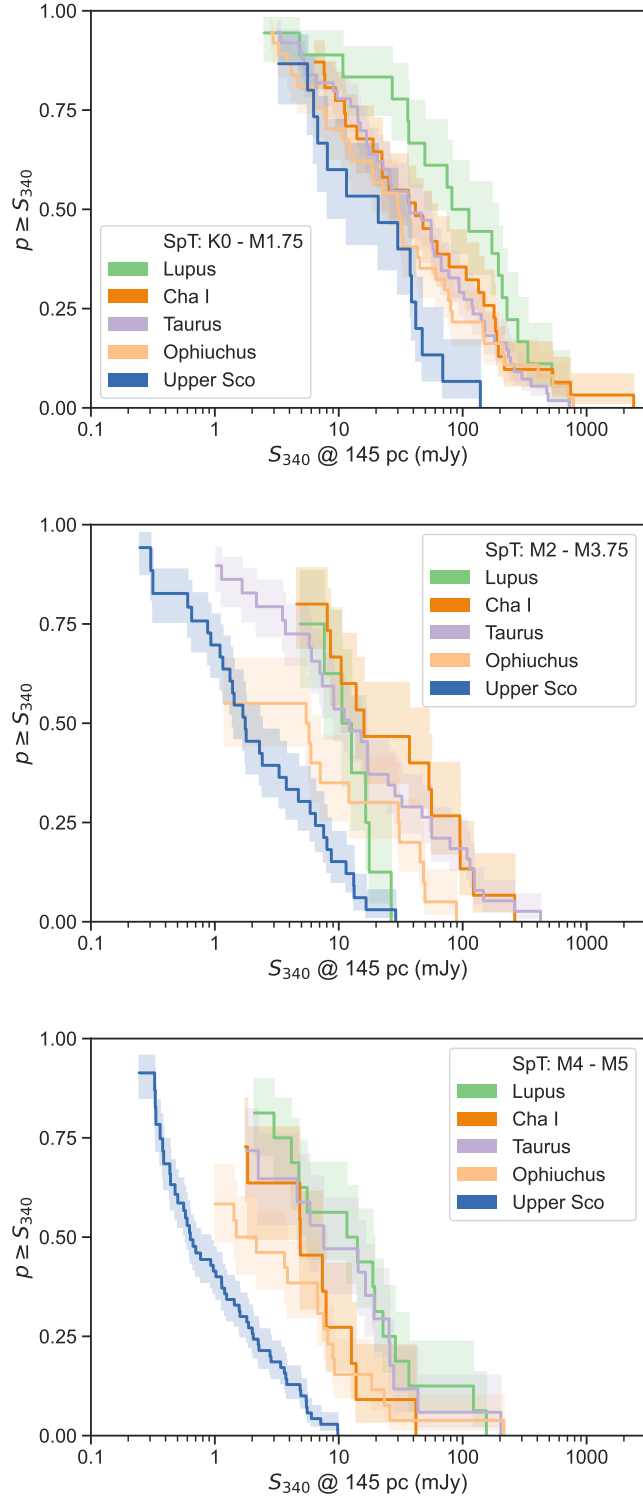


Figure 10. The Kaplan-Meier estimator of the submillimeter fluxes at 340 GHz for full disks in Lupus (Ansdel et al. 2016), Ophiuchus (Williams et al. 2019), Taurus (Akeson et al. 2019), Chamaeleon I (Pascucci et al. 2016), and Upper Sco (this paper). Each panel shows the results for different spectral type ranges. Only disks classified as full are shown. All fluxes have been scaled to a distance of 145 pc.

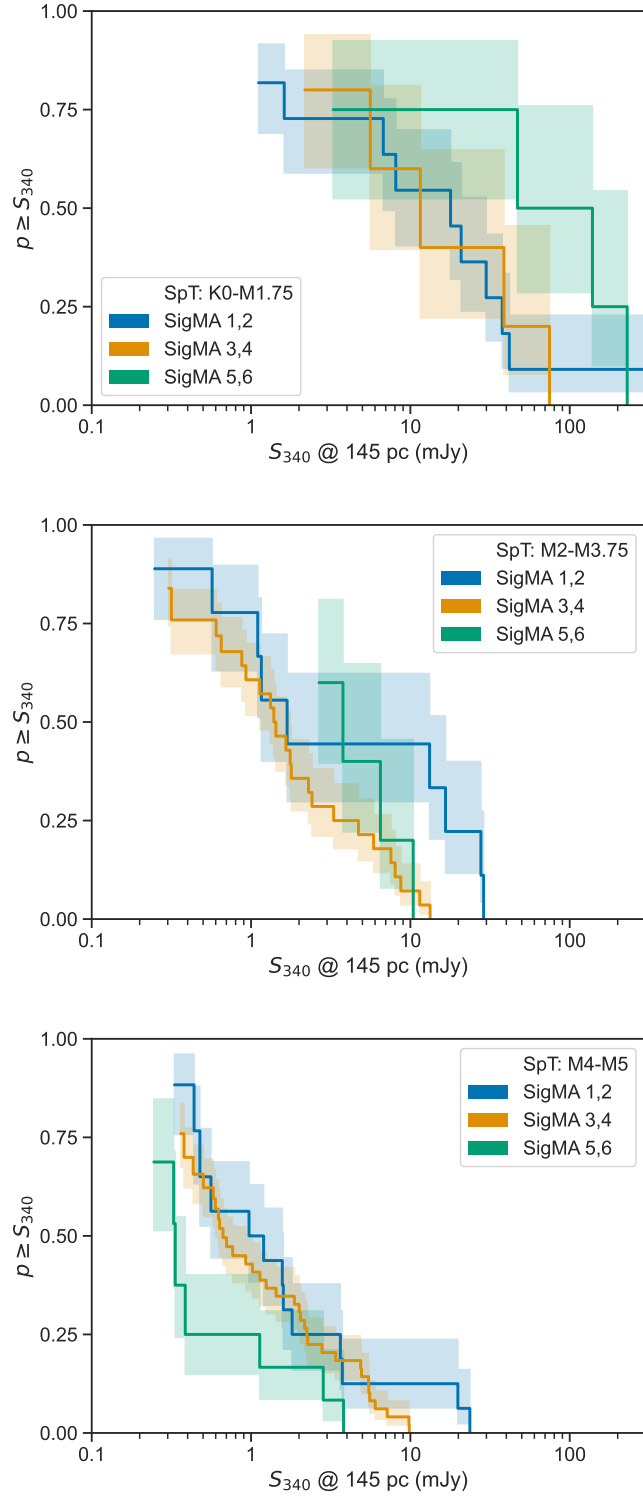


Figure 11. The Kaplan-Meier estimator of the Band 7 continuum fluxes for full disks in Upper Sco for stars with spectral type K0 to M1.75 (top panel), M2 to M3.75 (middle panel), and M4 to M5 (bottom panel). Within each panel, distributions are shown for members of the Upper Sco clusters identified by Ratzenböck et al. (2023a).

be explained by the differences in stellar luminosities or the differences in the typical disk size (Barenfeld et al. 2017; Hendl et al. 2020), and may indicate reduces dust masses for the later type stars as found in previous studies (Andrews et al. 2013; Pascucci et al. 2016; Ansdell et al. 2016). The CO J=3–2 integrated intensities also show a clear variations with spectral type, as the median CO flux around K0–M1.75 stars is $\sim 23\times$ brighter than M4–M5 stars.

The dust luminosities in Upper Sco were compared with nearby star forming regions. As found in previous studies (see review by Manara et al. 2023), stars with full disks tend to have fainter submillimeter luminosities in Upper Sco compared to younger regions. The difference is most pronounced for later spectral types (M4–M5) than earlier spectral types (K0–M1.75).

We thank the referee for carefully reviewing the manuscript. This paper makes use of the following ALMA data: ADS/JAO.ALMA#2011.0.00526.S, ADS/JAO.ALMA#2013.1.00395.S, and ADS/JAO.ALMA#2018.1.00564.S. ALMA is a partnership of ESO (representing its member states), NSF (USA) and NINS (Japan), together with NRC (Canada), NSTC and ASIAA (Taiwan), and KASI (Republic of Korea), in cooperation with the Republic of Chile. The Joint ALMA Observatory is operated by ESO, AUI/NRAO and NAOJ. The National Radio Astronomy Observatory is a facility of the National Science Foundation operated under cooperative agreement by Associated Universities, Inc. This research has made use of the VizieR catalog access tool, CDS, Strasbourg, France (DOI: 10.26093/cds/vizier). Part of this research was carried out at the Jet Propulsion Laboratory, California Institute of Technology, under a contract with the National Aeronautics and Space Administration (80NM0018D0004).

Facility: ALMA

Software: `Astropy` (Astropy Collaboration et al. 2013, 2018), `CASA` (McMullin et al. 2007), `corner` (Foreman-Mackey 2016), `emcee` (Foreman-Mackey et al. 2013), `EnvStats` (Millard 2013), `Lifelines` (Davidson-Pilon et al. 2019), `R` (R Core Team 2017)

REFERENCES

- Akeson, R. L., Jensen, E. L. N., Carpenter, J., et al. 2019, *ApJ*, 872, 158, doi: [10.3847/1538-4357/aaff6a](https://doi.org/10.3847/1538-4357/aaff6a)
- Andrews, S. M., Rosenfeld, K. A., Kraus, A. L., & Wilner, D. J. 2013, *ApJ*, 771, 129, doi: [10.1088/0004-637X/771/2/129](https://doi.org/10.1088/0004-637X/771/2/129)
- Andrews, S. M., Terrell, M., Tripathi, A., et al. 2018, *ApJ*, 865, 157, doi: [10.3847/1538-4357/aadd9f](https://doi.org/10.3847/1538-4357/aadd9f)
- Ansdell, M., Williams, J. P., Manara, C. F., et al. 2017, *AJ*, 153, 240, doi: [10.3847/1538-3881/aa69c0](https://doi.org/10.3847/1538-3881/aa69c0)
- Ansdell, M., Williams, J. P., van der Marel, N., et al. 2016, *ApJ*, 828, 46, doi: [10.3847/0004-637X/828/1/46](https://doi.org/10.3847/0004-637X/828/1/46)
- Ansdell, M., Haworth, T. J., Williams, J. P., et al. 2020, *AJ*, 160, 248, doi: [10.3847/1538-3881/abb9af](https://doi.org/10.3847/1538-3881/abb9af)
- Aru, M. L., Maucó, K., Manara, C. F., et al. 2024, *A&A*, 687, A93, doi: [10.1051/0004-6361/202349004](https://doi.org/10.1051/0004-6361/202349004)
- Astropy Collaboration, Robitaille, T. P., Tollerud, E. J., et al. 2013, *A&A*, 558, A33, doi: [10.1051/0004-6361/201322068](https://doi.org/10.1051/0004-6361/201322068)
- Astropy Collaboration, Price-Whelan, A. M., SipHocz, B. M., et al. 2018, *aj*, 156, 123, doi: [10.3847/1538-3881/aaabc4f](https://doi.org/10.3847/1538-3881/aaabc4f)
- Bailer-Jones, C. A. L., Rybizki, J., Fouesneau, M., Demleitner, M., & Andrae, R. 2021, *AJ*, 161, 147, doi: [10.3847/1538-3881/ab806](https://doi.org/10.3847/1538-3881/ab806)
- Baraffe, I., Homeier, D., Allard, F., & Chabrier, G. 2015, *A&A*, 577, A42, doi: [10.1051/0004-6361/201425481](https://doi.org/10.1051/0004-6361/201425481)
- Barenfeld, S. A., Carpenter, J. M., Ricci, L., & Isella, A. 2016, *ApJ*, 827, 142, doi: [10.3847/0004-637X/827/2/142](https://doi.org/10.3847/0004-637X/827/2/142)
- Barenfeld, S. A., Carpenter, J. M., Sargent, A. I., Isella, A., & Ricci, L. 2017, *ApJ*, 851, 85, doi: [10.3847/1538-4357/aa989d](https://doi.org/10.3847/1538-4357/aa989d)
- Barenfeld, S. A., Carpenter, J. M., Sargent, A. I., et al. 2019, *ApJ*, 878, 45, doi: [10.3847/1538-4357/ab1e50](https://doi.org/10.3847/1538-4357/ab1e50)
- Briceño, C., Calvet, N., Hernández, J., et al. 2019, *AJ*, 157, 85, doi: [10.3847/1538-3881/aaf79b](https://doi.org/10.3847/1538-3881/aaf79b)
- Carpenter, J. M., Ricci, L., & Isella, A. 2014, *ApJ*, 787, 42, doi: [10.1088/0004-637X/787/1/42](https://doi.org/10.1088/0004-637X/787/1/42)
- CASA Team, Bean, B., Bhatnagar, S., et al. 2022, *PASP*, 134, 114501, doi: [10.1088/1538-3873/ac9642](https://doi.org/10.1088/1538-3873/ac9642)
- Cazzoletti, P., Manara, C. F., Baobab Liu, H., et al. 2019, *A&A*, 626, A11, doi: [10.1051/0004-6361/201935273](https://doi.org/10.1051/0004-6361/201935273)
- Cleeves, L. I., Öberg, K. I., Wilner, D. J., et al. 2016, *ApJ*, 832, 110, doi: [10.3847/0004-637X/832/2/110](https://doi.org/10.3847/0004-637X/832/2/110)
- Davidson-Pilon, C., Kalderstam, J., Zivich, P., et al. 2019, CamDavidsonPilon/lifelines: v0.23.0, v0.25.4, Zenodo, doi: [10.5281/zenodo.3544808](https://doi.org/10.5281/zenodo.3544808)
- de Bruijne, J. H. J. 2012, *Ap&SS*, 341, 31, doi: [10.1007/s10509-012-1019-4](https://doi.org/10.1007/s10509-012-1019-4)
- de Zeeuw, P. T., Hoogerwerf, R., de Bruijne, J. H. J., Brown, A. G. A., & Blaauw, A. 1999, *AJ*, 117, 354, doi: [10.1086/300682](https://doi.org/10.1086/300682)
- Eisner, J. A., Arce, H. G., Ballering, N. P., et al. 2018, *ApJ*, 860, 77, doi: [10.3847/1538-4357/aac3e2](https://doi.org/10.3847/1538-4357/aac3e2)
- Esplin, T. L., & Luhman, K. L. 2019, *AJ*, 158, 54, doi: [10.3847/1538-3881/ab2594](https://doi.org/10.3847/1538-3881/ab2594)
- . 2020, *AJ*, 159, 282, doi: [10.3847/1538-3881/ab8dbd](https://doi.org/10.3847/1538-3881/ab8dbd)
- . 2022, *AJ*, 163, 64, doi: [10.3847/1538-3881/ac3e64](https://doi.org/10.3847/1538-3881/ac3e64)
- Esplin, T. L., Luhman, K. L., Miller, E. B., & Mamajek, E. E. 2018, *AJ*, 156, 75, doi: [10.3847/1538-3881/aacce0](https://doi.org/10.3847/1538-3881/aacce0)
- Fedele, D., van den Ancker, M. E., Henning, T., Jayawardhana, R., & Oliveira, J. M. 2010, *A&A*, 510, A72, doi: [10.1051/0004-6361/200912810](https://doi.org/10.1051/0004-6361/200912810)
- Feiden, G. A. 2016, *A&A*, 593, A99, doi: [10.1051/0004-6361/201527613](https://doi.org/10.1051/0004-6361/201527613)
- Feiden, G. A., & Chaboyer, B. 2012, *ApJ*, 761, 30, doi: [10.1088/0004-637X/761/1/30](https://doi.org/10.1088/0004-637X/761/1/30)
- . 2013, *ApJ*, 779, 183, doi: [10.1088/0004-637X/779/2/183](https://doi.org/10.1088/0004-637X/779/2/183)
- Flagey, N., Noriega-Crespo, A., Boulanger, F., et al. 2009, *ApJ*, 701, 1450, doi: [10.1088/0004-637X/701/2/1450](https://doi.org/10.1088/0004-637X/701/2/1450)
- Foreman-Mackey, D. 2016, *The Journal of Open Source Software*, 1, 24, doi: [10.21105/joss.00024](https://doi.org/10.21105/joss.00024)
- Foreman-Mackey, D., Hogg, D. W., Lang, D., & Goodman, J. 2013, *PASP*, 125, 306, doi: [10.1086/670067](https://doi.org/10.1086/670067)
- Gaia Collaboration, Prusti, T., de Bruijne, J. H. J., et al. 2016, *A&A*, 595, A1, doi: [10.1051/0004-6361/201629272](https://doi.org/10.1051/0004-6361/201629272)
- Gaia Collaboration, Brown, A. G. A., Vallenari, A., et al. 2018, *A&A*, 616, A1, doi: [10.1051/0004-6361/201833051](https://doi.org/10.1051/0004-6361/201833051)
- . 2021, *A&A*, 649, A1, doi: [10.1051/0004-6361/202039657](https://doi.org/10.1051/0004-6361/202039657)
- Gaia Collaboration, Vallenari, A., Brown, A. G. A., et al. 2023, *A&A*, 674, A1, doi: [10.1051/0004-6361/202243940](https://doi.org/10.1051/0004-6361/202243940)
- Garufi, A., Avenhaus, H., Pérez, S., et al. 2020, *A&A*, 633, A82, doi: [10.1051/0004-6361/201936946](https://doi.org/10.1051/0004-6361/201936946)
- Grant, S. L., Espaillat, C. C., Wendeborn, J., et al. 2021, *ApJ*, 913, 123, doi: [10.3847/1538-4357/abf432](https://doi.org/10.3847/1538-4357/abf432)
- Haisch, Karl E., J., Lada, E. A., & Lada, C. J. 2001, *ApJL*, 553, L153, doi: [10.1086/320685](https://doi.org/10.1086/320685)
- Harris, R. J., Andrews, S. M., Wilner, D. J., & Kraus, A. L. 2012, *ApJ*, 751, 115, doi: [10.1088/0004-637X/751/2/115](https://doi.org/10.1088/0004-637X/751/2/115)
- Hartmann, L., Herczeg, G., & Calvet, N. 2016, *ARA&A*, 54, 135, doi: [10.1146/annurev-astro-081915-023347](https://doi.org/10.1146/annurev-astro-081915-023347)
- Hendler, N., Pascucci, I., Pinilla, P., et al. 2020, *ApJ*, 895, 126, doi: [10.3847/1538-4357/ab70ba](https://doi.org/10.3847/1538-4357/ab70ba)
- Hernández, J., Calvet, N., Hartmann, L., et al. 2005, *AJ*, 129, 856, doi: [10.1086/426918](https://doi.org/10.1086/426918)
- Ingleby, L., Calvet, N., Hernández, J., et al. 2014, *ApJ*, 790, 47, doi: [10.1088/0004-637X/790/1/47](https://doi.org/10.1088/0004-637X/790/1/47)

- Kerr, R. M. P., Rizzuto, A. C., Kraus, A. L., & Offner, S. S. R. 2021, ApJ, 917, 23, doi: [10.3847/1538-4357/ac0251](https://doi.org/10.3847/1538-4357/ac0251)
- Köhler, R., Kunkel, M., Leinert, C., & Zinnecker, H. 2000, A&A, 356, 541
- Kouwenhoven, M. B. N., Brown, A. G. A., Zinnecker, H., Kaper, L., & Portegies Zwart, S. F. 2005, A&A, 430, 137, doi: [10.1051/0004-6361:20048124](https://doi.org/10.1051/0004-6361:20048124)
- Kraus, A. L., & Hillenbrand, L. A. 2012, ApJ, 757, 141, doi: [10.1088/0004-637X/757/2/141](https://doi.org/10.1088/0004-637X/757/2/141)
- Lafrenière, D., Jayawardhana, R., van Kerwijk, M. H., Brandeker, A., & Janson, M. 2014, ApJ, 785, 47, doi: [10.1088/0004-637X/785/1/47](https://doi.org/10.1088/0004-637X/785/1/47)
- Long, F., Andrews, S. M., Rosotti, G., et al. 2022, ApJ, 931, 6, doi: [10.3847/1538-4357/ac634e](https://doi.org/10.3847/1538-4357/ac634e)
- Luhman, K. L. 2020, AJ, 160, 186, doi: [10.3847/1538-3881/abb12f](https://doi.org/10.3847/1538-3881/abb12f)
- . 2022a, AJ, 163, 25, doi: [10.3847/1538-3881/ac35e3](https://doi.org/10.3847/1538-3881/ac35e3)
- . 2022b, AJ, 163, 24, doi: [10.3847/1538-3881/ac35e2](https://doi.org/10.3847/1538-3881/ac35e2)
- . 2023, AJ, 165, 37, doi: [10.3847/1538-3881/ac9da3](https://doi.org/10.3847/1538-3881/ac9da3)
- Luhman, K. L., Allen, P. R., Espaillat, C., Hartmann, L., & Calvet, N. 2010, ApJS, 186, 111, doi: [10.1088/0067-0049/186/1/111](https://doi.org/10.1088/0067-0049/186/1/111)
- Luhman, K. L., & Esplin, T. L. 2020, AJ, 160, 44, doi: [10.3847/1538-3881/ab9599](https://doi.org/10.3847/1538-3881/ab9599)
- Luhman, K. L., Herrmann, K. A., Mamajek, E. E., Esplin, T. L., & Pecaut, M. J. 2018, AJ, 156, 76, doi: [10.3847/1538-3881/aacc6d](https://doi.org/10.3847/1538-3881/aacc6d)
- Luhman, K. L., & Muench, A. A. 2008, ApJ, 684, 654, doi: [10.1086/590364](https://doi.org/10.1086/590364)
- Luhman, K. L., Allen, L. E., Allen, P. R., et al. 2008, ApJ, 675, 1375, doi: [10.1086/527347](https://doi.org/10.1086/527347)
- Maeshima, H., Nakagawa, T., Kojima, T., Takita, S., & Kwon, J. 2021, PASJ, 73, 1589, doi: [10.1093/pasj/psab095](https://doi.org/10.1093/pasj/psab095)
- Mahieu, S., Maier, D., Lazareff, B., et al. 2012, IEEE Transactions on Terahertz Science and Technology, 2, 29, doi: [10.1109/TTHZ.2011.2177734](https://doi.org/10.1109/TTHZ.2011.2177734)
- Mamajek, E. E. 2009, in American Institute of Physics Conference Series, Vol. 1158, Exoplanets and Disks: Their Formation and Diversity, ed. T. Usuda, M. Tamura, & M. Ishii, 3–10
- Manara, C. F., Ansdell, M., Rosotti, G. P., et al. 2023, in Astronomical Society of the Pacific Conference Series, Vol. 534, Protostars and Planets VII, ed. S. Inutsuka, Y. Aikawa, T. Muto, K. Tomida, & M. Tamura, 539
- Manara, C. F., Natta, A., Rosotti, G. P., et al. 2020, A&A, 639, A58, doi: [10.1051/0004-6361/202037949](https://doi.org/10.1051/0004-6361/202037949)
- Marigo, P., Girardi, L., Bressan, A., et al. 2017, ApJ, 835, 77, doi: [10.3847/1538-4357/835/1/77](https://doi.org/10.3847/1538-4357/835/1/77)
- Mathews, G. S., Williams, J. P., Ménard, F., et al. 2012, ApJ, 745, 23, doi: [10.1088/0004-637X/745/1/23](https://doi.org/10.1088/0004-637X/745/1/23)
- Maucó, K., Manara, C. F., Ansdell, M., et al. 2023, A&A, 679, A82, doi: [10.1051/0004-6361/202347627](https://doi.org/10.1051/0004-6361/202347627)
- McMullin, J. P., Waters, B., Schiebel, D., Young, W., & Golap, K. 2007, in Astronomical Society of the Pacific Conference Series, Vol. 376, Astronomical Data Analysis Software and Systems XVI, ed. R. A. Shaw, F. Hill, & D. J. Bell, 127
- Metchev, S. A., & Hillenbrand, L. A. 2009, ApJS, 181, 62, doi: [10.1088/0067-0049/181/1/62](https://doi.org/10.1088/0067-0049/181/1/62)
- Meyer, M. R., & Wilking, B. A. 2009, PASP, 121, 350, doi: [10.1086/598804](https://doi.org/10.1086/598804)
- Millard, S. P. 2013, EnvStats: An R Package for Environmental Statistics, Use R! (New York, NY: Springer), doi: [10.1007/978-1-4614-8456-1](https://doi.org/10.1007/978-1-4614-8456-1)
<https://www.springer.com>
- Muzerolle, J., Calvet, N., Briceño, C., Hartmann, L., & Hillenbrand, L. 2000, ApJL, 535, L47, doi: [10.1086/312691](https://doi.org/10.1086/312691)
- Pascucci, I., Testi, L., Herczeg, G. J., et al. 2016, ApJ, 831, 125, doi: [10.3847/0004-637X/831/2/125](https://doi.org/10.3847/0004-637X/831/2/125)
- Pecaut, M. J., & Mamajek, E. E. 2013, ApJS, 208, 9, doi: [10.1088/0067-0049/208/1/9](https://doi.org/10.1088/0067-0049/208/1/9)
- Pecaut, M. J., Mamajek, E. E., & Bubar, E. J. 2012, ApJ, 746, 154, doi: [10.1088/0004-637X/746/2/154](https://doi.org/10.1088/0004-637X/746/2/154)
- Perryman, M. A. C., de Boer, K. S., Gilmore, G., et al. 2001, A&A, 369, 339, doi: [10.1051/0004-6361:20010085](https://doi.org/10.1051/0004-6361:20010085)
- Preibisch, T., Brown, A. G. A., Bridges, T., Guenther, E., & Zinnecker, H. 2002, AJ, 124, 404, doi: [10.1086/341174](https://doi.org/10.1086/341174)
- R Core Team. 2017, R: A Language and Environment for Statistical Computing, R Foundation for Statistical Computing, Vienna, Austria
- Ratzenböck, S., Großschedl, J. E., Möller, T., et al. 2023a, A&A, 677, A59, doi: [10.1051/0004-6361/202243690](https://doi.org/10.1051/0004-6361/202243690)
- Ratzenböck, S., Großschedl, J. E., Alves, J., et al. 2023b, A&A, 678, A71, doi: [10.1051/0004-6361/202346901](https://doi.org/10.1051/0004-6361/202346901)
- Ribas, Á., Bouy, H., & Merín, B. 2015, A&A, 576, A52, doi: [10.1051/0004-6361/201424846](https://doi.org/10.1051/0004-6361/201424846)
- Ribas, Á., Merín, B., Bouy, H., & Maud, L. T. 2014, A&A, 561, A54, doi: [10.1051/0004-6361/201322597](https://doi.org/10.1051/0004-6361/201322597)
- Rosotti, G. P., Tazzari, M., Booth, R. A., et al. 2019, MNRAS, 486, 4829, doi: [10.1093/mnras/stz1190](https://doi.org/10.1093/mnras/stz1190)
- Ruiz-Rodríguez, D., Cieza, L. A., Williams, J. P., et al. 2018, MNRAS, 478, 3674, doi: [10.1093/mnras/sty1351](https://doi.org/10.1093/mnras/sty1351)
- Sanchis, E., Testi, L., Natta, A., et al. 2021, arXiv e-prints, arXiv:2101.11307. <https://arxiv.org/abs/2101.11307>
- Sicilia-Aguilar, A., Henning, T., & Hartmann, L. W. 2010, ApJ, 710, 597, doi: [10.1088/0004-637X/710/1/597](https://doi.org/10.1088/0004-637X/710/1/597)

- Sicilia-Aguilar, A., Henning, T., Kainulainen, J., & Roccagliata, V. 2011, ApJ, 736, 137,
doi: [10.1088/0004-637X/736/2/137](https://doi.org/10.1088/0004-637X/736/2/137)
- Sierra, A., Pérez, L. M., Agurto-Gangas, C., et al. 2024,
arXiv e-prints, arXiv:2407.16651,
doi: [10.48550/arXiv.2407.16651](https://doi.org/10.48550/arXiv.2407.16651)
- Slesnick, C. L., Hillenbrand, L. A., & Carpenter, J. M. 2008, ApJ, 688, 377, doi: [10.1086/592265](https://doi.org/10.1086/592265)
- Tazzari, M., Testi, L., Natta, A., et al. 2017, A&A, 606, A88, doi: [10.1051/0004-6361/201730890](https://doi.org/10.1051/0004-6361/201730890)
—. 2020, arXiv e-prints, arXiv:2010.02248.
<https://arxiv.org/abs/2010.02248>
- Tokovinin, A., & Briceño, C. 2020, AJ, 159, 15,
doi: [10.3847/1538-3881/ab5525](https://doi.org/10.3847/1538-3881/ab5525)
- Trapman, L., Rosotti, G., Bosman, A. D., Hogerheijde, M. R., & van Dishoeck, E. F. 2020, A&A, 640, A5,
doi: [10.1051/0004-6361/202037673](https://doi.org/10.1051/0004-6361/202037673)
- Tripathi, A., Andrews, S. M., Birnstiel, T., & Wilner, D. J. 2017, ApJ, 845, 44, doi: [10.3847/1538-4357/aa7c62](https://doi.org/10.3847/1538-4357/aa7c62)
- van Terwisga, S. E., Hacar, A., van Dishoeck, E. F., Oonk, R., & Portegies Zwart, S. 2022, A&A, 661, A53,
doi: [10.1051/0004-6361/202141913](https://doi.org/10.1051/0004-6361/202141913)
- van Terwisga, S. E., van Dishoeck, E. F., Mann, R. K., et al. 2020, A&A, 640, A27, doi: [10.1051/0004-6361/201937403](https://doi.org/10.1051/0004-6361/201937403)
- Williams, J. P., Cieza, L., Hales, A., et al. 2019, ApJL, 875, L9, doi: [10.3847/2041-8213/ab1338](https://doi.org/10.3847/2041-8213/ab1338)
- Wright, N. J., & Mamajek, E. E. 2018, MNRAS, 476, 381,
doi: [10.1093/mnras/sty207](https://doi.org/10.1093/mnras/sty207)
- Zagaria, F., Rosotti, G. P., Clarke, C. J., & Tabone, B. 2022, MNRAS, 514, 1088, doi: [10.1093/mnras/stac1461](https://doi.org/10.1093/mnras/stac1461)
- Zhang, K., Isella, A., Carpenter, J. M., & Blake, G. A. 2014, ApJ, 791, 42, doi: [10.1088/0004-637X/791/1/42](https://doi.org/10.1088/0004-637X/791/1/42)

APPENDIX

A. CORNER PLOTS FOR THE CONTINUUM VISIBILITY GAUSSIAN FITS

Figure 12 presents the corner plot (Foreman-Mackey 2016) that summarizes the parameters from the Gaussian fit to the continuum visibilities for 2MASS J15354856-2958551. Similar plots for sources that were fitted with a Gaussian are shown in the figure set. In cases where multiple source components were fitted to the visibilities, only the parameters associated with the intended stellar target are shown.

Fig. Set 13. Corner plots for the Gaussian fits to the continuum visibilities

B. IDENTIFICATION OF THE ALMA SOURCES

This section analyzes the ALMA continuum sources to identify which sources are coincident with the targeted star and which may be contaminants, either from galaxies, binary companions, or other members of Upper Sco. The stellar astrometry is derived from the Gaia EDR3 and include corrections for proper motion to the epoch of the ALMA observation. Twenty-four sources do not have a proper motion listed in *Gaia* EDR3. For these sources, the median proper motion of the sample was used according to the defined group; i.e., for Upper Sco members, the median proper motion of all Upper Sco members was used and for non-Upper Sco members, the median proper motion of non-Upper Sco members was used.

In addition to the *Gaia* sources, ALMA sources were matched with sources detected from optical and infrared multiplicity surveys of Upper Sco. Table 5 in Tokovinin & Briceño (2020) summarized the binary companions in Upper Sco based on their own observations and from Köhler et al. (2000), Kouwenhoven et al. (2005), Metchev & Hillenbrand (2009), Kraus & Hillenbrand (2012), and Lafrenière et al. (2014). ALMA sources were also matched with the multiplicity survey of Barenfeld et al. (2019, see also Garufi et al. 2020).

Figure 13 shows the offsets of the ALMA continuum detections (defined as sources with a signal-to-noise ratio of at least 3) to the stellar position within $\pm 1''$. Of the 150 sources represented in this figure, 93% have a separation between the ALMA source and the expected stellar position of $\leq 0''.2$, with a mean of $0''.052$ and a dispersion of $0''.042$. We assume for these sources that the ALMA continuum source is associated with the star with the exception of 2MASS J15442550-2126408, where the ALMA continuum source is more closely aligned with a binary (Tokovinin & Briceño 2020). For the ALMA continuum detections that are more than $0''.2$ in separation from the expected stellar position, we assume the ALMA source is not associated with the star, as it may be an extragalactic contaminant, a binary, or other member of Upper Sco.

We can estimate contamination based on the source detection statistics in the ALMA images. A total of 25 sources were detected with a flux density ≥ 1 mJy between $0''.35$ and $5''$ of the stellar position. Such sources could be detected in 231 of the images at a signal-to-noise ratio of at least 5. Assuming conservatively that these are all extragalactic sources, we expect to detect ~ 0.15 galaxies brighter than 1 mJy within $0''.35$ of the stellar position. We therefore conclude that the extragalactic contamination is negligible, but some of the contaminants could still be from close binary companions.

After establishing which ALMA sources are associated with the intended stellar target, there are 38 ALMA continuum sources detected with a signal to noise ratio ≥ 3 that are offset from the target star. For 16 of these ALMA sources, the intended stellar counterpart was also detected such that more than one ALMA source appears in the field. This creates ambiguity in the disk classification, since both sources likely contribute to the infrared emission. Nonetheless, we retain these 16 stars in the sample and keep the disk classification identified in the literature.

For 22 sources, the targeted star is not detected with ALMA but there is another submillimeter continuum source in the field. The infrared excesses for most of these sources were identified from *Spitzer* or *WISE* with an angular resolution of $\sim 6''$. We therefore assume for these targets that when an ALMA source is within $3''$ of the stellar position, the disk classification is compromised and these sources have been removed from the sample.

In summary, 13 sources were removed from the sample since the disk classification of the star may be contaminated by another source in close proximity. This includes 7 sources classified as full disks (2MASS J15442550-2126408, 2MASS J15564244-2039339, 2MASS J15594231-2945495, 2MASS J16044876-1748393, 2MASS J16050647-1734020, 2MASS J16153220-2010236, and 2MASS J16185382-2053182) and 6 sources with evolved disks (2MASS J15524851-2845369,

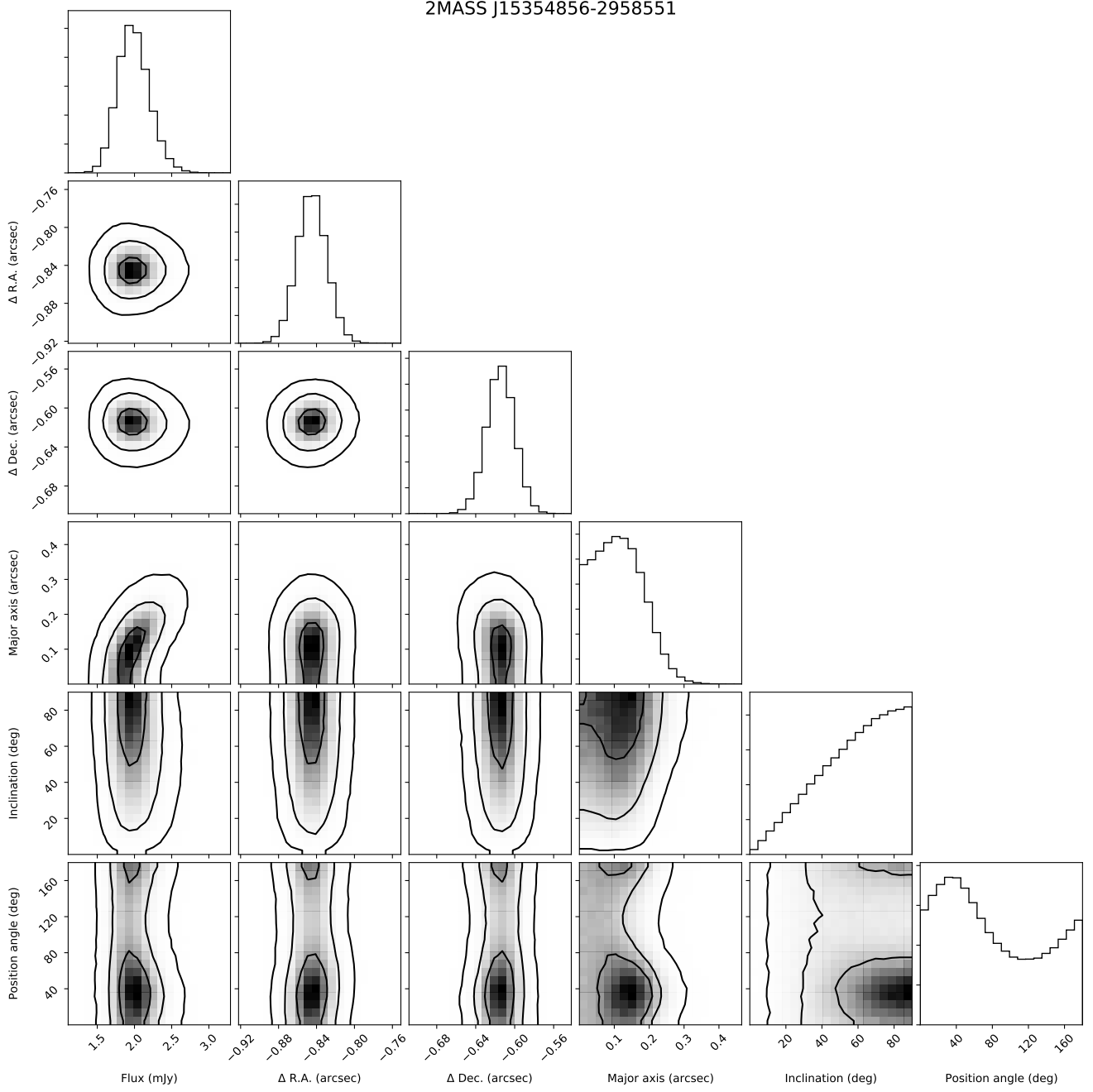


Figure 12. Corner plot for the Gaussian fit to the continuum visibilities of 2MASS J15354856-2958551. The diagonal panels show 1-D histograms for each model parameter, marginalized over the others, with dashed vertical lines indicating the best-fit values. The off-diagonal panels present 2-D projections of the posterior probability distributions for parameter pairs, with contours corresponding to the 1σ , 2σ , and 3σ confidence regions. The full set of figures for the Gaussian fits (121 images) is available in the online journal.

2MASS J15594460-2155250, 2MASS J16052556-2035397, 2MASS J16064385-1908056, 2MASS J16120505-2043404, and 2MASS J16185277-2259537). Table 4 lists the identified counterparts to the additional sources.

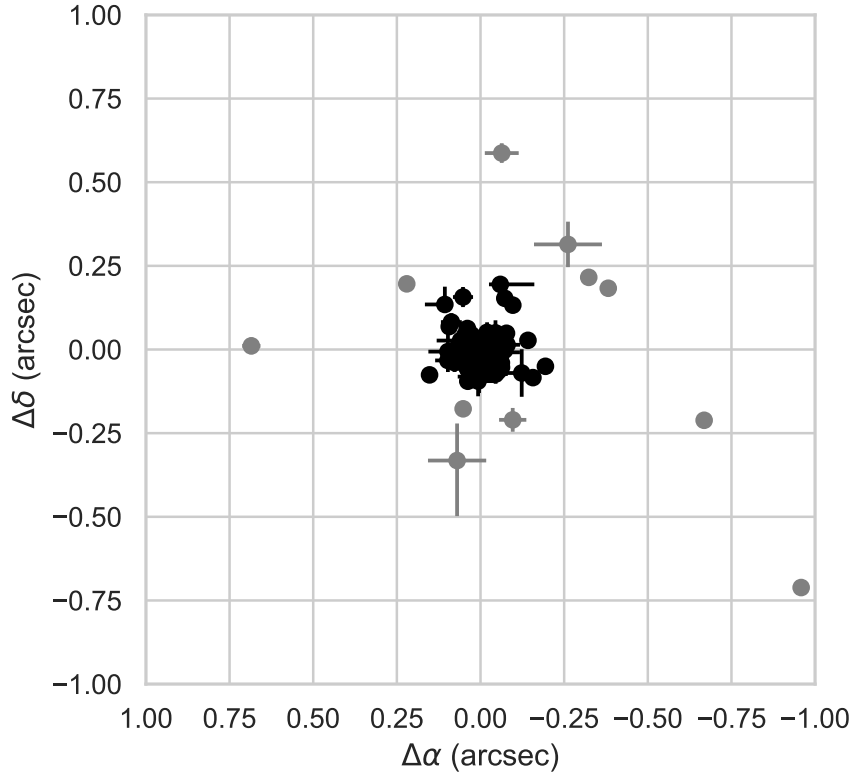


Figure 13. Angular separation between the ALMA continuum detection and the stellar position for ALMA sources detected with a signal to noise ratio of ≥ 3 . Only sources detected with a $1'' \times 1''$ region are shown for clarity. If multiple ALMA sources were detected in the image, then only the ALMA source closest to the star is shown. Black symbols indicate the ALMA continuum sources that are assumed to be associated with the star, and the gray symbols indicate ALMA sources that are not assumed associated with the star.

Table 1. Observed sample

2MASS	Gaia EDR3	SpT ^a	Disk Type ^b	Distance ^c (pc)	Population ^d	Sample? ^e
J15354856-2958551	6209142346187345024	M4	full	94.1 ^{+3.2} _{-2.8}	c	
J15442550-2126408	6241506333509857664	M3.25	full			
J15462696-2443225	6236718475767921664	M4.75	146.2 ^{+1.4} _{-1.2}	c		
J15465432-2556520	6234895897806114560	M5	full	149.0 ^{+1.7} _{-1.6}	uc	Y
J15472572-2609185	6234842567193557888	M4.75	full	146.0 ^{+3.4} _{-3.2}	c	
J15480853-2507011	6236644533607453440	M3	full	141.1 ^{+2.1} _{-1.8}	c	
J15482445-2235495	6240396032927158272	M3.75	full	140.0 ^{+0.7} _{-0.7}	uc	Y
J15485435-2443101	6236682741640391808	M4.75	full	140.9 ^{+1.0} _{-0.8}	uc	Y
J15510126-2523100	6236390271550062464	M4.75	full	157.0 ^{+1.9} _{-1.7}	lc	
J15514032-2146103	6240733445557819264	M4	full	139.7 ^{+1.0} _{-0.6}	uc	Y
J15514709-2113234	6240789280132901632	M4.5	full	142.7 ^{+1.8} _{-1.5}	uc	Y
J15520884-2723456	6233762782358231808	M4	full	173.7 ^{+1.0} _{-0.8}		
J15521088-2125372	6240766048648463488	M4.5	full	154.2 ^{+5.0} _{-6.6}	ulc	Y
J15524851-2845369	6041376800439881472	M4	evolved	142.9 ^{+2.4} _{-2.4}	c	
J15530132-2114135	6246779041523860096	M4	full	141.8 ^{+1.0} _{-1.0}	u	Y
J15534211-2049282	6246807830684399488	M3.4	full	134.8 ^{+2.6} _{-2.7}		
J15540240-2254587	6237326196462378752	M4.5	full	141.9 ^{+0.9} _{-0.8}	u	Y
J15551704-2322165	623725259183461248	M2.5	debris/ev trans?	122.8 ^{+0.6} _{-0.8}	c	
J15554314-2437435	6236547707871265408	M5	full			
J15554883-2512240	6235742349962813824	G3	III	143.0 ^{+0.4} _{-0.4}	c	
J15562477-2225552	6237457553741894016	M4	full	141.1 ^{+0.6} _{-0.7}	u	Y
J15564244-2039339	6246729391702902912	M3.5	full	140.2 ^{+0.7} _{-0.6}	u	
J15565600-2911349	6041077080442819840	M4.75	full	140.2 ^{+1.2} _{-1.5}	c	
J15570146-2046184	6246723275669422464	M4.5	full	141.7 ^{+1.1} _{-0.9}	u	Y
J15570641-2206060	6243485282644929408	M4	full	143.9 ^{+1.0} _{-0.9}	u	Y
J15571045-2545307	6235477127144134144	M4.75	full	145.6 ^{+4.8} _{-4.2}	uc	Y
J15572109-2202130	6243487069351330304	M3.5	full	145.2 ^{+0.4} _{-0.5}	u	Y
J15572986-2258438	6237356707903924608	M4	evolved			
J15573049-1903014	6248218267884353792	M3.25	full	139.8 ^{+1.0} _{-0.7}	u	Y
J15575444-2450424	6236150955972919936	K4	full	134.5 ^{+0.4} _{-0.5}	u	Y
J15581270-2328364	6237136599427052544	G2	debris/ev trans	144.9 ^{+0.4} _{-0.4}	u	Y
J15582981-2310077	6237174395139447808	M4.5	full	140.0 ^{+1.1} _{-0.9}	u	Y
J15583620-1946135	6247358449792211456	M4.25	full	155.6 ^{+0.7} _{-0.7}	ul	Y
J15583692-2257153	6237190612936085120	K0	full	166.5 ^{+0.5} _{-0.4}		
J15584772-1757595	6248435902467580416	K5	debris/ev trans?	137.7 ^{+0.6} _{-0.5}	u	Y
J15590484-2422469	6236191156867993344	M2	full	142.3 ^{+0.4} _{-0.4}	u	Y
J15591452-2606182	6235404525017276544	K2	III	149.3 ^{+2.5} _{-2.7}	u	Y
J15594231-2945495	6040286359786429568	M3.5	full	153.8 ^{+1.3} _{-1.1}		

Table 1 continued on next page

Table 1 (*continued*)

2MASS	Gaia EDR3	SpT ^a	Disk Type ^b	Distance ^c (pc)	Population ^d	Sample? ^e
J15594426-2029232	6246749423430736896	M5	full	138.0 ^{+0.7} _{-0.7}	u	Y
J15594460-2155250	6243457550035199744	M4.75	evolved	106.2 ^{+3.1} _{-4.2}		
J15595116-2311044	6237124539159376640	M2.25	full	139.6 ^{+0.3} _{-0.4}	u	Y
J15595759-1812234	6248378556063992576	M3.25	full	137.1 ^{+0.6} _{-0.6}		
J16001330-2418106	6236195486194570752	M0.5	debris/ev trans?	146.2 ^{+0.6} _{-0.5}	u	Y
J16001730-2236504	6243212844282186880	M4	full	144.0 ^{+0.8} _{-0.7}	u	Y
J16001844-2230114	6243217104889830912	M4.5	full	168.1 ^{+13.2} _{-17.7}		
J16002945-2022536	6247126208021276032	M5	evolved	139.7 ^{+1.1} _{-0.8}	u	Y
J16011398-2516281	6235879479683450496	M4.5	evolved			
J16012268-2408003	6236250942813221120	M2.25	full	140.3 ^{+0.7} _{-0.6}	u	Y
J16012652-2301343	6243135156913242496	M4.5	full	141.9 ^{+0.9} _{-0.9}	u	Y
J16012902-2509069	6235906898751869952	M3.5	full	134.5 ^{+1.1} _{-0.9}	u	Y
J16014086-2258103	6243135809739361792	M4	full	135.0 ^{+1.1} _{-1.4}	u	Y
J16014157-2111380	6243648216526221696	M4	full	140.3 ^{+1.5} _{-1.6}	u	Y
J16020039-2221237	6243235109392659072	M1	debris/ev trans?	141.4 ^{+0.6} _{-0.5}	u	Y
J16020287-2236139	6243221193699945984	M0e	III	307.3 ^{+41.7} _{-68.2}		
J16020429-2231468	6243223873758073728	M3	full	142.9 ^{+1.7} _{-1.8}	u	Y
J16020517-2331070	6236353334834635648	M4.5	full	142.4 ^{+0.7} _{-0.9}	u	Y
J16020757-2257467	6243130106031671168	M2.5	full	139.6 ^{+0.4} _{-0.4}	u	Y
J16023587-2320170	6242360619693213440	M4.25	evolved	139.1 ^{+0.6} _{-0.6}	u	Y
J16024152-2138245	6243553211849342464	M4.75	full	139.4 ^{+1.5} _{-1.2}	u	Y
J16025123-2401574	6236273895118889472	K4	debris/ev trans?	144.5 ^{+0.4} _{-0.4}	u	Y
J16025431-1805300	6249127426563419008	M5	149.3 ^{+1.4} _{-1.4}	u	Y	
J16025855-2256495	6243127838288847232	M2.75	debris/ev trans	147.3 ^{+0.5} _{-0.5}	u	Y
J16030161-2207523	6243332381812183296	M4.75	full	139.1 ^{+1.5} _{-1.3}	u	Y
J16031329-2112569	6243603892463613824	M4.75	full	136.1 ^{+0.8} _{-1.0}	u	Y
J16032225-2413111	6236254859823767936	M3.5	full	139.0 ^{+0.7} _{-0.6}	u	Y
J16032277-2238206	6243176697837023744	M5	full	137.4 ^{+0.8} _{-0.8}	u	Y
J16032625-2155378	624335313050876288	M5	full	141.4 ^{+1.1} _{-1.3}	u	Y
J16035228-2321076	6242351754880605184	M4.5	full	139.6 ^{+2.7} _{-2.4}	u	Y
J16035767-2031055	6244083039015457664	K5	full	142.6 ^{+0.4} _{-0.3}	u	Y
J16035793-1942108	624722213430964608	M2	full	152.9 ^{+0.7} _{-0.7}	ul	Y
J16041416-2129151	6243394091902073728	M4	full	146.5 ^{+1.3} _{-1.2}	u	Y
J16041740-1942287	6247221285718008320	M3.5	full	152.8 ^{+1.0} _{-0.7}	ul	Y
J16041792-1941505	6247227161233273088	M5	full	154.3 ^{+2.5} _{-2.3}	ul	Y
J16041893-2430392	6236047430087176576	M3	full			
J16042165-2130284	6243393817024157184	K2	144.6 ^{+0.7} _{-0.6}	u	Y	
J16043916-1942459	6247224034497055360	M3.25	debris/ev trans	149.6 ^{+0.7} _{-0.7}	u	Y
J16044876-1748393	6249158762644802304	M3.5	full	150.7 ^{+0.6} _{-0.7}	u	
J16050231-1941554	6247224962209972480	M4.5	debris/ev trans	152.6 ^{+1.2} _{-1.4}	ul	Y

Table 1 *continued on next page*

Table 1 (*continued*)

2MASS	Gaia EDR3	SpT ^a	Disk Type ^b	Distance ^c	Population ^d	Sample? ^e
(pc)						
J16050647-1734020	6249260742344680448	M4.75	full	152.3 ^{+1.2} _{-1.4}	u	
J16050844-1947070	6247210428040600960	M4.5	evolved	150.5 ^{+1.4} _{-1.1}	u	Y
J16052076-1821367	6249055271112521216	M2	III	145.2 ^{+0.8} _{-1.0}	u	Y
J16052157-1821412	6249055271112519936	K4.5	148.9 ^{+0.7} _{-0.9}	u	Y	
J16052459-1954419	6247205274079794176	M3.5	debris/ev trans?	151.2 ^{+0.8} _{-0.8}	u	Y
J16052556-2035397	6244020950968009216	M5	evolved	143.5 ^{+2.0} _{-2.2}	u	
J16052661-1957050	6244202748339502848	M4.5	evolved			
J16052730-2614090	6043564828583271680	M4.75	evolved	132.2 ^{+1.8} _{-1.8}	u	Y
J16052787-2115510	6243774351121245184	M4	III	170.1 ^{+2.0} _{-2.2}	u	Y
J16052875-2655496	6042963567523268480	M5	full	154.6 ^{+1.8} _{-1.3}	c	
J16053215-1933159	6247250010459625984	M4.75	evolved	151.3 ^{+1.4} _{-1.0}	ul	Y
J16054540-2023088	6244077816335061504	M4.5	full	137.6 ^{+0.7} _{-0.7}	u	Y
J16055863-1949029	6244205531477555456	M4	full	151.1 ^{+0.9} _{-0.9}	u	Y
J16060061-1957114	6244201992424361216	M4	evolved	155.0 ^{+15.1} _{-14.2}	uo	Y
J16060215-2003142	6244197285140179328	M3.5	full	144.7 ^{+0.6} _{-0.6}	u	Y
J16061144-1935405	6247238293789181440	M5	full	139.6 ^{+1.3} _{-1.3}	u	Y
J16061330-2212537	6243292799392725632	M4	debris/ev trans	139.0 ^{+0.4} _{-0.5}	u	Y
J16062196-1928445	6247245990371393408	M0	transitional			
J16062277-2011243	6244177803168485248	M5	transitional	152.1 ^{+0.9} _{-0.9}	ul	Y
J16062383-1807183	6249088325181290368	M4.25	full	148.6 ^{+0.9} _{-0.7}	u	Y
J16062861-2121297	6243763184206780288	M2	full	139.7 ^{+0.4} _{-0.4}	u	Y
J16063539-2516510	6043774388623996672	M4.5	evolved	137.4 ^{+0.9} _{-1.0}	u	Y
J16064102-2455489	6043818506528512640	M4.5	full	151.8 ^{+1.4} _{-1.5}	uc	Y
J16064115-2517044	6043774285544858880	M3.25	evolved	150.8 ^{+0.6} _{-0.7}	uc	Y
J16064385-1908056	6248768740952946816	K7	evolved	145.3 ^{+3.9} _{-3.3}	u	
J16064794-1841437	6248832413846579840	M0	transitional	155.8 ^{+0.9} _{-0.8}	ul	Y
J16070014-2033092	6244106163113915904	M2.75	full	138.3 ^{+0.5} _{-0.6}	u	Y
J16070211-2019387	6244125335847955968	M5	full	145.6 ^{+2.8} _{-2.5}	u	Y
J16070304-2331460	6242125702157494912	M3.5	full	133.4 ^{+0.6} _{-0.6}	u	Y
J16070873-1927341	6247244203663970944	M4	debris/ev trans	147.7 ^{+1.0} _{-1.0}	u	Y
J16071403-1702425	6249306612595902592	M3.5	full	152.4 ^{+0.7} _{-0.7}	u	Y
J16071971-2020555	6244127741029633024	M3	debris/ev trans?	154.6 ^{+0.8} _{-0.9}	ul	Y
J16072625-2432079	6241990427866622464	M3.5	full	143.4 ^{+0.5} _{-0.5}	u	Y
J16072682-1855239	6248778743935130112	M4.25	III	140.2 ^{+0.8} _{-0.7}	uo	Y
J16072747-2059442	6243810360128177920	M4.75	evolved	179.2 ^{+19.4} _{-21.1}	ul	Y
J16072863-2630130	6043375025387317504	M5	evolved	127.9 ^{+0.8} _{-1.0}	c	
J16072955-2308221	6242417897370352512	M4	full	145.5 ^{+0.8} _{-0.8}	u	Y
J16073939-1917472	6248748266847062912	M2	debris/ev trans?	138.5 ^{+0.6} _{-0.7}	uo	Y
J16075796-2040087	6243914607573143040	K5	full	135.9 ^{+2.0} _{-2.2}	uo	Y
J16080555-2218070	6242532590177846400	M3.25	III	143.5 ^{+0.4} _{-0.4}	u	Y

Table 1 *continued on next page*

Table 1 (*continued*)

2MASS	Gaia EDR3	SpT ^a	Disk Type ^b	Distance ^c (pc)	Population ^d	Sample? ^e
J16081566-2222199	6242527745454719232	M2	full	138.6 ^{+0.4} _{-0.4}	u	Y
J16082324-1930009	6245739521996902272	K9	full	137.0 ^{+0.4} _{-0.4}	u	Y
J16082733-2217292	6242529875758506880	M5	139.9 ^{+0.6} _{-0.6}	u	Y	
J16082751-1949047	6244217076350451968	M5	evolved			
J16082870-2137198	6243694052412741120	M5	full	139.8 ^{+0.8} _{-0.8}	u	Y
J16083319-2015549	6244140243676709376	M4	full/edge-on?	140.9 ^{+3.3} _{-2.5}	uo	Y
J16083455-2211559	6242908790652919040	M4.5	full	137.9 ^{+1.0} _{-1.1}	u	Y
J16084836-2341209	6242059181703801472	M5	full	141.0 ^{+1.4} _{-1.3}	u	Y
J16084894-2400045	6242032896504230400	M3.75	full	143.5 ^{+0.6} _{-0.6}	u	Y
J16090002-1908368	6245777283349431552	M5	full	135.7 ^{+0.8} _{-1.0}	uo	Y
J16090071-2029086	6243923055771917696	M5	full	138.3 ^{+5.1} _{-5.3}	uo	Y
J16090075-1908526	6245777283349430912	M1	full	136.9 ^{+0.5} _{-0.5}	uo	Y
J16090451-2224523	6242480432095204480	M5	III	144.0 ^{+3.0} _{-3.6}	u	Y
J16092136-2139342	6242962945900587392	M5	full	135.7 ^{+2.0} _{-2.3}	u	Y
J16093164-2229224	6242475862249989888	M2.75	full	153.9 ^{+8.3} _{-9.9}		
J16093558-1828232	6248909826335737088	M3	full	157.4 ^{+1.1} _{-1.3}	ul	Y
J16093653-1848009	6248795167890589312	M3	full	135.6 ^{+0.8} _{-0.9}	uo	Y
J16093730-2027250	6243943882070642176	M4.5	105.1 ^{+2.9} _{-2.9}			
J16094098-2217594	6242857942539775232	M0	debris/ev trans	144.8 ^{+0.4} _{-0.4}	u	Y
J16095361-1754474	6249011050125909504	M4.5	full	157.1 ^{+2.7} _{-2.7}	ul	Y
J16095441-1906551	6245775565362814592	M1	debris/ev trans?	137.6 ^{+0.4} _{-0.3}	u	Y
J16095933-1800090	6248997237510309120	M4	full	135.3 ^{+0.8} _{-0.7}	uo	Y
J16101100-1946040	6245669050173377280	M5	debris/ev trans	137.6 ^{+0.8} _{-1.0}	u	Y
J16101264-2104446	6243839046209540864	K3	153.8 ^{+1.0} _{-1.0}	ul	Y	
J16101473-1919095	6245758900889486720	M3	III	137.9 ^{+0.5} _{-0.4}	uo	Y
J16101888-2502325	6049748786908497408	M4.75	full	152.5 ^{+1.8} _{-1.5}	ulc	Y
J16101903-2124251	6242974112815691520	M4.5	full	142.7 ^{+0.9} _{-0.7}	u	Y
J16102174-1904067	6245781097280740864	M1	debris/ev trans?	133.6 ^{+0.4} _{-0.4}	uo	Y
J16102819-1910444	6245768109299634176	M4	full	150.4 ^{+1.5} _{-1.4}	u	Y
J16102857-1904469	6245780856763065984	M3	evolved			
J16103956-1916524	6245757767018447616	M2	debris/ev trans	155.0 ^{+0.5} _{-0.5}	ul	Y
J16104202-2101319	6243833724749589632	K5	debris/ev trans	140.1 ^{+0.4} _{-0.3}	u	Y
J16104391-2032025	6243928317109086464	M4.5	evolved	151.1 ^{+2.6} _{-2.4}	ul	Y
J16104636-1840598	6248888282779703168	M4.5	full	140.1 ^{+1.6} _{-1.3}	uo	Y
J16105011-2157481	6242894054624897152	M4.25	full	139.1 ^{+0.9} _{-0.8}	uo	Y
J16105240-1937344	6245677605748460416	M3	debris/ev trans	138.3 ^{+0.8} _{-0.7}	uo	Y
J16105691-2204515	6242888007310865280	M5	full	142.7 ^{+1.4} _{-1.2}	u	Y
J16111095-1933320	6245701691925397632	M5	evolved	137.5 ^{+1.0} _{-0.9}	uo	Y
J16111237-1927374	6245704749942125952	M5.5	full	137.0 ^{+1.3} _{-1.4}	uo	Y
J16111330-2019029	6243940617895466368	M3	full	152.9 ^{+0.9} _{-0.7}	u	Y

Table 1 *continued on next page*

Table 1 (*continued*)

2MASS	Gaia EDR3	SpT ^a	Disk Type ^b	Distance ^c (pc)	Population ^d	Sample? ^e
J16111534-1757214	6249000566108106112	M1	full	135.3 ^{+0.3} _{-0.3}	uo	Y
J16111705-2213085	6242873473141419648	M5	full	140.8 ^{+0.8} _{-0.9}	u	Y
J16111742-1918285	6245715573259517312	M0.25	136.9 ^{+1.1} _{-1.0}	uo	Y	
J16111907-2319202	6242186072216348544	M5	evolved	140.2 ^{+1.0} _{-1.0}	u	Y
J16112057-1820549	6248926520870519680	K5	debris/ev trans	135.8 ^{+0.4} _{-0.3}	uo	Y
J16112601-2631558	6042662198252863488	M3	evolved			
J16113134-1838259	6245891976154382720	K5	full	131.7 ^{+1.3} _{-1.1}	o	
J16114534-1928132	6245698084152661888	M5	full	138.6 ^{+1.3} _{-1.7}	uo	Y
J16114612-1907429	6245859403122312704	M5	debris/ev trans	135.1 ^{+1.2} _{-1.2}	uo	Y
J16115091-2012098	6245444371843335936	M3.5	full	139.8 ^{+0.6} _{-0.7}	u	Y
J16120239-1926218	6245698393390305664	M4.5	full	139.2 ^{+0.9} _{-0.8}	uo	Y
J16120505-2043404	6243868702963748352	M2.5	evolved	122.5 ^{+7.1} _{-7.3}		
J16120668-3010270	6038520956430662144	M0.5	full	131.9 ^{+0.3} _{-0.3}	u	Y
J16121242-1907191	6245812811317070976	M4.75	full	138.2 ^{+1.4} _{-1.1}	uo	Y
J16122737-2009596	6245447636018595968	M4.5	full	142.2 ^{+1.2} _{-1.5}	uo	Y
J16123352-2543281	6049478414428226688	M4	debris/ev trans	144.9 ^{+0.7} _{-0.6}		
J16123414-2144500	6242993663505753216	M4.75	full	152.6 ^{+1.1} _{-1.1}	u	Y
J16123916-1859284	6245821092014031616	M1.5	full	134.7 ^{+0.3} _{-0.3}	uo	Y
J16124893-1800525	6249313690700531328	M3	evolved?	152.0 ^{+0.6} _{-0.6}	u	Y
J16125533-2319456	6242176653347275136	G2	debris/ev trans	152.5 ^{+0.4} _{-0.4}	ul	Y
J16130627-2606107	6042702605304672896	M3.5	III	154.5 ^{+0.5} _{-0.7}	ulc	Y
J16130982-2302184	6242560490284409856	M5	evolved	126.8 ^{+2.2} _{-2.5}	c	
J16130996-1904269	6245816277354494208	M4	full	135.1 ^{+0.9} _{-0.8}	uo	Y
J16132190-2136136	6243001634964520320	M3.25	full	144.8 ^{+0.5} _{-0.5}	uo	Y
J16133650-2503473	6049575721207795584	M3.5	full			
J16134880-2509006	6049521638979538816	M5	full	160.3 ^{+3.2} _{-3.0}	ul	Y
J16135434-2320342	6050394479417395456	M4.5	full			
J16140792-1938292	6245582772869338368	K1	full	159.5 ^{+0.8} _{-1.0}	ul	Y
J16141107-2305362	6050407948434871808	K4	full			
J16142029-1906481	6245801816200921088	M0	full	138.8 ^{+0.9} _{-1.1}	uo	Y
J16142091-1906051	6245825279605904384	K8	full	135.3 ^{+0.3} _{-0.5}	o	
J16142893-1857224	6245831090698131712	M2.5	debris/ev trans?	135.1 ^{+0.5} _{-0.6}	uo	Y
J16143367-1900133	6245826349054119552	M2	full	135.8 ^{+0.5} _{-0.5}	uo	Y
J16145024-2100599	6244546311362056832	M1.25	full	138.5 ^{+0.6} _{-0.7}	uo	Y
J16145026-2332397	6050377265185700352	M3	full	144.0 ^{+0.6} _{-0.5}	u	Y
J16145131-2308515	6050405234012889856	M5	transitional	164.8 ^{+1.7} _{-1.7}		
J16145244-2513523	6049510643863127680	M3.5	evolved	157.6 ^{+1.7} _{-1.4}	ulc	Y
J16145918-2750230	6042205763488144768	G8	debris/ev trans	149.2 ^{+0.3} _{-0.3}	c	
J16145928-2459308	6049623103285036032	M4.25	full	157.7 ^{+0.8} _{-0.8}	u	Y
J16150095-2733553	6042306403159403776	M5	full	140.8 ^{+1.0} _{-1.0}	uo	Y

Table 1 *continued on next page*

Table 1 (*continued*)

2MASS	Gaia EDR3	SpT ^a	Disk Type ^b	Distance ^c (pc)	Population ^d	Sample? ^e
J16150753-2420204	6049726075120913152	K6	debris/ev trans	156.9 ^{+0.3} _{-0.4}	ul	Y
J16151239-2420091	6049726045061744256	M4	145.2 ^{+1.5} _{-1.2}	uc	Y	
J16152752-1847097	6245840161669008512	M2.25	transitional	137.3 ^{+0.5} _{-0.5}	uo	Y
J16153220-2010236	6245413035762118528	M2.5	full			
J16153341-1854249	6245835179506936704	M5	evolved	154.9 ^{+2.2} _{-2.7}	ul	Y
J16153456-2242421	6242598526515737728	K7	full	138.0 ^{+0.4} _{-0.4}	uo	Y
J16154416-1921171	6245617643707106432	K7	full	125.9 ^{+1.2} _{-1.1}		
J16154533-2110294	6244530059206332160	M4.5	full	136.9 ^{+0.7} _{-0.7}	u	Y
J16154914-2213117	6242721152123092608	M5	transitional	148.6 ^{+1.5} _{-1.5}	u	Y
J16160448-2932400	6038474914382457344	M4.75	full	150.5 ^{+0.8} _{-0.6}		
J16160602-2528217	6048751018766177408	M4.75	evolved	162.7 ^{+2.3} _{-1.9}	uc	Y
J16161423-2643148	6042418858284146688	K5	III	121.1 ^{+0.2} _{-0.2}	c	
J16162531-2412057	6049723468081347072	M5	transitional	154.7 ^{+2.9} _{-2.8}	ulc	Y
J16163345-2521505	6048845748563450368	M0.5	full	158.4 ^{+0.6} _{-0.4}	ul	Y
J16164689-2033323	6244589913870360576	M4	transitional	133.0 ^{+0.7} _{-0.6}	u	Y
J16165083-2009081	6244752126194634240	M4.25	full	126.9 ^{+1.3} _{-1.1}		
J16165556-2014219	6244739791048551680	M5	evolved	136.9 ^{+1.9} _{-1.6}	u	Y
J16171889-2230017	6050548715982482944	M4.75	full			
J16172756-2517222	6048841449299626368	M4.75	full	155.6 ^{+2.8} _{-2.9}	ulc	Y
J16175432-2543435	6048775208020531968	M4.25	evolved	155.6 ^{+1.6} _{-2.0}	u	Y
J16180868-2547126	6048762288758899840	M5	full	147.3 ^{+2.6} _{-3.0}	uc	Y
J16181445-2319251	6050352010777437952	M4.5	full	137.7 ^{+0.7} _{-0.7}	uo	Y
J16181618-2619080	6048459991781686144	M4.5	III			
J16181811-2221150	6050571947461161984	M4.75	full			
J16181904-2028479	6244683166199787392	M4.75	evolved	138.3 ^{+1.3} _{-1.1}	uo	Y
J16182735-2009533	6244744498333170048	M4.75	full	129.7 ^{+0.9} _{-1.0}	u	Y
J16183317-2517504	6048838533018634880	M4.75	evolved	161.4 ^{+5.0} _{-5.5}	uc	Y
J16185228-2516149	6048815168396538368	M5	full	155.2 ^{+2.8} _{-3.0}	ulc	Y
J16185277-2259537	6050459969072881664	M4.5	evolved	136.0 ^{+1.4} _{-1.3}	uo	
J16185382-2053182	6244376608616348928	M0	full	131.0 ^{+3.7} _{-3.8}		
J16191008-2432088	6049274764255776896	M3.5	full	149.9 ^{+0.7} _{-0.8}	uc	Y
J16191936-2329192	6050158050047731072	M3.75	evolved	138.7 ^{+2.9} _{-2.7}	uo	Y
J16192288-2135037	6244258239317113088	M4.75	full	113.0 ^{+4.5} _{-4.9}		
J16193570-1950426	6244778475817598976	M:	full	129.8 ^{+2.8} _{-3.3}	u	Y
J16194711-2203112	6052084050827109504	M5	evolved	126.8 ^{+2.0} _{-2.3}	u	Y
J16194836-2212519	6052068657664195072	M3	debris/ev trans	135.4 ^{+0.5} _{-0.4}	u	Y
J16200357-2419396	6049284110104892288	M4.5	full	158.3 ^{+2.5} _{-2.2}	u	Y
J16200616-2212385	6052065977604571520	M3.5	evolved	137.3 ^{+0.6} _{-0.7}	u	Y
J16201053-2139090	6244276484338020736	M4.5	full	131.7 ^{+0.5} _{-0.6}	c	
J16201949-2337412	6050187393266194816	M4.25	evolved	136.6 ^{+3.4} _{-4.4}	uo	Y

Table 1 *continued on next page*

Table 1 (*continued*)

2MASS	Gaia EDR3	SpT ^a	Disk Type ^b	Distance ^c	Population ^d	Sample? ^e
(pc)						
J16202291-2227041	6050514120021417728	M3.5	evolved	142.0 ^{+0.5} _{-0.5}		
J16202863-2442087	6049256416155461632	M2	full	152.7 ^{+0.6} _{-0.7}	u	Y
J16203960-2634284	6048383747522362496	M3	debris/ev trans	148.3 ^{+0.7} _{-0.7}		
J16204233-2431473	6049266002522895232	M3	evolved	152.3 ^{+1.5} _{-1.4}	u	Y
J16204468-2431384	6049266036882633856	G0	debris/ev trans	166.2 ^{+0.6} _{-0.7}		
J16212930-2537567	6048589321840039808	M4.75	full	161.1 ^{+2.0} _{-2.0}	uc	Y
J16213469-2612269	6048501945023784704	K5	full	150.8 ^{+0.5} _{-0.5}	u	Y
J16215466-2043091	6244440552088537600	K7	III	108.5 ^{+0.2} _{-0.3}		
J16215472-2752053	6045240278140467072	K7	159.3 ^{+0.6} _{-0.5}	u	Y	
J16215741-2238180	6051806217982566272	M4.75	full			
J16220194-2245410	6051801338898199296	M3.75	full	140.1 ^{+1.6} _{-1.4}	uo	Y
J16220961-1953005	6245095242541363072	M3.7	debris/ev trans	133.3 ^{+0.5} _{-0.6}	o	
J16221000-2409118	6049313453321383040	M4.5	III	134.5 ^{+0.8} _{-0.9}	o	
J16221481-2045398	6244436531998870144	M5	evolved	138.0 ^{+4.1} _{-4.3}	u	Y
J16221532-2511349	6048993461079183488	M3	full	139.0 ^{+0.4} _{-0.4}	uo	Y
J16222160-2217307	6052009112237997440	M5	full	134.9 ^{+2.0} _{-2.0}	c	
J16222982-2002472	6244898979715556096	M2.75	full	126.0 ^{+0.4} _{-0.5}		
J16230761-2516339	6048982328524443136	M3.25	full	136.9 ^{+0.6} _{-0.7}	o	
J16230783-2300596	6051735162041951616	K3	debris/ev trans	137.5 ^{+0.4} _{-0.3}	uo	Y
J16231145-2517357	6048982053647568128	M3	full	137.6 ^{+1.3} _{-1.3}	uo	Y
J16235385-2946401	6038066858123563008	G2.5	III	134.6 ^{+0.3} _{-0.4}	c	
J16235468-2515392	6048980163861891840	M4.75	full			
J16251521-2511540	6048957589512689792	M5	evolved			
J16252883-2607538	6045876242538763904	M2.5	debris/ev trans	139.5 ^{+0.3} _{-0.4}	uo	Y
J16253798-1943162	6245016146423892736	M1	150.8 ^{+0.5} _{-0.5}	u	Y	
J16253849-2613540	6045871737110194048	K7	full	137.1 ^{+0.4} _{-0.4}	uo	Y
J16254322-2230026	6051778764550671872	M5	III	128.5 ^{+1.1} _{-1.0}	u	Y
J16261080-2525125	6048936320834323968	M3.5	evolved	147.6 ^{+2.1} _{-2.2}		
J16262925-2507041	6049043832452569728	M5	full	138.0 ^{+1.4} _{-1.2}	u	Y
J16263926-2113453	6052562029145268864	M4.75	full			
J16270942-2148457	6051965303570960768	M4.5	full	137.0 ^{+1.8} _{-1.9}	u	Y
J16271273-2504017	6049045000683707392	M1	full	134.7 ^{+0.3} _{-0.4}	o	
J16274905-2602437	6045854286665108480	M4.75	full	130.9 ^{+0.4} _{-0.4}		
J16284517-2604324	6045840027373568896	M4	evolved	140.6 ^{+0.7} _{-0.7}	uo	Y
J16290902-2515028	6046026394590627840	M4.75	full	134.4 ^{+1.0} _{-0.9}	uo	Y
J16293267-2543291	6045948191826239744	M2.75	full	142.8 ^{+0.6} _{-0.7}	o	
J16294879-2137086	6052302853642527616	M5	full	135.0 ^{+4.2} _{-3.1}	c	
J16294991-2728498	6044389805898446592	K1	debris/ev trans	132.6 ^{+0.3} _{-0.2}		
J16303390-2428062	6050589058606703744	M4	full	145.0 ^{+1.2} _{-1.0}	uo	Y
J16364650-2502032	6047277982427118464	M2.75	full	143.0 ^{+0.4} _{-0.5}	u	Y

Table 1 *continued on next page*

Table 1 (*continued*)

2MASS	Gaia EDR3	SpT ^a	Disk Type ^b	Distance ^c	Population ^d	Sample? ^e
(pc)						
J16365288-2708187	6044636130868878208	G0	III	160.1 ^{+0.6} _{-0.4}	u	Y
J16370169-2545368	6046467333112041728	M4.75	evolved			
J16371121-2725003	6044608570048364928	M5	evolved	145.4 ^{+3.0} _{-2.7}	uc	Y
J16394272-2812141	6032502642101481600	M4.5	full			
J16395577-2347355	6047871787419721344	M2	full	150.6 ^{+0.7} _{-0.6}		
J16413713-2730489	6032565142467104512	M4.75	full			

^aSpectral types are from Luhman (2022b) and references therein, and from Manara et al. (2020).

^bDisk types are from Luhman (2020) and Luhman (2022b).

^cDistances are from the Gaia EDR3 distance catalog by Bailer-Jones et al. (2021).

^dPopulation subgroup membership in the Scorpius-Centaurus Association from Luhman & Esplin (2020) and Luhman (2022b).

^eSources marked with 'Y' are include in the final sample of Upper Sco sources.

Table 2. Cycle 6 Observations

UT date	Number	Baseline range	PWV	Calibrators					
				Antennas	(m)	(mm)	Flux	Passband	Gain
2018 Nov 13	43	15-1397	0.45	J1427-4206	J1427-4206	J1553-2422			
2018 Nov 15	42	15-1397	0.69	J1427-4206	J1427-4206	J1553-2422			
2018 Nov 25	44	15-1397	0.84	J1427-4206	J1427-4206	J1553-2422			
2018 Dec 5	44	15-783	0.37	J1517-2422	J1517-2422	J1553-2422			
2019 Apr 19	49	15-740	0.64	J1517-2422	J1517-2422	J1551-1755			
2019 Apr 19	48	15-740	0.60	J1517-2422	J1517-2422	J1626-2951			
2019 Apr 19	48	15-740	0.57	J1517-2422	J1517-2422	J1626-2951			
2019 Apr 20	46	15-740	0.43	J1517-2422	J1517-2422	J1553-2422			
2019 Apr 21	46	15-740	0.74	J1517-2422	J1517-2422	J1553-2422			
2019 Apr 21	47	15-740	0.82	J1517-2422	J1517-2422	J1553-2422			
2019 Sep 28	50	15-2617	0.82	J1517-2422	J1517-2422	J1650-2943			

Table 3. Band 7 continuum flux measurements for the full sample

2MASS	Flux (mJy)	$\Delta\alpha$ (arcsec)	$\Delta\delta$ (arcsec)	Major axis (arcsec)	Inclination (deg)	PA (deg)
J15354856-2958551	2.01 ^{+0.21} _{-0.21}	-0.07 ^{+0.02} _{-0.02}	-0.00 ^{+0.02} _{-0.01}	0.10 ^{+0.07} _{-0.07}	83.5 ^{+5.5} _{-35.7}	35.5 ^{+41.1} _{-60.5}
J15442550-2126408	-0.23 ^{+0.15} _{-0.45}
J15462696-2443225	-0.10 ^{+0.12} _{-0.12}
J15465432-2556520	4.71 ^{+0.35} _{-0.35}	0.07 ^{+0.02} _{-0.02}	-0.01 ^{+0.02} _{-0.02}	0.41 ^{+0.05} _{-0.05}	47.0 ^{+9.4} _{-13.6}	126.6 ^{+21.2} _{-17.9}
J15472572-2609185	0.23 ^{+0.11} _{-0.11}
J15480853-2507011	1.76 ^{+0.38} _{-0.38}	0.01 ^{+0.06} _{-0.06}	-0.08 ^{+0.05} _{-0.05}	0.51 ^{+0.15} _{-0.11}	71.4 ^{+13.4} _{-22.1}	46.5 ^{+28.8} _{-13.5}
J15482445-2235495	1.93 ^{+0.13} _{-0.13}	-0.02 ^{+0.01} _{-0.01}	0.01 ^{+0.01} _{-0.01}	0.22 ^{+0.04} _{-0.04}	86.0 ^{+3.8} _{-17.7}	167.3 ^{+16.1} _{-9.1}
J15485435-2443101	2.18 ^{+0.54} _{-0.54}	-0.10 ^{+0.10} _{-0.09}	-0.06 ^{+0.06} _{-0.08}	0.83 ^{+0.28} _{-0.21}	60.3 ^{+11.9} _{-23.7}	107.1 ^{+20.4} _{-44.6}
J15510126-2523100	1.86 ^{+0.27} _{-0.27}	0.02 ^{+0.03} _{-0.02}	0.00 ^{+0.03} _{-0.03}	0.32 ^{+0.05} _{-0.06}	42.5 ^{+13.8} _{-20.3}	6.5 ^{+61.1} _{-38.7}
J15514032-2146103	0.65 ^{+0.17} _{-0.17}
J15514709-2113234	0.96 ^{+0.22} _{-0.22}	-0.03 ^{+0.08} _{-0.08}	-0.01 ^{+0.06} _{-0.06}	0.60 ^{+0.26} _{-0.18}	81.5 ^{+7.8} _{-29.5}	52.3 ^{+38.1} _{-11.0}
J15520884-2723456	0.09 ^{+0.11} _{-0.11}
J15521088-2125372	0.09 ^{+0.16} _{-0.16}
J15524851-2845369	-0.00 ^{+0.12} _{-0.12}
J15530132-2114135	5.85 ^{+0.19} _{-0.19}	-0.05 ^{+0.01} _{-0.01}	-0.00 ^{+0.01} _{-0.01}	0.05 ^{+0.04} _{-0.04}	82.6 ^{+6.0} _{-37.6}	201.6 ^{+33.6} _{-80.5}
J15534211-2049282	3.11 ^{+0.28} _{-0.28}	-0.19 ^{+0.02} _{-0.03}	-0.05 ^{+0.01} _{-0.01}	0.47 ^{+0.07} _{-0.06}	86.3 ^{+3.1} _{-9.4}	75.9 ^{+5.5} _{-5.9}
J15540240-2254587	0.53 ^{+0.10} _{-0.10}	-0.05 ^{+0.03} _{-0.03}	-0.06 ^{+0.03} _{-0.03}
J15551704-2322165	0.30 ^{+0.16} _{-0.16}
J15554314-2437435	-0.10 ^{+0.11} _{-0.11}
J15554883-2512240	0.11 ^{+0.15} _{-0.15}
J15562477-2225552	0.32 ^{+0.19} _{-0.19}
J15564244-2039339	0.03 ^{+0.09} _{-0.09}
J15565600-2911349	0.13 ^{+0.11} _{-0.11}
J15570146-2046184	2.39 ^{+0.14} _{-0.14}	-0.01 ^{+0.01} _{-0.01}	-0.01 ^{+0.01} _{-0.01}	0.21 ^{+0.03} _{-0.02}	46.4 ^{+15.5} _{-18.8}	8.9 ^{+25.9} _{-25.5}
J15570641-2206060	0.23 ^{+0.20} _{-0.20}
J15571045-2545307	-0.05 ^{+0.11} _{-0.11}
J15572109-2202130	1.77 ^{+0.15} _{-0.15}	-0.05 ^{+0.02} _{-0.01}	0.01 ^{+0.01} _{-0.01}	0.22 ^{+0.05} _{-0.04}	55.4 ^{+18.5} _{-22.1}	154.0 ^{+18.6} _{-34.5}
J15572986-2258438	-0.05 ^{+0.21} _{-0.21}
J15573049-1903014	1.51 ^{+0.11} _{-0.11}	-0.01 ^{+0.01} _{-0.01}	-0.05 ^{+0.01} _{-0.01}	0.10 ^{+0.06} _{-0.05}	83.3 ^{+5.7} _{-34.0}	43.3 ^{+37.4} _{-44.4}
J15575444-2450424	7.33 ^{+0.48} _{-0.48}	-0.02 ^{+0.01} _{-0.01}	-0.00 ^{+0.01} _{-0.01}
J15581270-2328364	0.02 ^{+0.15} _{-0.15}
J15582981-2310077	5.93 ^{+0.21} _{-0.21}	0.07 ^{+0.01} _{-0.01}	0.01 ^{+0.01} _{-0.01}	0.03 ^{+0.07} _{-0.03}	80.5 ^{+8.3} _{-32.7}	53.2 ^{+44.8} _{-71.0}
J15583620-1946135	0.55 ^{+0.13} _{-0.13}	-0.00 ^{+0.05} _{-0.05}	-0.05 ^{+0.03} _{-0.03}	0.08 ^{+0.20} _{-0.08}	83.7 ^{+5.7} _{-32.7}	105.4 ^{+68.1} _{-35.2}
J15583692-2257153	175.50 ^{+0.60} _{-0.60}	-0.01 ^{+0.01} _{-0.01}	-0.04 ^{+0.01} _{-0.01}
J15584772-1757595	-0.07 ^{+0.15} _{-0.15}
J15590484-2422469	2.53 ^{+0.28} _{-0.28}	-0.10 ^{+0.02} _{-0.01}	0.13 ^{+0.02} _{-0.02}	0.35 ^{+0.09} _{-0.07}	72.4 ^{+10.6} _{-17.3}	164.3 ^{+10.4} _{-10.1}
J15591452-2606182	-0.15 ^{+0.12} _{-0.12}
J15594231-2945495	0.07 ^{+0.15} _{-0.15}

Table 3 continued on next page

Table 3 (*continued*)

2MASS	Flux	$\Delta\alpha$	$\Delta\delta$	Major axis	Inclination	PA
	(mJy)	(arcsec)	(arcsec)	(arcsec)	(deg)	(deg)
J15594426-2029232	0.78 $^{+0.11}_{-0.11}$	0.01 $^{+0.02}_{-0.02}$	-0.07 $^{+0.02}_{-0.02}$	0.04 $^{+0.10}_{-0.04}$	83.9 $^{+5.4}_{-34.5}$	124.1 $^{+52.9}_{-58.6}$
J15594460-2155250	0.07 $^{+0.09}_{-0.09}$
J15595116-2311044	6.39 $^{+0.15}_{-0.15}$	0.01 $^{+0.01}_{-0.01}$	0.00 $^{+0.01}_{-0.01}$	0.24 $^{+0.01}_{-0.02}$	38.5 $^{+6.3}_{-8.9}$	94.0 $^{+13.5}_{-12.4}$
J15595759-1812234	1.28 $^{+0.12}_{-0.12}$	0.07 $^{+0.02}_{-0.02}$	-0.00 $^{+0.01}_{-0.01}$	0.15 $^{+0.07}_{-0.07}$	83.3 $^{+6.4}_{-29.2}$	94.1 $^{+37.9}_{-24.1}$
J16001330-2418106	-0.08 $^{+0.16}_{-0.16}$
J16001730-2236504	0.13 $^{+0.16}_{-0.16}$
J16001844-2230114	4.16 $^{+0.25}_{-0.25}$	-0.05 $^{+0.01}_{-0.01}$	-0.01 $^{+0.01}_{-0.01}$	0.15 $^{+0.03}_{-0.04}$	54.1 $^{+31.4}_{-13.8}$	11.0 $^{+29.9}_{-35.3}$
J16002945-2022536	0.04 $^{+0.09}_{-0.09}$
J16011398-2516281	0.31 $^{+0.12}_{-0.12}$
J16012268-2408003	9.38 $^{+0.31}_{-0.31}$	0.05 $^{+0.01}_{-0.01}$	-0.05 $^{+0.01}_{-0.01}$	0.33 $^{+0.02}_{-0.02}$	29.2 $^{+7.7}_{-11.1}$	59.9 $^{+21.4}_{-25.0}$
J16012652-2301343	0.10 $^{+0.09}_{-0.09}$
J16012902-2509069	0.36 $^{+0.11}_{-0.11}$
J16014086-2258103	3.95 $^{+0.26}_{-0.26}$	-0.06 $^{+0.01}_{-0.01}$	0.00 $^{+0.01}_{-0.01}$	0.19 $^{+0.04}_{-0.04}$	73.4 $^{+15.1}_{-20.4}$	24.3 $^{+20.0}_{-16.9}$
J16014157-2111380	0.62 $^{+0.15}_{-0.15}$
J16020039-2221237	-0.03 $^{+0.15}_{-0.15}$
J16020287-2236139	-0.11 $^{+0.16}_{-0.16}$
J16020429-2231468	0.91 $^{+0.15}_{-0.15}$	-0.03 $^{+0.03}_{-0.03}$	-0.06 $^{+0.02}_{-0.03}$	0.22 $^{+0.10}_{-0.09}$	62.0 $^{+21.3}_{-23.3}$	99.2 $^{+49.8}_{-51.8}$
J16020517-2331070	0.13 $^{+0.09}_{-0.09}$
J16020757-2257467	5.13 $^{+0.28}_{-0.28}$	-0.02 $^{+0.01}_{-0.01}$	-0.01 $^{+0.01}_{-0.01}$	0.25 $^{+0.03}_{-0.03}$	56.2 $^{+11.3}_{-12.1}$	81.8 $^{+12.5}_{-10.9}$
J16023587-2320170	0.12 $^{+0.09}_{-0.09}$
J16024152-2138245	10.68 $^{+0.24}_{-0.24}$	0.03 $^{+0.01}_{-0.01}$	-0.05 $^{+0.01}_{-0.01}$	0.11 $^{+0.03}_{-0.03}$	39.0 $^{+17.0}_{-16.2}$	153.6 $^{+27.6}_{-38.4}$
J16025123-2401574	0.09 $^{+0.15}_{-0.15}$
J16025431-1805300	2.97 $^{+0.15}_{-0.15}$	-0.01 $^{+0.01}_{-0.01}$	-0.01 $^{+0.01}_{-0.01}$	0.26 $^{+0.03}_{-0.03}$	64.6 $^{+10.2}_{-11.8}$	109.6 $^{+10.3}_{-7.8}$
J16025855-2256495	0.02 $^{+0.08}_{-0.08}$
J16030161-2207523	3.05 $^{+0.19}_{-0.19}$	0.03 $^{+0.01}_{-0.01}$	-0.03 $^{+0.01}_{-0.01}$	0.11 $^{+0.05}_{-0.05}$	71.1 $^{+16.7}_{-26.2}$	58.8 $^{+56.6}_{-34.9}$
J16031329-2112569	0.05 $^{+0.13}_{-0.13}$
J16032225-2413111	2.52 $^{+0.20}_{-0.20}$	-0.04 $^{+0.01}_{-0.01}$	-0.00 $^{+0.01}_{-0.01}$	0.09 $^{+0.05}_{-0.08}$	83.6 $^{+5.4}_{-34.7}$	71.1 $^{+56.6}_{-41.0}$
J16032277-2238206	0.49 $^{+0.09}_{-0.09}$	-0.09 $^{+0.04}_{-0.04}$	0.01 $^{+0.03}_{-0.04}$
J16032625-2155378	0.40 $^{+0.09}_{-0.09}$	-0.04 $^{+0.04}_{-0.04}$	-0.08 $^{+0.03}_{-0.03}$
J16035228-2321076	1.35 $^{+0.13}_{-0.13}$	-0.00 $^{+0.02}_{-0.01}$	-0.03 $^{+0.01}_{-0.01}$	0.15 $^{+0.05}_{-0.05}$	56.5 $^{+23.5}_{-21.5}$	94.5 $^{+49.9}_{-50.9}$
J16035767-2031055	5.83 $^{+0.86}_{-0.86}$	0.07 $^{+0.02}_{-0.02}$	-0.00 $^{+0.04}_{-0.04}$	0.54 $^{+0.16}_{-0.16}$	74.6 $^{+13.7}_{-12.1}$	6.4 $^{+13.8}_{-11.7}$
J16035793-1942108	2.99 $^{+0.69}_{-0.69}$	-0.01 $^{+0.04}_{-0.04}$	-0.03 $^{+0.04}_{-0.05}$	0.63 $^{+0.21}_{-0.15}$	53.3 $^{+14.0}_{-19.7}$	25.4 $^{+25.0}_{-33.3}$
J16041416-2129151	5.94 $^{+0.14}_{-0.14}$	-0.01 $^{+0.01}_{-0.01}$	-0.01 $^{+0.01}_{-0.01}$	0.16 $^{+0.01}_{-0.01}$	30.1 $^{+9.5}_{-14.2}$	23.2 $^{+37.6}_{-36.6}$
J16041740-1942287	0.84 $^{+0.16}_{-0.16}$	0.04 $^{+0.03}_{-0.03}$	0.02 $^{+0.03}_{-0.02}$	0.02 $^{+0.10}_{-0.02}$	83.8 $^{+5.3}_{-34.7}$	93.6 $^{+56.9}_{-61.5}$
J16041792-1941505	0.21 $^{+0.09}_{-0.09}$
J16041893-2430392	6.50 $^{+0.30}_{-0.30}$	0.01 $^{+0.01}_{-0.01}$	0.02 $^{+0.01}_{-0.01}$	0.40 $^{+0.03}_{-0.03}$	63.6 $^{+4.0}_{-4.7}$	67.2 $^{+3.7}_{-4.2}$
J16042165-2130284	217.40 $^{+0.73}_{-0.73}$	-0.02 $^{+0.01}_{-0.01}$	0.05 $^{+0.01}_{-0.01}$
J16043916-1942459	0.36 $^{+0.15}_{-0.15}$
J16044876-1748393	0.11 $^{+0.09}_{-0.09}$
J16050231-1941554	-0.34 $^{+0.15}_{-0.15}$

Table 3 continued on next page

Table 3 (*continued*)

2MASS	Flux	$\Delta\alpha$	$\Delta\delta$	Major axis	Inclination	PA
	(mJy)	(arcsec)	(arcsec)	(arcsec)	(deg)	(deg)
J16050647-1734020	-0.03 ^{+0.09} _{-0.09}
J16050844-1947070	0.54 ^{+0.09} _{-0.09}	-0.00 ^{+0.04} _{-0.04}	-0.05 ^{+0.04} _{-0.03}
J16052076-1821367	-0.15 ^{+0.13} _{-0.13}
J16052157-1821412	45.43 ^{+0.31} _{-0.31}	0.02 ^{+0.01} _{-0.01}	-0.01 ^{+0.01} _{-0.01}	0.49 ^{+0.01} _{-0.01}	62.2 ^{+1.1} _{-1.1}	155.1 ^{+24.9} _{-0.6}
J16052459-1954419	-0.15 ^{+0.15} _{-0.15}
J16052556-2035397	0.06 ^{+0.18} _{-0.18}
J16052661-1957050	-0.02 ^{+0.15} _{-0.15}
J16052730-2614090	0.01 ^{+0.12} _{-0.12}
J16052787-2115510	0.06 ^{+0.09} _{-0.09}
J16052875-2655496	0.55 ^{+0.12} _{-0.12}	-0.05 ^{+0.05} _{-0.05}	0.19 ^{+0.03} _{-0.04}
J16053215-1933159	0.24 ^{+0.20} _{-0.20}
J16054540-2023088	11.01 ^{+0.26} _{-0.26}	-0.03 ^{+0.01} _{-0.01}	-0.01 ^{+0.01} _{-0.01}	0.07 ^{+0.04} _{-0.04}	46.0 ^{+29.0} _{-19.4}	30.8 ^{+25.5} _{-78.2}
J16055863-1949029	-0.08 ^{+0.16} _{-0.16}
J16060061-1957114	0.09 ^{+0.14} _{-0.14}
J16060215-2003142	0.32 ^{+0.09} _{-0.09}
J16061144-1935405	1.56 ^{+0.14} _{-0.14}	0.02 ^{+0.01} _{-0.01}	0.01 ^{+0.01} _{-0.01}	0.22 ^{+0.07} _{-0.05}	86.2 ^{+3.8} _{-14.8}	22.4 ^{+10.4} _{-13.8}
J16061330-2212537	-0.28 ^{+0.13} _{-0.13}
J16062196-1928445	4.87 ^{+0.78} _{-0.78}	-0.04 ^{+0.04} _{-0.04}	0.05 ^{+0.04} _{-0.03}	0.34 ^{+0.14} _{-0.13}	83.5 ^{+6.2} _{-30.4}	123.0 ^{+22.7} _{-39.5}
J16062277-2011243	0.55 ^{+0.13} _{-0.13}
J16062383-1807183	5.23 ^{+0.15} _{-0.15}	-0.04 ^{+0.01} _{-0.01}	-0.03 ^{+0.01} _{-0.01}	0.19 ^{+0.02} _{-0.01}	34.1 ^{+9.2} _{-14.0}	90.0 ^{+27.9} _{-27.2}
J16062861-2121297	12.42 ^{+0.17} _{-0.17}	-0.03 ^{+0.01} _{-0.01}	-0.04 ^{+0.01} _{-0.01}	0.23 ^{+0.01} _{-0.01}	28.6 ^{+5.9} _{-8.1}	105.3 ^{+13.7} _{-16.3}
J16063539-2516510	2.06 ^{+0.27} _{-0.27}	-0.01 ^{+0.02} _{-0.01}	-0.01 ^{+0.02} _{-0.02}	0.23 ^{+0.07} _{-0.09}	83.5 ^{+5.9} _{-28.8}	17.3 ^{+33.3} _{-21.2}
J16064102-2455489	3.50 ^{+0.25} _{-0.25}	-0.06 ^{+0.01} _{-0.01}	0.02 ^{+0.01} _{-0.01}	0.17 ^{+0.04} _{-0.04}	48.6 ^{+20.7} _{-21.9}	87.5 ^{+40.1} _{-37.4}
J16064115-2517044	-0.00 ^{+0.15} _{-0.15}
J16064385-1908056	0.21 ^{+0.18} _{-0.18}
J16064794-1841437	119.05 ^{+1.07} _{-1.07}	-0.01 ^{+0.01} _{-0.01}	-0.04 ^{+0.01} _{-0.01}
J16070014-2033092	0.34 ^{+0.16} _{-0.16}
J16070211-2019387	0.37 ^{+0.21} _{-0.21}
J16070304-2331460	8.98 ^{+0.14} _{-0.14}	0.03 ^{+0.01} _{-0.01}	-0.04 ^{+0.01} _{-0.01}	0.20 ^{+0.01} _{-0.01}	53.2 ^{+6.4} _{-5.4}	17.8 ^{+6.5} _{-4.9}
J16070873-1927341	0.20 ^{+0.17} _{-0.17}
J16071403-1702425	0.02 ^{+0.09} _{-0.09}
J16071971-2020555	0.20 ^{+0.16} _{-0.16}
J16072625-2432079	13.70 ^{+0.31} _{-0.31}	-0.07 ^{+0.01} _{-0.01}	0.02 ^{+0.01} _{-0.01}	0.14 ^{+0.01} _{-0.02}	50.0 ^{+13.0} _{-18.0}	150.4 ^{+14.5} _{-19.4}
J16072682-1855239	0.09 ^{+0.10} _{-0.10}
J16072747-2059442	2.19 ^{+0.15} _{-0.15}	0.05 ^{+0.01} _{-0.01}	-0.01 ^{+0.01} _{-0.01}	0.02 ^{+0.07} _{-0.01}	83.9 ^{+5.3} _{-35.0}	29.0 ^{+50.4} _{-58.3}
J16072863-2630130	0.18 ^{+0.11} _{-0.11}
J16072955-2308221	7.15 ^{+0.13} _{-0.13}	-0.02 ^{+0.01} _{-0.01}	0.02 ^{+0.01} _{-0.01}	0.12 ^{+0.01} _{-0.01}	30.1 ^{+13.1} _{-14.1}	30.8 ^{+52.1} _{-40.6}
J16073939-1917472	0.01 ^{+0.16} _{-0.16}
J16075796-2040087	23.90 ^{+0.20} _{-0.20}	0.04 ^{+0.01} _{-0.01}	-0.01 ^{+0.01} _{-0.01}	0.08 ^{+0.01} _{-0.01}	65.8 ^{+14.8} _{-10.3}	1.4 ^{+7.7} _{-0.9}
J16080555-2218070	0.12 ^{+0.13} _{-0.13}

Table 3 *continued on next page*

Table 3 (*continued*)

2MASS	Flux	$\Delta\alpha$	$\Delta\delta$	Major axis	Inclination	PA
	(mJy)	(arcsec)	(arcsec)	(arcsec)	(deg)	(deg)
J16081566-2222199	1.58 $^{+0.27}_{-0.27}$	0.06 $^{+0.02}_{-0.02}$	-0.02 $^{+0.04}_{-0.04}$	0.44 $^{+0.13}_{-0.12}$	87.1 $^{+2.9}_{-9.8}$	171.5 $^{+12.5}_{-7.4}$
J16082324-1930009	43.64 $^{+0.80}_{-0.80}$	-0.14 $^{+0.01}_{-0.01}$	0.03 $^{+0.01}_{-0.01}$	0.40 $^{+0.01}_{-0.01}$	71.4 $^{+5.3}_{-5.0}$	124.1 $^{+2.2}_{-2.7}$
J16082733-2217292	0.60 $^{+0.09}_{-0.09}$	-0.04 $^{+0.02}_{-0.03}$	-0.00 $^{+0.02}_{-0.02}$	0.02 $^{+0.09}_{-0.02}$	84.0 $^{+5.4}_{-33.8}$	63.0 $^{+34.5}_{-76.3}$
J16082751-1949047	0.75 $^{+0.15}_{-0.15}$	0.01 $^{+0.05}_{-0.06}$	-0.09 $^{+0.04}_{-0.05}$
J16082870-2137198	0.69 $^{+0.22}_{-0.22}$	-0.06 $^{+0.07}_{-0.05}$	-0.08 $^{+0.06}_{-0.07}$	0.38 $^{+0.24}_{-0.15}$	56.8 $^{+21.6}_{-22.4}$	172.5 $^{+58.0}_{-47.8}$
J16083319-2015549	1.30 $^{+0.14}_{-0.14}$	0.01 $^{+0.02}_{-0.02}$	-0.02 $^{+0.02}_{-0.02}$	0.25 $^{+0.08}_{-0.06}$	67.8 $^{+18.8}_{-20.1}$	62.5 $^{+24.5}_{-16.6}$
J16083455-2211559	0.15 $^{+0.13}_{-0.13}$
J16084836-2341209	1.99 $^{+0.11}_{-0.11}$	0.00 $^{+0.01}_{-0.01}$	-0.01 $^{+0.01}_{-0.01}$	0.10 $^{+0.04}_{-0.06}$	75.6 $^{+12.9}_{-28.7}$	161.7 $^{+58.0}_{-37.9}$
J16084894-2400045	-0.10 $^{+0.15}_{-0.15}$
J16090002-1908368	1.81 $^{+0.16}_{-0.16}$	0.04 $^{+0.03}_{-0.02}$	0.06 $^{+0.02}_{-0.01}$	0.03 $^{+0.13}_{-0.02}$	82.5 $^{+6.5}_{-33.6}$	104.7 $^{+59.0}_{-50.0}$
J16090071-2029086	1.07 $^{+0.12}_{-0.12}$	-0.01 $^{+0.02}_{-0.02}$	0.00 $^{+0.02}_{-0.01}$	0.14 $^{+0.06}_{-0.06}$	66.9 $^{+20.2}_{-23.6}$	76.3 $^{+38.1}_{-67.9}$
J16090075-1908526	47.21 $^{+1.00}_{-1.00}$	0.04 $^{+0.01}_{-0.01}$	-0.09 $^{+0.01}_{-0.01}$	0.31 $^{+0.02}_{-0.02}$	54.3 $^{+5.4}_{-5.5}$	153.8 $^{+6.9}_{-5.9}$
J16090451-2224523	0.05 $^{+0.08}_{-0.08}$
J16092136-2139342	0.88 $^{+0.19}_{-0.06}$	-0.06 $^{+0.02}_{-0.02}$	-0.02 $^{+0.01}_{-0.01}$	0.04 $^{+0.17}_{-0.04}$	85.2 $^{+4.8}_{-26.6}$	104.5 $^{+32.1}_{-41.3}$
J16093164-2229224	10.73 $^{+0.13}_{-0.13}$	0.02 $^{+0.01}_{-0.01}$	0.00 $^{+0.01}_{-0.01}$	0.14 $^{+0.01}_{-0.01}$	57.8 $^{+9.7}_{-8.2}$	31.4 $^{+7.4}_{-5.9}$
J16093558-1828232	0.56 $^{+0.16}_{-0.16}$
J16093653-1848009	1.27 $^{+0.18}_{-0.18}$	0.02 $^{+0.02}_{-0.02}$	0.01 $^{+0.02}_{-0.03}$	0.27 $^{+0.09}_{-0.09}$	64.8 $^{+17.3}_{-25.9}$	164.0 $^{+37.1}_{-30.0}$
J16093730-2027250	0.17 $^{+0.09}_{-0.09}$
J16094098-2217594	0.33 $^{+0.13}_{-0.13}$
J16095361-1754474	0.98 $^{+0.21}_{-0.21}$	-0.00 $^{+0.03}_{-0.03}$	-0.01 $^{+0.04}_{-0.04}$	0.05 $^{+0.19}_{-0.04}$	83.7 $^{+5.8}_{-32.7}$	147.3 $^{+45.0}_{-54.5}$
J16095441-1906551	0.01 $^{+0.16}_{-0.16}$
J16095933-1800090	0.51 $^{+0.18}_{-0.18}$
J16101100-1946040	-0.04 $^{+0.08}_{-0.08}$
J16101264-2104446	73.40 $^{+0.77}_{-0.77}$	0.02 $^{+0.01}_{-0.01}$	0.01 $^{+0.01}_{-0.01}$
J16101473-1919095	0.07 $^{+0.16}_{-0.16}$
J16101888-2502325	0.28 $^{+0.14}_{-0.14}$
J16101903-2124251	0.69 $^{+0.10}_{-0.10}$	0.06 $^{+0.02}_{-0.02}$	-0.02 $^{+0.02}_{-0.02}$	0.11 $^{+0.07}_{-0.08}$	80.7 $^{+7.9}_{-33.7}$	80.3 $^{+35.0}_{-76.4}$
J16102174-1904067	0.05 $^{+0.16}_{-0.16}$
J16102819-1910444	0.11 $^{+0.16}_{-0.16}$
J16102857-1904469	0.16 $^{+0.16}_{-0.16}$
J16103956-1916524	0.06 $^{+0.16}_{-0.16}$
J16104202-2101319	0.26 $^{+0.13}_{-0.13}$
J16104391-2032025	0.08 $^{+0.09}_{-0.09}$
J16104636-1840598	1.95 $^{+0.20}_{-0.20}$	-0.03 $^{+0.02}_{-0.01}$	-0.02 $^{+0.01}_{-0.01}$	0.06 $^{+0.07}_{-0.05}$	83.2 $^{+5.7}_{-36.5}$	108.1 $^{+45.3}_{-69.5}$
J16105011-2157481	2.45 $^{+0.09}_{-0.09}$	0.03 $^{+0.01}_{-0.01}$	0.01 $^{+0.01}_{-0.01}$	0.03 $^{+0.05}_{-0.03}$	84.1 $^{+5.2}_{-34.8}$	80.5 $^{+34.6}_{-69.8}$
J16105240-1937344	0.17 $^{+0.09}_{-0.09}$
J16105691-2204515	1.06 $^{+0.09}_{-0.09}$	-0.02 $^{+0.02}_{-0.02}$	-0.02 $^{+0.01}_{-0.01}$	0.02 $^{+0.08}_{-0.01}$	83.0 $^{+6.0}_{-34.4}$	105.1 $^{+44.4}_{-72.3}$
J16111095-1933320	-0.14 $^{+0.09}_{-0.09}$
J16111237-1927374	3.47 $^{+0.14}_{-0.14}$	-0.00 $^{+0.01}_{-0.01}$	0.00 $^{+0.01}_{-0.01}$	0.16 $^{+0.03}_{-0.02}$	53.3 $^{+14.0}_{-19.1}$	121.8 $^{+18.4}_{-21.1}$
J16111330-2019029	7.27 $^{+0.22}_{-0.22}$	-0.04 $^{+0.01}_{-0.01}$	-0.03 $^{+0.01}_{-0.01}$	0.05 $^{+0.03}_{-0.04}$	83.4 $^{+5.5}_{-35.0}$	85.4 $^{+49.5}_{-49.6}$

Table 3 continued on next page

Table 3 (*continued*)

2MASS	Flux	$\Delta\alpha$	$\Delta\delta$	Major axis	Inclination	PA
	(mJy)	(arcsec)	(arcsec)	(arcsec)	(deg)	(deg)
J16111534-1757214	0.14 ^{+0.17} _{-0.17}
J16111705-2213085	5.21 ^{+0.10} _{-0.10}	0.01 ^{+0.01} _{-0.01}	-0.02 ^{+0.01} _{-0.01}	0.03 ^{+0.05} _{-0.02}	84.4 ^{+5.6} _{-26.7}	140.1 ^{+37.8} _{-30.2}
J16111742-1918285	0.40 ^{+0.09} _{-0.09}
J16111907-2319202	-0.10 ^{+0.08} _{-0.08}
J16112057-1820549	-0.08 ^{+0.16} _{-0.16}
J16112601-2631558	0.21 ^{+0.11} _{-0.11}
J16113134-1838259	902.70 ^{+4.47} _{-4.47}	0.02 ^{+0.01} _{-0.01}	-0.05 ^{+0.01} _{-0.01}	0.44 ^{+0.01} _{-0.01}	23.9 ^{+1.1} _{-1.3}	113.4 ^{+3.1} _{-3.2}
J16114534-1928132	1.32 ^{+0.14} _{-0.14}	-0.00 ^{+0.02} _{-0.02}	-0.02 ^{+0.01} _{-0.02}	0.18 ^{+0.06} _{-0.06}	61.2 ^{+23.5} _{-20.8}	145.1 ^{+28.7} _{-51.5}
J16114612-1907429	0.11 ^{+0.08} _{-0.08}
J16115091-2012098	0.65 ^{+0.16} _{-0.16}
J16120239-1926218	4.09 ^{+0.15} _{-0.15}	-0.03 ^{+0.01} _{-0.01}	0.03 ^{+0.01} _{-0.01}	0.28 ^{+0.02} _{-0.02}	71.2 ^{+7.2} _{-8.4}	164.2 ^{+5.9} _{-4.4}
J16120505-2043404	0.13 ^{+0.09} _{-0.09}
J16120668-3010270	57.43 ^{+1.22} _{-1.22}	0.05 ^{+0.01} _{-0.01}	0.16 ^{+0.01} _{-0.01}
J16121242-1907191	0.49 ^{+0.08} _{-0.08}	0.07 ^{+0.04} _{-0.03}	-0.04 ^{+0.03} _{-0.03}
J16122737-2009596	0.50 ^{+0.16} _{-0.16}
J16123352-2543281	0.02 ^{+0.12} _{-0.12}
J16123414-2144500	0.33 ^{+0.09} _{-0.09}
J16123916-1859284	9.45 ^{+0.34} _{-0.34}	-0.05 ^{+0.01} _{-0.01}	-0.01 ^{+0.01} _{-0.01}	0.20 ^{+0.02} _{-0.02}	36.7 ^{+10.3} _{-14.9}	109.0 ^{+26.3} _{-30.4}
J16124893-1800525	0.37 ^{+0.16} _{-0.16}
J16125533-2319456	0.01 ^{+0.13} _{-0.13}
J16130627-2606107	-0.14 ^{+0.11} _{-0.11}
J16130982-2302184	0.14 ^{+0.08} _{-0.08}
J16130996-1904269	0.33 ^{+0.17} _{-0.17}
J16132190-2136136	16.79 ^{+0.16} _{-0.16}	0.01 ^{+0.01} _{-0.01}	0.01 ^{+0.01} _{-0.01}	0.14 ^{+0.01} _{-0.01}	30.3 ^{+6.6} _{-11.7}	178.3 ^{+19.7} _{-22.0}
J16133650-2503473	0.67 ^{+0.20} _{-0.20}
J16134880-2509006	1.65 ^{+0.09} _{-0.09}	0.00 ^{+0.01} _{-0.01}	-0.00 ^{+0.01} _{-0.01}	0.09 ^{+0.04} _{-0.03}	73.5 ^{+14.9} _{-23.8}	85.7 ^{+18.6} _{-45.5}
J16135434-2320342	8.21 ^{+0.20} _{-0.20}	0.01 ^{+0.01} _{-0.01}	0.00 ^{+0.01} _{-0.01}	0.08 ^{+0.02} _{-0.03}	51.0 ^{+27.8} _{-19.0}	48.4 ^{+39.4} _{-54.2}
J16140792-1938292	57.50 ^{+0.73} _{-0.73}	0.02 ^{+0.01} _{-0.01}	-0.02 ^{+0.01} _{-0.01}
J16141107-2305362	5.05 ^{+0.20} _{-0.20}	0.15 ^{+0.01} _{-0.01}	-0.08 ^{+0.01} _{-0.01}	0.16 ^{+0.04} _{-0.05}	52.4 ^{+29.7} _{-17.3}	43.2 ^{+39.8} _{-55.0}
J16142029-1906481	41.45 ^{+0.26} _{-0.26}	-0.08 ^{+0.01} _{-0.01}	0.05 ^{+0.01} _{-0.01}	0.18 ^{+0.01} _{-0.01}	28.7 ^{+8.1} _{-11.1}	19.8 ^{+21.9} _{-17.2}
J16142091-1906051	1.87 ^{+0.18} _{-0.18}	0.03 ^{+0.02} _{-0.02}	0.04 ^{+0.02} _{-0.02}	0.39 ^{+0.09} _{-0.06}	53.4 ^{+12.5} _{-22.9}	147.3 ^{+15.1} _{-38.9}
J16142893-1857224	0.08 ^{+0.16} _{-0.16}
J16143367-1900133	1.33 ^{+0.19} _{-0.19}	-0.06 ^{+0.02} _{-0.02}	-0.06 ^{+0.02} _{-0.02}	0.02 ^{+0.11} _{-0.02}	82.8 ^{+6.4} _{-32.8}	47.3 ^{+61.1} _{-47.1}
J16145024-2100599	33.04 ^{+0.24} _{-0.24}	0.02 ^{+0.01} _{-0.01}	0.01 ^{+0.01} _{-0.01}	0.36 ^{+0.01} _{-0.01}	33.1 ^{+2.2} _{-2.1}	180.7 ^{+0.1} _{-13.3}
J16145026-2332397	1.35 ^{+0.12} _{-0.12}	0.03 ^{+0.01} _{-0.01}	0.01 ^{+0.01} _{-0.01}	0.17 ^{+0.07} _{-0.07}	83.9 ^{+4.9} _{-36.5}	39.7 ^{+45.2} _{-34.0}
J16145131-2308515	0.28 ^{+0.09} _{-0.09}
J16145244-2513523	-0.04 ^{+0.07} _{-0.07}
J16145918-2750230	0.08 ^{+0.19} _{-0.19}
J16145928-2459308	0.04 ^{+0.13} _{-0.13}
J16150095-2733553	0.24 ^{+0.11} _{-0.11}

Table 3 *continued on next page*

Table 3 (*continued*)

2MASS	Flux	$\Delta\alpha$	$\Delta\delta$	Major axis	Inclination	PA
	(mJy)	(arcsec)	(arcsec)	(arcsec)	(deg)	(deg)
J16150753-2420204	0.05 ^{+0.08} _{-0.08}
J16151239-2420091	0.08 ^{+0.14} _{-0.14}
J16152752-1847097	74.66 ^{+0.56} _{-0.56}	0.03 ^{+0.01} _{-0.01}	0.04 ^{+0.01} _{-0.01}	0.76 ^{+0.01} _{-0.01}	74.3 ^{+0.4} _{-0.4}	161.8 ^{+0.5} _{-0.3}
J16153220-2010236	0.02 ^{+0.10} _{-0.10}
J16153341-1854249	0.15 ^{+0.09} _{-0.09}
J16153456-2242421	12.84 ^{+0.31} _{-0.31}	0.02 ^{+0.01} _{-0.01}	0.00 ^{+0.01} _{-0.01}	0.12 ^{+0.05} _{-0.05}	49.4 ^{+16.2} _{-19.2}	161.7 ^{+17.4} _{-24.2}
J16154416-1921171	23.88 ^{+0.25} _{-0.25}	-0.06 ^{+0.01} _{-0.01}	-0.04 ^{+0.01} _{-0.01}	0.07 ^{+0.01} _{-0.01}	50.7 ^{+18.6} _{-23.8}	101.1 ^{+31.3} _{-30.2}
J16154533-2110294	0.44 ^{+0.08} _{-0.08}	0.10 ^{+0.04} _{-0.03}	-0.03 ^{+0.03} _{-0.04}
J16154914-2213117	0.27 ^{+0.09} _{-0.09}
J16160448-2932400	-0.08 ^{+0.11} _{-0.11}
J16160602-2528217	-0.04 ^{+0.07} _{-0.07}
J16161423-2643148	-0.12 ^{+0.12} _{-0.12}
J16162531-2412057	1.42 ^{+0.11} _{-0.11}	0.01 ^{+0.01} _{-0.01}	-0.02 ^{+0.01} _{-0.01}	0.12 ^{+0.04} _{-0.08}	81.8 ^{+7.2} _{-34.2}	29.9 ^{+67.8} _{-32.4}
J16163345-2521505	2.76 ^{+0.31} _{-0.31}	0.05 ^{+0.02} _{-0.03}	0.04 ^{+0.02} _{-0.02}	0.48 ^{+0.08} _{-0.06}	64.4 ^{+9.0} _{-9.3}	64.6 ^{+8.4} _{-10.2}
J16164689-2033323	0.40 ^{+0.08} _{-0.08}
J16165083-2009081	26.13 ^{+0.20} _{-0.20}	-0.02 ^{+0.01} _{-0.01}	-0.01 ^{+0.01} _{-0.01}	0.14 ^{+0.01} _{-0.01}	22.3 ^{+6.1} _{-10.5}	100.9 ^{+27.0} _{-36.3}
J16165556-2014219	0.19 ^{+0.08} _{-0.08}
J16171889-2230017	2.49 ^{+0.10} _{-0.10}	0.08 ^{+0.01} _{-0.01}	-0.03 ^{+0.01} _{-0.01}	0.05 ^{+0.04} _{-0.04}	83.2 ^{+5.6} _{-35.4}	104.8 ^{+44.7} _{-61.1}
J16172756-2517222	0.21 ^{+0.07} _{-0.07}
J16175432-2543435	0.23 ^{+0.07} _{-0.07}
J16180868-2547126	0.33 ^{+0.07} _{-0.07}	0.09 ^{+0.06} _{-0.05}	-0.00 ^{+0.06} _{-0.03}
J16181445-2319251	4.06 ^{+0.13} _{-0.13}	0.01 ^{+0.01} _{-0.01}	0.01 ^{+0.01} _{-0.01}	0.16 ^{+0.02} _{-0.03}	46.3 ^{+15.5} _{-18.1}	104.3 ^{+20.6} _{-26.7}
J16181618-2619080	0.07 ^{+0.14} _{-0.14}
J16181811-2221150	0.16 ^{+0.08} _{-0.08}
J16181904-2028479	4.81 ^{+0.17} _{-0.17}	0.01 ^{+0.01} _{-0.01}	-0.01 ^{+0.01} _{-0.01}	0.06 ^{+0.02} _{-0.05}	83.8 ^{+4.9} _{-37.3}	90.0 ^{+44.0} _{-60.6}
J16182735-2009533	1.43 ^{+0.13} _{-0.13}	0.04 ^{+0.02} _{-0.02}	-0.01 ^{+0.01} _{-0.01}	0.18 ^{+0.07} _{-0.07}	58.9 ^{+27.0} _{-17.4}	61.0 ^{+66.4} _{-24.3}
J16183317-2517504	1.39 ^{+0.08} _{-0.08}	-0.01 ^{+0.01} _{-0.01}	-0.01 ^{+0.01} _{-0.01}	0.08 ^{+0.04} _{-0.03}	85.1 ^{+4.9} _{-19.9}	56.5 ^{+17.5} _{-24.4}
J16185228-2516149	0.18 ^{+0.07} _{-0.07}
J16185277-2259537	-0.02 ^{+0.09} _{-0.09}
J16185382-2053182	0.22 ^{+0.09} _{-0.09}
J16191008-2432088	3.56 ^{+0.10} _{-0.10}	0.01 ^{+0.01} _{-0.01}	0.01 ^{+0.01} _{-0.01}	0.16 ^{+0.02} _{-0.02}	49.2 ^{+9.7} _{-11.5}	54.2 ^{+12.0} _{-20.7}
J16191936-2329192	0.15 ^{+0.08} _{-0.08}
J16192288-2135037	1.23 ^{+0.13} _{-0.13}	0.04 ^{+0.02} _{-0.02}	-0.06 ^{+0.02} _{-0.02}	0.26 ^{+0.09} _{-0.11}	85.9 ^{+4.1} _{-14.5}	132.4 ^{+16.6} _{-13.2}
J16193570-1950426	56.12 ^{+0.46} _{-0.46}	0.01 ^{+0.01} _{-0.01}	-0.04 ^{+0.01} _{-0.01}	0.35 ^{+0.01} _{-0.01}	66.5 ^{+1.1} _{-1.2}	120.9 ^{+1.0} _{-1.0}
J16194711-2203112	0.27 ^{+0.08} _{-0.08}
J16194836-2212519	0.00 ^{+0.08} _{-0.08}
J16200357-2419396	0.28 ^{+0.07} _{-0.07}
J16200616-2212385	0.09 ^{+0.08} _{-0.08}
J16201053-2139090	1.04 ^{+0.11} _{-0.11}	0.03 ^{+0.02} _{-0.02}	-0.00 ^{+0.02} _{-0.02}	0.18 ^{+0.07} _{-0.09}	74.2 ^{+14.1} _{-28.7}	153.1 ^{+50.1} _{-40.9}
J16201949-2337412	0.77 ^{+0.10} _{-0.10}	-0.07 ^{+0.02} _{-0.02}	0.15 ^{+0.02} _{-0.02}	0.06 ^{+0.09} _{-0.05}	84.3 ^{+5.1} _{-33.6}	9.1 ^{+54.3} _{-45.6}

Table 3 continued on next page

Table 3 (*continued*)

2MASS	Flux	$\Delta\alpha$	$\Delta\delta$	Major axis	Inclination	PA
	(mJy)	(arcsec)	(arcsec)	(arcsec)	(deg)	(deg)
J16202291-2227041	1.22 ^{+0.16} _{-0.16}	0.02 ^{+0.04} _{-0.04}	-0.02 ^{+0.02} _{-0.02}	0.41 ^{+0.14} _{-0.09}	68.6 ^{+12.2} _{-17.1}	80.2 ^{+20.1} _{-13.8}
J16202863-2442087	5.89 ^{+0.18} _{-0.18}	0.06 ^{+0.01} _{-0.01}	0.01 ^{+0.01} _{-0.01}	0.52 ^{+0.02} _{-0.03}	44.4 ^{+4.6} _{-4.8}	179.1 ^{+0.7} _{-3.8}
J16203960-2634284	84.87 ^{+0.62} _{-0.62}	-0.01 ^{+0.01} _{-0.01}	0.03 ^{+0.01} _{-0.01}
J16204233-2431473	-0.04 ^{+0.07} _{-0.07}
J16204468-2431384	0.05 ^{+0.07} _{-0.07}
J16212930-2537567	0.05 ^{+0.07} _{-0.07}
J16213469-2612269	129.39 ^{+0.43} _{-0.43}	0.03 ^{+0.01} _{-0.01}	0.01 ^{+0.01} _{-0.01}	0.41 ^{+0.01} _{-0.01}	49.3 ^{+0.5} _{-0.5}	45.0 ^{+0.6} _{-0.6}
J16215466-2043091	-0.00 ^{+0.14} _{-0.14}
J16215472-2752053	28.99 ^{+0.17} _{-0.17}	0.01 ^{+0.01} _{-0.01}	0.01 ^{+0.01} _{-0.01}	0.30 ^{+0.01} _{-0.03}	63.3 ^{+1.6} _{-15.1}	27.1 ^{+0.5} _{-27.1}
J16215741-2238180	4.03 ^{+0.14} _{-0.14}	-0.00 ^{+0.01} _{-0.01}	-0.02 ^{+0.01} _{-0.01}	0.10 ^{+0.03} _{-0.03}	55.0 ^{+22.2} _{-24.2}	97.4 ^{+39.5} _{-55.2}
J16220194-2245410	0.27 ^{+0.08} _{-0.08}
J16220961-1953005	-0.01 ^{+0.17} _{-0.17}
J16221000-2409118	0.00 ^{+0.07} _{-0.07}
J16221481-2045398	0.07 ^{+0.08} _{-0.08}
J16221532-2511349	31.60 ^{+0.16} _{-0.16}	-0.01 ^{+0.01} _{-0.01}	-0.00 ^{+0.01} _{-0.01}	0.29 ^{+0.01} _{-0.01}	53.6 ^{+1.0} _{-1.0}	18.1 ^{+1.1} _{-1.1}
J16222160-2217307	1.77 ^{+0.10} _{-0.10}	0.02 ^{+0.01} _{-0.01}	0.03 ^{+0.01} _{-0.01}	0.08 ^{+0.02} _{-0.07}	83.6 ^{+5.2} _{-35.7}	101.3 ^{+62.1} _{-44.4}
J16222982-2002472	34.15 ^{+0.29} _{-0.29}	0.02 ^{+0.01} _{-0.01}	-0.00 ^{+0.01} _{-0.01}	0.16 ^{+0.01} _{-0.01}	34.6 ^{+5.0} _{-5.8}	167.5 ^{+7.0} _{-11.3}
J16230761-2516339	0.64 ^{+0.16} _{-0.16}	0.05 ^{+0.07} _{-0.07}	0.04 ^{+0.05} _{-0.06}	0.40 ^{+0.26} _{-0.17}	71.6 ^{+17.0} _{-25.1}	49.5 ^{+51.2} _{-44.6}
J16230783-2300596	-0.04 ^{+0.13} _{-0.13}
J16231145-2517357	14.77 ^{+0.11} _{-0.11}	-0.00 ^{+0.01} _{-0.01}	-0.01 ^{+0.01} _{-0.01}	0.15 ^{+0.01} _{-0.01}	38.5 ^{+4.0} _{-3.6}	126.3 ^{+6.9} _{-5.5}
J16235385-2946401	-0.04 ^{+0.13} _{-0.13}
J16235468-2515392	3.40 ^{+0.11} _{-0.11}	0.06 ^{+0.01} _{-0.01}	-0.02 ^{+0.01} _{-0.01}	0.32 ^{+0.02} _{-0.02}	77.1 ^{+4.0} _{-4.1}	116.3 ^{+3.1} _{-3.2}
J16251521-2511540	2.35 ^{+0.08} _{-0.08}	-0.06 ^{+0.01} _{-0.01}	-0.03 ^{+0.01} _{-0.01}	0.05 ^{+0.03} _{-0.02}	74.8 ^{+14.2} _{-23.8}	106.5 ^{+44.4} _{-30.4}
J16252883-2607538	0.14 ^{+0.07} _{-0.07}
J16253798-1943162	34.00 ^{+0.36} _{-0.36}	0.00 ^{+0.01} _{-0.01}	-0.02 ^{+0.01} _{-0.01}	0.53 ^{+0.01} _{-0.01}	75.5 ^{+0.9} _{-1.1}	71.3 ^{+0.8} _{-0.8}
J16253849-2613540	7.62 ^{+0.10} _{-0.10}	-0.01 ^{+0.01} _{-0.01}	0.00 ^{+0.01} _{-0.01}	0.13 ^{+0.01} _{-0.01}	42.6 ^{+7.8} _{-8.5}	171.8 ^{+10.7} _{-11.3}
J16254322-2230026	0.21 ^{+0.08} _{-0.08}
J16261080-2525125	0.02 ^{+0.07} _{-0.07}
J16262925-2507041	0.37 ^{+0.07} _{-0.07}	0.05 ^{+0.03} _{-0.05}	0.02 ^{+0.02} _{-0.03}
J16263926-2113453	0.62 ^{+0.10} _{-0.10}	0.08 ^{+0.03} _{-0.03}	0.09 ^{+0.02} _{-0.03}	0.04 ^{+0.11} _{-0.04}	82.8 ^{+6.4} _{-33.4}	115.5 ^{+81.7} _{-34.0}
J16270942-2148457	3.21 ^{+0.20} _{-0.20}	-0.01 ^{+0.01} _{-0.01}	-0.01 ^{+0.01} _{-0.01}	0.16 ^{+0.04} _{-0.05}	83.9 ^{+5.8} _{-23.3}	171.1 ^{+19.4} _{-20.4}
J16271273-2504017	1.30 ^{+0.09} _{-0.09}	0.03 ^{+0.02} _{-0.01}	0.01 ^{+0.01} _{-0.01}	0.13 ^{+0.04} _{-0.03}	45.3 ^{+21.7} _{-18.7}	91.8 ^{+42.4} _{-66.4}
J16274905-2602437	29.22 ^{+0.14} _{-0.14}	0.02 ^{+0.01} _{-0.01}	-0.00 ^{+0.01} _{-0.01}	0.21 ^{+0.01} _{-0.01}	45.8 ^{+1.5} _{-1.3}	45.3 ^{+2.0} _{-1.8}
J16284517-2604324	0.11 ^{+0.07} _{-0.07}
J16290902-2515028	1.87 ^{+0.08} _{-0.08}	-0.00 ^{+0.01} _{-0.01}	-0.01 ^{+0.01} _{-0.01}	0.08 ^{+0.03} _{-0.02}	84.8 ^{+5.2} _{-23.1}	34.2 ^{+20.9} _{-27.3}
J16293267-2543291	28.77 ^{+0.15} _{-0.15}	0.00 ^{+0.01} _{-0.01}	0.01 ^{+0.01} _{-0.01}	0.17 ^{+0.01} _{-0.01}	27.3 ^{+3.0} _{-3.3}	81.8 ^{+7.3} _{-7.6}
J16294879-2137086	0.22 ^{+0.08} _{-0.08}
J16294991-2728498	0.04 ^{+0.07} _{-0.07}
J16303390-2428062	0.56 ^{+0.14} _{-0.14}
J16364650-2502032	1.74 ^{+0.09} _{-0.09}	-0.01 ^{+0.01} _{-0.01}	0.00 ^{+0.01} _{-0.01}	0.21 ^{+0.03} _{-0.03}	79.2 ^{+9.6} _{-10.1}	109.3 ^{+8.8} _{-8.2}

Table 3 continued on next page

Table 3 (*continued*)

2MASS	Flux	$\Delta\alpha$	$\Delta\delta$	Major axis	Inclination	PA
	(mJy)	(arcsec)	(arcsec)	(arcsec)	(deg)	(deg)
J16365288-2708187	-0.02 ^{+0.07} _{-0.07}
J16370169-2545368	0.41 ^{+0.07} _{-0.07}	0.10 ^{+0.04} _{-0.03}	0.13 ^{+0.06} _{-0.02}
J16371121-2725003	2.15 ^{+0.09} _{-0.09}	0.03 ^{+0.01} _{-0.01}	-0.00 ^{+0.01} _{-0.01}	0.11 ^{+0.02} _{-0.02}	40.2 ^{+16.8} _{-17.7}	67.2 ^{+35.7} _{-48.4}
J16394272-2812141	2.55 ^{+0.08} _{-0.08}	-0.16 ^{+0.01} _{-0.01}	-0.08 ^{+0.01} _{-0.01}	0.07 ^{+0.02} _{-0.02}	56.5 ^{+14.5} _{-25.0}	98.8 ^{+38.2} _{-49.7}
J16395577-2347355	9.72 ^{+0.10} _{-0.10}	0.01 ^{+0.01} _{-0.01}	0.00 ^{+0.01} _{-0.01}	0.14 ^{+0.01} _{-0.01}	47.6 ^{+3.9} _{-4.7}	80.6 ^{+5.7} _{-6.2}
J16413713-2730489	0.84 ^{+0.10} _{-0.10}	0.09 ^{+0.02} _{-0.02}	0.07 ^{+0.02} _{-0.02}	0.13 ^{+0.07} _{-0.05}	78.6 ^{+9.6} _{-33.3}	23.4 ^{+55.4} _{-34.1}

Table 4. Band 7 continuum flux measurements for additional sources

Field	Flux (mJy)	$\Delta\alpha$ (arcsec)	$\Delta\delta$ (arcsec)	Major axis (arcsec)	Inclination (deg)	PA (deg)	Notes
J15442550-2126408	2.92 ^{+0.50} _{-0.17}	0.05 ^{+0.01} _{-0.01}	-0.18 ^{+0.02} _{-0.01}	0.19 ^{+0.04} _{-0.04}	57.4 ^{+12.4} _{-19.3}	175.2 ^{+29.9} _{-12.1}	
J15480853-2507011	1.55 ^{+0.41} _{-0.41}	-0.03 ^{+0.06} _{-0.06}	-1.03 ^{+0.08} _{-0.08}	0.51 ^{+0.24} _{-0.16}	67.5 ^{+14.0} _{-23.2}	154.4 ^{+32.5} _{-28.8}	Gaia EDR3
J15510126-2523100	2.41 ^{+0.24} _{-0.24}	-0.28 ^{+0.01} _{-0.01}	-2.00 ^{+0.02} _{-0.02}	0.35 ^{+0.06} _{-0.05}	83.6 ^{+5.9} _{-6.0}	1.2 ^{+2.1} _{-15.4}	Gaia EDR3
J15524851-2845369	1.53 ^{+0.46} _{-0.46}	-0.24 ^{+0.09} _{-0.11}	0.32 ^{+0.06} _{-0.07}	0.61 ^{+0.39} _{-0.24}	61.4 ^{+18.8} _{-23.1}	80.1 ^{+52.3} _{-30.1}	
J15564244-2039339	4.24 ^{+0.13} _{-0.13}	0.86 ^{+0.01} _{-0.01}	1.05 ^{+0.01} _{-0.01}	0.15 ^{+0.02} _{-0.01}	30.7 ^{+13.9} _{-12.8}	59.2 ^{+55.7} _{-29.9}	Gaia EDR3
J15584772-1757595	1.73 ^{+0.29} _{-0.29}	-3.04 ^{+0.03} _{-0.03}	0.90 ^{+0.03} _{-0.02}	0.24 ^{+0.08} _{-0.09}	55.3 ^{+23.4} _{-22.3}	102.9 ^{+70.3} _{-35.3}	
J15594231-2945495	2.03 ^{+0.60} _{-0.60}	0.07 ^{+0.09} _{-0.09}	-0.34 ^{+0.12} _{-0.16}	0.98 ^{+0.34} _{-0.27}	66.1 ^{+14.2} _{-24.7}	168.7 ^{+12.2} _{-42.8}	
J15594460-2155250	0.60 ^{+0.11} _{-0.11}	0.68 ^{+0.03} _{-0.03}	0.02 ^{+0.02} _{-0.03}	0.04 ^{+0.14} _{-0.04}	83.6 ^{+5.5} _{-34.9}	122.8 ^{+31.7} _{-86.5}	
J16012902-2509069	1.57 ^{+0.33} _{-0.33}	0.10 ^{+0.05} _{-0.03}	0.57 ^{+0.04} _{-0.04}	0.39 ^{+0.12} _{-0.11}	62.2 ^{+17.0} _{-27.1}	136.8 ^{+41.3} _{-45.8}	Gaia EDR3
J16020287-2236139	3.84 ^{+0.45} _{-0.45}	4.46 ^{+0.03} _{-0.02}	2.83 ^{+0.01} _{-0.02}	0.42 ^{+0.08} _{-0.07}	62.4 ^{+10.0} _{-13.0}	98.2 ^{+10.3} _{-12.6}	
J16025123-2401574	2.09 ^{+0.55} _{-0.18}	3.96 ^{+0.02} _{-0.02}	3.79 ^{+0.02} _{-0.02}	0.24 ^{+0.09} _{-0.10}	62.0 ^{+20.3} _{-24.5}	72.2 ^{+55.2} _{-35.5}	
J16032225-2413111	3.48 ^{+0.60} _{-0.60}	-6.73 ^{+0.03} _{-0.03}	-0.20 ^{+0.02} _{-0.03}	0.38 ^{+0.09} _{-0.09}	50.7 ^{+15.6} _{-23.1}	106.7 ^{+45.2} _{-25.8}	
J16044876-1748393	2.59 ^{+0.15} _{-0.15}	-1.83 ^{+0.01} _{-0.01}	2.18 ^{+0.01} _{-0.01}	0.21 ^{+0.03} _{-0.03}	57.5 ^{+18.8} _{-22.5}	175.3 ^{+18.6} _{-20.8}	Gaia EDR3
J16050647-1734020	1.98 ^{+0.13} _{-0.13}	-0.96 ^{+0.01} _{-0.01}	-0.71 ^{+0.01} _{-0.01}	0.17 ^{+0.05} _{-0.05}	84.9 ^{+4.9} _{-21.3}	24.3 ^{+16.6} _{-19.5}	
J16052556-2035397	1.61 ^{+0.22} _{-0.22}	-0.06 ^{+0.05} _{-0.05}	0.59 ^{+0.03} _{-0.03}	0.05 ^{+0.22} _{-0.04}	82.2 ^{+6.9} _{-32.9}	94.5 ^{+52.2} _{-60.5}	Barenfeld et al. (2019)
J16052730-2614090	4.43 ^{+0.66} _{-0.66}	2.63 ^{+0.04} _{-0.04}	-4.04 ^{+0.03} _{-0.03}	0.56 ^{+0.15} _{-0.09}	47.5 ^{+9.6} _{-22.0}	78.8 ^{+41.1} _{-31.8}	
J16064385-1908056	0.73 ^{+0.17} _{-0.17}	-0.09 ^{+0.04} _{-0.04}	-0.21 ^{+0.04} _{-0.03}	WDS 16067-1908 AB
J16092136-2139342	2.86 ^{+0.14} _{-0.14}	-0.12 ^{+0.01} _{-0.01}	-0.69 ^{+0.01} _{-0.01}	0.19 ^{+0.03} _{-0.02}	46.3 ^{+10.2} _{-22.0}	29.2 ^{+26.4} _{-39.5}	Gaia EDR3
J16104391-2032025	1.66 ^{+0.32} _{-0.32}	-5.79 ^{+0.06} _{-0.07}	-3.84 ^{+0.04} _{-0.04}	0.51 ^{+0.16} _{-0.14}	61.1 ^{+14.8} _{-25.3}	97.0 ^{+16.3} _{-45.7}	
J16111095-1933320	1.49 ^{+0.23} _{-0.23}	-0.40 ^{+0.03} _{-0.03}	-3.51 ^{+0.03} _{-0.03}	0.35 ^{+0.11} _{-0.09}	47.8 ^{+19.8} _{-21.7}	17.7 ^{+74.1} _{-19.7}	
J16111742-1918285	1.52 ^{+0.25} _{-0.25}	0.31 ^{+0.04} _{-0.04}	2.71 ^{+0.04} _{-0.04}	0.47 ^{+0.15} _{-0.11}	47.6 ^{+14.3} _{-21.9}	53.3 ^{+78.4} _{-21.8}	
J16112601-2631558	5.56 ^{+0.79} _{-0.79}	-4.79 ^{+0.05} _{-0.05}	-4.12 ^{+0.03} _{-0.04}	0.65 ^{+0.20} _{-0.11}	50.5 ^{+10.4} _{-19.9}	81.1 ^{+23.4} _{-27.9}	
J16113134-1838259	116.35 ^{+3.44} _{-3.44}	-0.77 ^{+0.01} _{-0.01}	-1.10 ^{+0.01} _{-0.01}	0.38 ^{+0.02} _{-0.02}	64.2 ^{+3.1} _{-3.2}	108.6 ^{+3.0} _{-2.8}	
J16120505-2043404	3.47 ^{+0.13} _{-0.13}	-0.32 ^{+0.01} _{-0.01}	0.22 ^{+0.01} _{-0.01}	0.13 ^{+0.02} _{-0.02}	38.2 ^{+13.9} _{-19.2}	53.3 ^{+48.4} _{-49.9}	
J16123414-2144500	4.52 ^{+0.36} _{-0.36}	-7.24 ^{+0.02} _{-0.02}	-5.61 ^{+0.02} _{-0.02}	0.51 ^{+0.06} _{-0.07}	84.3 ^{+5.0} _{-9.0}	53.7 ^{+5.2} _{-6.7}	
J16135434-2320342	6.41 ^{+0.19} _{-0.19}	0.59 ^{+0.01} _{-0.01}	-0.19 ^{+0.01} _{-0.01}	0.07 ^{+0.03} _{-0.04}	71.4 ^{+15.9} _{-28.7}	156.6 ^{+58.2} _{-44.1}	Barenfeld et al. (2019)
J16145131-2308515	3.52 ^{+0.29} _{-0.29}	2.17 ^{+0.02} _{-0.02}	6.24 ^{+0.03} _{-0.02}	0.60 ^{+0.08} _{-0.06}	70.1 ^{+8.7} _{-8.3}	168.7 ^{+6.1} _{-5.2}	

Table 4 continued on next page

Table 4 (continued)

Field	Flux (mJy)	$\Delta\alpha$ (arcsec)	$\Delta\delta$ (arcsec)	Major axis (arcsec)	Inclination (deg)	PA (deg)	Notes
J16150753-2420204	1.35 ^{+0.26} _{-0.26}	2.97 ^{+0.06} _{-0.05}	6.18 ^{+0.05} _{-0.05}	0.46 ^{+0.16} _{-0.13}	49.3 ^{+19.2} _{-21.0}	122.8 ^{+80.5} _{-15.0}	
J16153220-2010236	1.92 ^{+0.13} _{-0.13}	0.22 ^{+0.01} _{-0.01}	0.20 ^{+0.01} _{-0.01}	0.14 ^{+0.05} _{-0.07}	83.8 ^{+5.2} _{-33.4}	150.0 ^{+35.8} _{-39.4}	WDS 16155-2010
J16162531-2412057	2.61 ^{+0.21} _{-0.21}	3.98 ^{+0.02} _{-0.02}	2.61 ^{+0.01} _{-0.01}	0.37 ^{+0.05} _{-0.05}	52.7 ^{+12.6} _{-18.2}	78.3 ^{+21.2} _{-18.8}	
J16164689-2033323	1.63 ^{+0.33} _{-0.33}	1.18 ^{+0.08} _{-0.07}	-1.18 ^{+0.07} _{-0.07}	0.89 ^{+0.23} _{-0.20}	42.0 ^{+19.0} _{-15.7}	140.1 ^{+47.4} _{-36.8}	
J16171889-2230017	3.67 ^{+0.24} _{-0.24}	-3.19 ^{+0.02} _{-0.02}	2.28 ^{+0.01} _{-0.02}	0.41 ^{+0.05} _{-0.05}	41.1 ^{+10.7} _{-16.6}	7.5 ^{+30.4} _{-26.9}	
J16182735-2009533	1.41 ^{+0.18} _{-0.18}	3.80 ^{+0.03} _{-0.03}	-0.93 ^{+0.02} _{-0.03}	0.33 ^{+0.08} _{-0.07}	47.5 ^{+16.7} _{-23.4}	175.7 ^{+19.9} _{-86.3}	
J16185277-2259537	1.58 ^{+0.13} _{-0.13}	-0.67 ^{+0.01} _{-0.01}	-0.21 ^{+0.01} _{-0.01}	0.17 ^{+0.05} _{-0.06}	66.8 ^{+20.8} _{-22.2}	29.6 ^{+43.6} _{-33.7}	
J16185382-2053182	6.16 ^{+0.13} _{-0.13}	-0.38 ^{+0.01} _{-0.01}	0.18 ^{+0.01} _{-0.01}	0.08 ^{+0.02} _{-0.03}	44.8 ^{+31.2} _{-16.3}	75.8 ^{+45.4} _{-66.2}	
J16200357-2419396	1.35 ^{+0.11} _{-0.11}	3.04 ^{+0.01} _{-0.01}	2.36 ^{+0.01} _{-0.01}	0.12 ^{+0.05} _{-0.04}	61.4 ^{+20.5} _{-23.0}	86.9 ^{+36.5} _{-53.1}	
J16215741-2238180	2.92 ^{+0.11} _{-0.11}	-0.27 ^{+0.01} _{-0.01}	0.34 ^{+0.01} _{-0.01}	0.03 ^{+0.04} _{-0.03}	83.6 ^{+5.5} _{-35.6}	35.3 ^{+40.2} _{-67.4}	
J16365288-2708187	1.59 ^{+0.24} _{-0.24}	1.39 ^{+0.04} _{-0.04}	4.71 ^{+0.04} _{-0.04}	0.54 ^{+0.12} _{-0.10}	42.1 ^{+15.8} _{-18.4}	37.0 ^{+64.5} _{-28.6}	

Table 5. CO J=3–2 flux measurements for the full sample

2MASS	Flux (mJy km s ⁻¹)	V _{LSRK} ^a	radius ^b
		(km s ⁻¹)	(arcsec)
J15354856-2958551	54.7 ± 28.6	0.1 - 9.8	0.25
J15442550-2126408	61.6 ± 7.8 ^c	5.0 - 7.1	0.25 ^d
J15462696-2443225	63.3 ± 53.6	0.1 - 9.9	0.25
J15465432-2556520	172.9 ± 51.3	0.1 - 9.8	0.25
J15472572-2609185	58.7 ± 49.2	0.0 - 10.1	0.25
J15480853-2507011	294.7 ± 48.3	-0.1 - 10.0	0.25
J15482445-2235495	113.1 ± 18.2	-3.0 - 10.2	0.25
J15485435-2443101	292.4 ± 45.0	0.0 - 10.1	0.25
J15510126-2523100	8.1 ± 48.3	0.0 - 10.1	0.25
J15514032-2146103	97.5 ± 31.8	-0.2 - 10.0	0.25
J15514709-2113234	43.5 ± 17.3	-0.2 - 10.0	0.25
J15520884-2723456	29.5 ± 44.5	0.0 - 10.1	0.25
J15521088-2125372	366.1 ± 24.6	0.0 - 8.4	0.25
J15524851-2845369	29.8 ± 46.3	-0.1 - 10.0	0.25
J15530132-2114135	185.2 ± 21.4	1.0 - 6.9	0.25
J15534211-2049282	448.2 ± 28.4	-0.3 - 11.1	0.25
J15540240-2254587	142.2 ± 19.5	-0.6 - 7.5	0.30
J15551704-2322165	4.1 ± 31.1	0.1 - 9.8	0.25
J15554314-2437435	52.7 ± 46.2	-0.1 - 10.0	0.25
J15554883-2512240	-39.0 ± 28.9	-0.2 - 10.0	0.25
J15562477-2225552	114.9 ± 18.9	2.0 - 5.0	0.40
J15564244-2039339	2.3 ± 16.3	0.1 - 9.8	0.25
J15565600-2911349	-68.6 ± 44.2	-0.2 - 10.0	0.25
J15570146-2046184	73.1 ± 17.0	0.0 - 10.1	0.25
J15570641-2206060	11.1 ± 14.5	0.0 - 10.1	0.25
J15571045-2545307	117.5 ± 43.8	0.2 - 9.9	0.25
J15572109-2202130	74.4 ± 17.7	-0.1 - 10.1	0.25
J15572986-2258438	8.6 ± 14.6	-0.2 - 10.0	0.25
J15573049-1903014	31.0 ± 18.0	0.1 - 9.9	0.25
J15575444-2450424	731.5 ± 128.8	-10.5 - 13.6	0.35 ^d
J15581270-2328364	31.8 ± 30.3	0.0 - 10.2	0.25
J15582981-2310077	35.8 ± 15.4	-0.2 - 10.0	0.25
J15583620-1946135	646.0 ± 25.2	5.3 - 9.1	0.40
J15583692-2257153	5359.3 ± 130.2	1.4 - 14.1	0.85
J15584772-1757595	-40.7 ± 27.4	0.0 - 10.2	0.25
J15590484-2422469	997.8 ± 79.5	-1.6 - 9.9	0.35 ^d
J15591452-2606182	17.7 ± 50.5	-0.1 - 10.1	0.25
J15594231-2945495	168.0 ± 51.3	-0.2 - 10.0	0.25

Table 5 continued on next page

Table 5 (*continued*)

2MASS	Flux	V _{LSRK} ^a	radius ^b
	(mJy km s ⁻¹)	(km s ⁻¹)	(arcsec)
J15594426-2029232	17.2 ± 17.5	-0.1 - 10.0	0.25
J15594460-2155250	-4.8 ± 15.2	0.2 - 9.9	0.25
J15595116-2311044	173.5 ± 22.8	-2.8 - 9.5	0.30 ^d
J15595759-1812234	110.9 ± 21.2	-3.1 - 12.1	0.25
J16001330-2418106	-6.0 ± 27.3	0.1 - 9.9	0.25
J16001730-2236504	-27.6 ± 30.9	0.0 - 10.1	0.25
J16001844-2230114	2213.4 ± 80.0	3.8 - 20.3	0.50 ^d
J16002945-2022536	26.1 ± 16.7	-0.2 - 10.0	0.25
J16011398-2516281	6.8 ± 53.9	0.1 - 9.8	0.25
J16012268-2408003	3540.4 ± 233.7	-8.4 - 11.9	0.65
J16012652-2301343	20.2 ± 16.8	0.1 - 9.8	0.25
J16012902-2509069	56.9 ± 45.7	0.1 - 9.8	0.25
J16014086-2258103	454.5 ± 29.3	-2.0 - 7.7	0.25
J16014157-2111380	51.3 ± 26.6	-0.1 - 10.1	0.25
J16020039-2221237	-13.6 ± 27.5	-0.2 - 10.0	0.25
J16020287-2236139	9.7 ± 31.4	-0.2 - 10.0	0.25
J16020429-2231468	83.6 ± 16.4	-3.6 - 2.3	0.25
J16020517-2331070	61.6 ± 17.5	-0.2 - 10.0	0.25
J16020757-2257467	746.0 ± 52.1	-0.7 - 8.6	0.40 ^d
J16023587-2320170	-16.6 ± 17.4	-0.1 - 10.0	0.25
J16024152-2138245	51.1 ± 29.7	-0.1 - 10.1	0.25
J16025123-2401574	-5.6 ± 23.8	0.1 - 9.8	0.25
J16025431-1805300	78.1 ± 16.6	0.0 - 10.2	0.25
J16025855-2256495	7.6 ± 14.3	0.0 - 10.1	0.25
J16030161-2207523	47.2 ± 26.2	-0.1 - 10.1	0.25
J16031329-2112569	-14.6 ± 23.4	0.1 - 9.8	0.25
J16032225-2413111	15.0 ± 28.0	0.1 - 9.9	0.25
J16032277-2238206	28.1 ± 15.2	0.1 - 9.8	0.25
J16032625-2155378	36.0 ± 16.6	-0.1 - 10.0	0.25
J16035228-2321076	125.2 ± 12.6	-0.2 - 5.7	0.25 ^d
J16035767-2031055	388.1 ± 63.3	0.3 - 9.2	0.35 ^d
J16035793-1942108	1446.4 ± 58.2	1.8 - 14.1	0.40
J16041416-2129151	167.3 ± 16.8	3.4 - 8.0	0.30 ^d
J16041740-1942287	54.0 ± 27.0	0.1 - 9.9	0.25
J16041792-1941505	4.1 ± 18.7	0.2 - 9.9	0.25
J16041893-2430392	107.6 ± 51.1	0.1 - 9.8	0.25
J16042165-2130284	20380.1 ± 128.0	3.0 - 6.4	2.10 ^d
J16043916-1942459	-7.5 ± 23.7	0.2 - 9.9	0.25
J16044876-1748393	5.4 ± 15.5	0.0 - 10.1	0.25
J16050231-1941554	-26.4 ± 25.8	-0.2 - 10.0	0.25

Table 5 *continued on next page*

Table 5 (*continued*)

2MASS	Flux	V _{LSRK} ^a	radius ^b
	(mJy km s ⁻¹)	(km s ⁻¹)	(arcsec)
J16050647-1734020	-1.0 ± 13.7	0.0 - 10.2	0.25
J16050844-1947070	-21.1 ± 19.6	0.1 - 9.8	0.25
J16052076-1821367	63.9 ± 16.6	0.1 - 9.9	0.25
J16052157-1821412	8067.9 ± 102.2	-4.1 - 17.1	0.85
J16052459-1954419	-16.5 ± 25.0	-0.2 - 10.0	0.25
J16052556-2035397	-20.2 ± 15.3	-0.2 - 10.0	0.25
J16052661-1957050	28.6 ± 26.5	-0.2 - 10.0	0.25
J16052730-2614090	45.8 ± 46.5	-0.2 - 10.0	0.25
J16052787-2115510	-2.9 ± 17.6	0.0 - 10.1	0.25
J16052875-2655496	1.4 ± 48.0	0.0 - 10.1	0.25
J16053215-1933159	21.7 ± 15.7	0.1 - 9.8	0.25
J16054540-2023088	235.3 ± 29.2	-1.9 - 7.0	0.25
J16055863-1949029	29.5 ± 31.6	-0.1 - 10.1	0.25
J16060061-1957114	12.3 ± 15.8	0.1 - 9.9	0.25
J16060215-2003142	335.7 ± 25.7	2.0 - 11.3	0.40
J16061144-1935405	20.0 ± 18.6	0.1 - 9.8	0.25
J16061330-2212537	-2.5 ± 25.8	-0.1 - 10.1	0.25
J16062196-1928445	20.8 ± 65.0	0.0 - 10.2	0.25
J16062277-2011243	100.5 ± 11.3	3.5 - 10.7	0.25
J16062383-1807183	741.9 ± 38.6	3.1 - 7.8	0.55 ^d
J16062861-2121297	1831.1 ± 68.9	-1.9 - 9.1	0.60 ^d
J16063539-2516510	54.2 ± 33.0	-0.1 - 10.1	0.25
J16064102-2455489	44.1 ± 24.2	0.0 - 10.2	0.25
J16064115-2517044	54.6 ± 28.6	-0.1 - 10.1	0.25
J16064385-1908056	21.5 ± 27.7	0.1 - 9.9	0.25
J16064794-1841437	8837.4 ± 144.6	-0.9 - 14.7	1.10
J16070014-2033092	27.7 ± 29.2	-0.1 - 10.1	0.25
J16070211-2019387	-22.0 ± 12.3	-0.1 - 10.1	0.25
J16070304-2331460	112.5 ± 13.4	-4.0 - 5.8	0.25 ^d
J16070873-1927341	27.2 ± 30.3	0.1 - 9.9	0.25
J16071403-1702425	-5.8 ± 16.7	0.0 - 10.2	0.25
J16071971-2020555	-0.7 ± 30.4	0.0 - 10.2	0.25
J16072625-2432079	259.7 ± 43.4	-2.8 - 12.9	0.25
J16072682-1855239	17.3 ± 16.4	0.2 - 9.9	0.25
J16072747-2059442	64.2 ± 24.5	-0.1 - 10.0	0.25
J16072863-2630130	34.8 ± 44.9	0.0 - 10.1	0.25
J16072955-2308221	258.3 ± 21.7	-0.4 - 9.3	0.35 ^d
J16073939-1917472	8.7 ± 29.8	-0.2 - 10.0	0.25
J16075796-2040087	3765.2 ± 107.8	-16.5 - 16.5	0.45 ^d
J16080555-2218070	6.0 ± 23.0	0.2 - 9.9	0.25

Table 5 *continued on next page*

Table 5 (*continued*)

2MASS	Flux (mJy km s ⁻¹)	V _{LSRK} ^a (km s ⁻¹)	radius ^b (arcsec)
J16081566-2222199	274.1 ± 30.4	-3.2 - 6.5	0.30 ^d
J16082324-1930009	1359.7 ± 208.4	-1.8 - 8.8	0.65
J16082733-2217292	117.9 ± 13.8	2.0 - 6.2	0.35 ^d
J16082751-1949047	19.0 ± 14.7	-0.1 - 10.0	0.25
J16082870-2137198	193.6 ± 20.5	0.8 - 5.9	0.35
J16083319-2015549	421.1 ± 28.5	-2.1 - 10.2	0.35 ^d
J16083455-2211559	4.4 ± 27.3	-0.2 - 10.0	0.25
J16084836-2341209	41.4 ± 11.7	0.0 - 10.2	0.25
J16084894-2400045	18.0 ± 29.4	0.0 - 10.2	0.25
J16090002-1908368	8.4 ± 13.5	0.1 - 9.8	0.25
J16090071-2029086	52.3 ± 18.7	-0.1 - 10.1	0.25
J16090075-1908526	1107.4 ± 153.1	-0.1 - 8.0	0.50 ^d
J16090451-2224523	-7.2 ± 14.7	-0.1 - 10.1	0.25
J16092136-2139342	-0.4 ± 16.0	-0.1 - 10.1	0.25
J16093164-2229224	34.8 ± 15.4	0.0 - 10.1	0.25
J16093558-1828232	33.5 ± 27.1	-0.2 - 10.0	0.25
J16093653-1848009	838.4 ± 52.8	-2.5 - 6.0	0.55
J16093730-2027250	28.8 ± 16.2	-0.1 - 10.0	0.25
J16094098-2217594	10.9 ± 28.9	0.0 - 10.1	0.25
J16095361-1754474	58.7 ± 28.2	-0.1 - 10.1	0.25
J16095441-1906551	-3.0 ± 33.0	0.2 - 9.9	0.25
J16095933-1800090	477.0 ± 40.3	1.1 - 7.1	0.50
J16101100-1946040	11.2 ± 15.6	0.1 - 9.8	0.25
J16101264-2104446	8456.0 ± 112.6	0.9 - 12.3	1.00
J16101473-1919095	-2.4 ± 30.8	0.2 - 9.9	0.25
J16101888-2502325	67.7 ± 25.0	0.0 - 10.2	0.25
J16101903-2124251	22.2 ± 15.5	-0.1 - 10.1	0.25
J16102174-1904067	-44.0 ± 28.9	-0.2 - 10.0	0.25
J16102819-1910444	29.5 ± 29.3	-0.2 - 10.0	0.25
J16102857-1904469	2.0 ± 29.9	-0.2 - 10.0	0.25
J16103956-1916524	-19.0 ± 32.2	-0.2 - 10.0	0.25
J16104202-2101319	18.9 ± 26.8	-0.1 - 10.1	0.25
J16104391-2032025	7.0 ± 15.8	0.2 - 9.9	0.25
J16104636-1840598	180.5 ± 30.0	-0.1 - 10.1	0.25
J16105011-2157481	56.2 ± 12.9	-0.2 - 10.0	0.25
J16105240-1937344	4.0 ± 16.5	0.1 - 9.8	0.25
J16105691-2204515	154.0 ± 15.4	1.9 - 5.3	0.40 ^d
J16111095-1933320	82.3 ± 45.4	0.1 - 2.2	0.85
J16111237-1927374	72.4 ± 8.7	2.6 - 5.6	0.25 ^d
J16111330-2019029	181.8 ± 21.6	3.5 - 9.5	0.25

Table 5 *continued on next page*

Table 5 (*continued*)

2MASS	Flux	V _{LSRK} ^a	radius ^b
	(mJy km s ⁻¹)	(km s ⁻¹)	(arcsec)
J16111534-1757214	76.4 ± 33.8	0.1 - 9.9	0.25
J16111705-2213085	134.1 ± 11.4	1.5 - 9.5	0.30 ^d
J16111742-1918285	660.7 ± 58.1	-2.0 - 10.3	0.55
J16111907-2319202	-1.4 ± 14.3	0.0 - 10.2	0.25
J16112057-1820549	15.8 ± 28.3	0.1 - 9.8	0.25
J16112601-2631558	45.4 ± 45.7	0.1 - 9.8	0.25
J16113134-1838259	29813.3 ± 126.2 ^c	-0.8 - 9.8	0.90 ^d
J16114534-1928132	53.3 ± 18.3	0.1 - 9.8	0.25
J16114612-1907429	35.2 ± 14.8	0.0 - 10.2	0.25
J16115091-2012098	395.1 ± 32.1	-0.6 - 6.2	0.30
J16120239-1926218	40.1 ± 17.0	0.0 - 10.2	0.25
J16120505-2043404	20.9 ± 16.6	0.0 - 10.2	0.25
J16120668-3010270	10016.5 ± 350.5	0.8 - 9.3	1.35
J16121242-1907191	311.5 ± 12.0	2.2 - 4.7	0.40
J16122737-2009596	53.8 ± 30.4	-0.1 - 10.1	0.25
J16123352-2543281	76.0 ± 53.6	-0.1 - 10.0	0.25
J16123414-2144500	-62.4 ± 75.9	0.1 - 9.8	0.90 ^d
J16123916-1859284	2143.9 ± 114.2	-0.3 - 9.5	0.70 ^d
J16124893-1800525	36.6 ± 34.0	-0.1 - 10.1	0.25
J16125533-2319456	29.7 ± 28.2	-0.2 - 10.0	0.25
J16130627-2606107	79.0 ± 42.1	0.1 - 9.8	0.25
J16130982-2302184	-4.6 ± 14.6	-0.1 - 10.1	0.25
J16130996-1904269	27.3 ± 25.2	0.2 - 9.9	0.25
J16132190-2136136	560.7 ± 28.7	0.6 - 10.8	0.45 ^d
J16133650-2503473	62.1 ± 37.8	0.1 - 9.8	0.25
J16134880-2509006	27.6 ± 12.8	-0.1 - 10.1	0.25
J16135434-2320342	115.0 ± 27.9	0.0 - 10.1	0.25
J16140792-1938292	3263.6 ± 63.0	-1.5 - 16.3	0.70 ^d
J16141107-2305362	5.8 ± 13.3	0.0 - 10.2	0.25
J16142029-1906481	4771.9 ± 92.3	-9.2 - 13.3	0.80 ^d
J16142091-1906051	8836.0 ± 121.1	-11.1 - 13.5	1.20 ^d
J16142893-1857224	-1.4 ± 27.3	0.0 - 10.1	0.25
J16143367-1900133	557.3 ± 29.7	-3.0 - 8.0	0.25
J16145024-2100599	2262.4 ± 63.1	-2.5 - 9.8	0.75 ^d
J16145026-2332397	943.1 ± 43.6	0.8 - 12.3	0.50 ^d
J16145131-2308515	-3.2 ± 12.2	0.1 - 9.8	0.25
J16145244-2513523	12.1 ± 13.0	0.0 - 10.2	0.25
J16145918-2750230	-58.7 ± 31.3	0.2 - 9.9	0.25
J16145928-2459308	111.7 ± 28.0	-0.2 - 10.0	0.25
J16150095-2733553	101.3 ± 44.2	-0.1 - 10.0	0.25

Table 5 *continued on next page*

Table 5 (*continued*)

2MASS	Flux (mJy km s ⁻¹)	V _{LSRK} ^a	radius ^b
		(km s ⁻¹)	(arcsec)
J16150753-2420204	-6.3 ± 13.1	-0.1 - 10.0	0.25
J16151239-2420091	-31.4 ± 25.3	0.0 - 10.1	0.25
J16152752-1847097	8219.5 ± 144.0	-6.2 - 14.1	1.15
J16153220-2010236	6.2 ± 12.9	-0.1 - 10.1	0.25
J16153341-1854249	4.7 ± 12.0	0.1 - 9.8	0.25
J16153456-2242421	342.4 ± 34.7	-8.2 - 12.2	0.25 ^d
J16154416-1921171	11301.9 ± 114.7	-3.3 - 10.3	0.70 ^d
J16154533-2110294	17.4 ± 12.8	0.2 - 9.9	0.25
J16154914-2213117	-1.4 ± 13.2	0.0 - 10.1	0.25
J16160448-2932400	623.2 ± 73.6	2.5 - 8.0	0.45 ^d
J16160602-2528217	-10.3 ± 15.7	0.1 - 9.9	0.25
J16161423-2643148	-74.0 ± 47.5	0.1 - 9.8	0.25
J16162531-2412057	-5.5 ± 12.8	0.1 - 9.8	0.25
J16163345-2521505	221.5 ± 26.5	0.4 - 10.6	0.25
J16164689-2033323	17.3 ± 13.1	0.0 - 10.1	0.25
J16165083-2009081	380.0 ± 19.9	0.1 - 5.1	0.40 ^d
J16165556-2014219	12.4 ± 13.3	0.1 - 9.8	0.25
J16171889-2230017	52.4 ± 11.2	0.1 - 9.8	0.25
J16172756-2517222	81.9 ± 13.1	0.3 - 10.9	0.25
J16175432-2543435	-11.9 ± 14.3	-0.1 - 10.0	0.25
J16180868-2547126	-5.6 ± 13.8	-0.1 - 10.0	0.25
J16181445-2319251	269.5 ± 16.4	-0.8 - 8.9	0.30
J16181618-2619080	20.2 ± 26.5	0.0 - 10.2	0.25
J16181811-2221150	1.8 ± 10.4	-0.2 - 10.0	0.25
J16181904-2028479	335.1 ± 36.4	-0.6 - 8.7	0.35
J16182735-2009533	46.5 ± 10.0	3.7 - 10.4	0.25 ^d
J16183317-2517504	31.6 ± 14.6	0.0 - 10.2	0.25
J16185228-2516149	-3.5 ± 14.4	0.1 - 9.8	0.25
J16185277-2259537	0.5 ± 12.6	0.2 - 9.9	0.25
J16185382-2053182	176.5 ± 19.0 ^c	-1.9 - 16.7	0.25
J16191008-2432088	57.3 ± 15.0	-0.1 - 10.0	0.25
J16191936-2329192	13.6 ± 13.3	0.2 - 9.9	0.25
J16192288-2135037	3.4 ± 12.3	0.1 - 9.9	0.25
J16193570-1950426	8863.0 ± 87.2	-5.5 - 16.1	0.70 ^d
J16194711-2203112	17.0 ± 12.1	0.1 - 9.8	0.25
J16194836-2212519	-0.7 ± 15.1	0.1 - 10.2	0.25
J16200357-2419396	0.2 ± 13.7	0.0 - 10.2	0.25
J16200616-2212385	2.0 ± 12.7	0.1 - 9.8	0.25
J16201053-2139090	84.9 ± 26.1	0.2 - 9.9	0.40 ^d
J16201949-2337412	0.2 ± 14.5	-0.2 - 10.0	0.25

Table 5 *continued on next page*

Table 5 (*continued*)

2MASS	Flux	V_{LSRK}^a	radius ^b
	(mJy km s ⁻¹)	(km s ⁻¹)	(arcsec)
J16202291-2227041	343.1 ± 33.1	-1.6 - 7.7	0.45
J16202863-2442087	3604.2 ± 95.7	-0.9 - 11.8	1.00
J16203960-2634284	6991.7 ± 121.1	-3.4 - 10.2	1.20
J16204233-2431473	4.4 ± 13.1	0.1 - 9.8	0.25
J16204468-2431384	-15.1 ± 15.6	0.1 - 9.8	0.25
J16212930-2537567	-26.0 ± 14.2	-0.1 - 10.1	0.25
J16213469-2612269	2494.9 ± 68.3	-2.8 - 13.3	0.65
J16215466-2043091	9.3 ± 27.3	-0.1 - 10.0	0.25
J16215472-2752053	3324.4 ± 80.2	-5.2 - 16.8	0.65
J16215741-2238180	37.8 ± 14.0	-0.2 - 10.0	0.25
J16220194-2245410	22.7 ± 12.2	-0.2 - 10.0	0.25
J16220961-1953005	-25.8 ± 31.2	0.1 - 9.8	0.25
J16221000-2409118	5.1 ± 12.7	-0.1 - 10.1	0.25
J16221481-2045398	4.2 ± 15.1	-0.2 - 10.0	0.25
J16221532-2511349	1970.7 ± 55.7	-3.7 - 10.3	0.60
J16222160-2217307	68.4 ± 12.2	-0.1 - 10.1	0.25
J16222982-2002472	4519.5 ± 65.5	-6.4 - 8.8	0.70
J16230761-2516339	923.5 ± 31.6	-1.1 - 9.1	0.45
J16230783-2300596	57.2 ± 29.9	0.0 - 10.2	0.25
J16231145-2517357	269.2 ± 26.2	0.6 - 11.2	0.40
J16235385-2946401	5.6 ± 27.8	0.2 - 9.9	0.25
J16235468-2515392	40.4 ± 14.1	-0.1 - 10.0	0.25
J16251521-2511540	27.3 ± 14.4	0.0 - 10.2	0.25
J16252883-2607538	-19.5 ± 13.1	-0.2 - 10.0	0.25
J16253798-1943162	3943.3 ± 100.7	0.0 - 14.8	0.95
J16253849-2613540	312.7 ± 32.3	2.4 - 17.2	0.45 ^d
J16254322-2230026	-3.8 ± 14.8	-0.1 - 10.0	0.25
J16261080-2525125	14.7 ± 13.6	0.1 - 9.8	0.25
J16262925-2507041	28.2 ± 13.1	0.2 - 9.9	0.25
J16263926-2113453	36.7 ± 13.1	-0.2 - 10.0	0.25
J16270942-2148457	98.4 ± 25.1	0.0 - 10.2	0.25
J16271273-2504017	637.0 ± 39.6	-3.9 - 10.9	0.45 ^d
J16274905-2602437	2442.1 ± 54.1	-6.2 - 7.7	0.60
J16284517-2604324	36.5 ± 14.0	-0.2 - 10.0	0.25
J16290902-2515028	32.4 ± 15.1	0.0 - 10.2	0.25
J16293267-2543291	1500.9 ± 56.5	-3.0 - 11.4	0.55
J16294879-2137086	4.0 ± 12.7	0.1 - 9.9	0.25
J16294991-2728498	14.7 ± 15.3	0.0 - 10.2	0.25
J16303390-2428062	5.3 ± 24.5	0.0 - 10.1	0.25
J16364650-2502032	16.0 ± 14.6	0.1 - 9.9	0.25

Table 5 *continued on next page*

Table 5 (*continued*)

2MASS	Flux	V_{LSRK}^a	radius ^b
	(mJy km s ⁻¹)	(km s ⁻¹)	(arcsec)
J16365288-2708187	9.8 ± 16.9	0.0 - 10.2	0.25
J16370169-2545368	12.0 ± 14.3	0.0 - 10.1	0.25
J16371121-2725003	184.6 ± 21.4	3.8 - 11.4	0.35
J16394272-2812141	87.5 ± 11.9	0.9 - 7.2	0.25
J16395577-2347355	901.8 ± 32.2	-4.3 - 9.2	0.40
J16413713-2730489	23.3 ± 14.6	0.0 - 10.2	0.25

^aVelocity range used to compute the flux.^bAperture radius to compute the flux.^cFlux measurement is contaminated by nearby source.^dRadius set by visual inspection.

Table 6. CO J=3–2 flux measurements for additional sources

Field	Flux (mJy km s ⁻¹)	V _{LSRK} ^a (km s ⁻¹)	radius ^b (arcsec)
J15442550-2126408	152.3 ± 18.5	-3.9 - 7.1	0.25
J15480853-2507011	588.7 ± 50.8	-0.1 - 7.5	0.30 ^d
J15510126-2523100	138.6 ± 43.1	0.0 - 10.1	0.25
J15524851-2845369	32.7 ± 49.5	-0.1 - 10.0	0.25
J15564244-2039339	288.8 ± 26.7	-2.1 - 8.1	0.35 ^d
J15584772-1757595	19.1 ± 32.2	0.0 - 10.2	0.25
J15594231-2945495	83.5 ± 50.8	-0.2 - 10.0	0.25
J15594460-2155250	20.3 ± 16.8	0.2 - 9.9	0.25
J16012902-2509069	16.9 ± 42.3	0.1 - 9.8	0.25
J16020287-2236139	4.5 ± 36.3	-0.2 - 10.0	0.25
J16025123-2401574	18.9 ± 32.5	0.1 - 9.8	0.25
J16032225-2413111	3.6 ± 44.4	0.1 - 9.9	0.25
J16044876-1748393	29.9 ± 16.5	0.0 - 10.1	0.25
J16050647-1734020	132.3 ± 17.4	0.0 - 14.8	0.25
J16052556-2035397	6.6 ± 14.0	-0.2 - 10.0	0.25
J16052730-2614090	71.1 ± 58.8	-0.2 - 10.0	0.25
J16060215-2003142	-33.1 ± 26.1	-0.1 - 10.1	0.25
J16064385-1908056	22.9 ± 29.0	0.1 - 9.9	0.25
J16092136-2139342	122.9 ± 16.6	-0.5 - 5.8	0.30 ^d
J16104391-2032025	-33.0 ± 25.2	0.2 - 9.9	0.25
J16111095-1933320	5.5 ± 22.1	0.1 - 9.8	0.25
J16111742-1918285	-26.7 ± 15.7	0.2 - 9.9	0.25
J16112601-2631558	-89.6 ± 65.2	0.1 - 9.8	0.25
J16113134-1838259	9025.7 ± 78.3 ^c	-10.5 - 11.9	0.40 ^d
J16120505-2043404	31.5 ± 15.0	0.0 - 10.2	0.25
J16123414-2144500	-57.7 ± 36.2	0.1 - 9.8	0.25
J16125533-2319456	-2.6 ± 68.8	-0.2 - 10.0	0.25
J16135434-2320342	109.3 ± 22.1	-1.7 - 5.5	0.25
J16145131-2308515	-13.6 ± 17.1	0.1 - 9.8	0.25
J16150753-2420204	-7.2 ± 19.8	-0.1 - 10.0	0.25
J16153220-2010236	30.3 ± 13.4	-0.1 - 10.1	0.25
J16162531-2412057	21.5 ± 17.2	0.1 - 9.8	0.25
J16164689-2033323	5.7 ± 13.1	0.0 - 10.1	0.25
J16171889-2230017	-12.8 ± 15.8	0.1 - 9.8	0.25
J16182735-2009533	11.2 ± 15.4	-0.2 - 10.0	0.25
J16185277-2259537	24.9 ± 13.1	0.2 - 9.9	0.25
J16185382-2053182	1379.6 ± 61.3	-3.6 - 19.2	0.55
J16200357-2419396	9.0 ± 16.5	0.0 - 10.2	0.25

Table 6 continued on next page

Table 6 (*continued*)

Field	Flux	V_{LSRK}^a	radius ^b
	(mJy km s ⁻¹)	(km s ⁻¹)	(arcsec)
J16215741-2238180	42.9 ± 12.7	-0.2 - 10.0	0.25
J16365288-2708187	-2.1 ± 19.7	0.0 - 10.2	0.25

^aVelocity range used to compute the flux.^bAperture radius to compute the flux.^cFlux measurement is contaminated by nearby source.^dRadius set by visual inspection.